

Double White Dwarfs as Probes of Single and Binary Star Evolution

Jeffrey John Andrews

Submitted in partial fulfillment of the
requirements for the degree
of Doctor of Philosophy
in the Graduate School of Arts and Sciences

COLUMBIA UNIVERSITY

2016

ProQuest Number: 10017971

All rights reserved

INFORMATION TO ALL USERS

The quality of this reproduction is dependent upon the quality of the copy submitted.

In the unlikely event that the author did not send a complete manuscript and there are missing pages, these will be noted. Also, if material had to be removed, a note will indicate the deletion.



ProQuest 10017971

Published by ProQuest LLC (2016). Copyright of the Dissertation is held by the Author.

All rights reserved.

This work is protected against unauthorized copying under Title 17, United States Code
Microform Edition © ProQuest LLC.

ProQuest LLC.
789 East Eisenhower Parkway
P.O. Box 1346
Ann Arbor, MI 48106 - 1346

©2016

Jeffrey John Andrews
All rights reserved

ABSTRACT

Double White Dwarfs as Probes of Single and Binary Star Evolution

Jeffrey John Andrews

As the endpoints of stars less massive than $\sim 8 M_{\odot}$, the population of Galactic white dwarfs (WD) contain information about complex stellar evolution processes. Associated pairs of WDs add an extra degree of leverage; both WDs must have formed and evolved together. The work presented in this dissertation uses various populations of double WDs (DWD) to constrain evolution of both single and binary stars.

One example is the set of low-mass WDs with unseen WD companions, which are formed through a dynamically-unstable mass loss process called the common envelope. To work toward a quantitative understanding of the common envelope, we develop and apply a Bayesian statistical technique to identify the masses of the unseen WD companions. We provide results which can be compared to evolutionary models and hence a deeper understanding of how binary stars evolve through a common envelope. The statistical technique we develop can be applied to any population of single-line spectroscopic binaries.

Binaries widely separated enough that they avoid any significant interaction independently evolve into separate WDs that can be identified in photometric and astrometric surveys. We discuss techniques for finding these objects, known as wide DWDs. We present a catalog of 142 candidate wide DWDs, combining both previously detected systems and systems we identify in our searches in the Sloan Digital Sky Survey. Having

been born at the same time, the masses and cooling ages of the WDs in wide DWDs, obtained with our spectroscopic follow-up campaign can be used to constrain the initial-final mass relation, which relates a main sequence star to the mass of the WD into which it will evolve. We develop a novel Bayesian technique to interpret our data and present our resulting constraints on this relation which are particularly strong for initial masses between 2 and 4 M_{\odot} .

During this process, we identified one wide DWD, HS 2220+2146, that was peculiar since the more massive WD in this system evolved second. We construct an evolutionary formation scenario in which the system began as a hierarchical triple in which the inner binary merged (possibly due to Kozai-Lidov oscillations) forming a post-blue straggler binary. The system then evolved into the DWD we observe today. We further discuss the potential for identifying more wide DWDs, including peculiar systems like HS 2220+2146, in future surveys such as *Gaia*.

Contents

List of Figures	v
List of Tables	xv
Acknowledgments	xvii
Dedication	xxi
1 Introduction	1
1.1 A Brief Observational History of White Dwarfs	2
1.2 Modern White Dwarf Observations	5
1.3 Short Period WD Binaries	6
1.4 Wide DWDs	8
1.5 Initial-Final Mass Relation	12
1.5.1 Method 1: WDs in Clusters	13
1.5.2 Method 2: AGB Star Population Models	16
1.5.3 Method 3: WD Population Models	18
1.5.4 Method 4: Wide (Non-Double) WD Binaries	19
1.5.5 Method 5: Wide Double White Dwarfs	21
1.6 Triple Systems	23
1.7 Dissertation Structure	26

2	ELM WDs	29
2.1	Introduction	29
2.2	Building our model	32
2.2.1	Our Model	34
2.3	Testing Our Model	37
2.3.1	Test 1: Single Gaussian (WD)	37
2.3.2	Test 2: Two Gaussians (WD + NS)	39
2.3.3	Test 3: Uniform (WD) + Gaussian (NS)	39
2.3.4	Test 4: PCEBs	40
2.4	Applying our model	40
2.4.1	The ELM Sample	40
2.4.2	Results and Discussion	42
2.5	Conclusions	44
2.6	Acknowledgments	45
3	Searching for Wide Double White Dwarf Binaries in SDSS DR7	47
3.1	Introduction	47
3.2	Motivation	48
3.2.1	Population Synthesis of DWD Systems	49
3.2.2	Evolution of the Synthesized DWD Orbits	52
3.2.3	Predicted Observed Angular Separation Distribution	52
3.3	Identifying Wide DWDs in SDSS	54
3.3.1	Candidate Binary Selection Process	54
3.3.2	Distances (and Radial Velocities)	56
3.3.3	Estimating the Purity of Our Sample	58
3.4	Results and Discussion	63
3.4.1	New DWDs	63
3.4.2	Comparison with Previously Known DWDs	67
3.5	Conclusions	72

3.6	Acknowledgments	73
4	Constraining the Initial-Final Mass Relation	75
4.1	Introduction	75
4.2	Searching for Wide DWDs	78
4.2.1	Common Proper Motion Pairs	78
4.2.2	Astrometrically Close Pairs	83
4.2.3	Comparison with Previous Samples	87
4.3	Assembling a Spectroscopic Sample	88
4.3.1	Observations and Reductions, and Spectra From the Literature	88
4.3.2	Atmospheric Model Fits to Our Spectra	102
4.3.3	Our Spectroscopic Sample	104
4.3.4	Comparison to the Baxter et al. (2014) Fit Results	108
4.3.5	Our DWD Sample for Constraining the IFMR	109
4.4	Constraining the IFMR with DWDs	110
4.4.1	Examining the Underlying Assumptions	110
4.4.2	Revisiting the Finley & Koester (1997) Result	117
4.4.3	A New Parametric Model for the IFMR	118
4.4.4	Testing the Model with Mock Data	127
4.4.5	Applying the Model to Wide DWDs	130
4.4.6	A Test of the Number of Model Parameters	133
4.5	Discussion	135
4.5.1	Comparison to Theoretical Predictions	135
4.5.2	Comparison to Other Observational Constraints	139
4.6	Conclusions	141
4.7	Appendix	145
4.8	Acknowledgments	151
5	The Curious Case of HS 2220+2146	153

5.1	Introduction	153
5.2	Observations	156
5.3	Proposed Formation Scenario	164
5.4	Discussion	166
5.4.1	The Eccentric Kozai-Lidov Mechanism	166
5.4.2	Wind Mass Accretion	167
5.5	Conclusions	173
5.6	Acknowledgments	174
6	Conclusions	177
6.1	Summary of Results and Future Work	179
7	Bibliography	183

List of Figures

1.1	A sample photometric plate from the data set of Haro & Luyten (1962). The photometric plate was exposed three separate times using, from left to right, B , V , and U filters, so each star appears as a triplet. The arrow points to the star PHL 384, a star with a B and U excess.	4
1.2	Constraints on the IFMR from Method 1 using WDs in clusters (red) and Method 4 using WDs in common proper motion pairs (blue). We also show constraints from the nearby WDs Sirius B and Procyon B (green). Finally, we show the IFMR constraint from the wide DWD PG 0922+162 (teal). . . .	13
2.1	The $M_1 - T$ distribution of the ELM sample (circles) and the known WD-NS binaries (triangles). The three eclipsing systems in the ELM sample with known M_2 are shown as filled circles, and the masses of the ELM WDs without detected RV variations are shown by the arrows. From M_1 and T alone, the two populations are indistinguishable.	31
2.2	Results from testing the first two mock data sets described in Section 2.3. The left-most panels show the companion masses (gray histogram) randomly drawn from each of our test distributions and our MAP models (black line). Panels in the second and third columns show samples from the posterior distributions of μ_{WD} and σ_{WD} and f_{NS} . Contours designate the 68% and 95% confidence levels. Dashed lines in these panels show the true values from which the sample systems were drawn. The fourth panel shows individual mock LMWD systems (ordered by increasing m_f) and their corresponding P_{NS} distribution. Tick marks along the bottom indicate inputted LMWD-NS systems.	38

2.3	The results of our model when applied to our third mock data set and the SDSS PCEB sample. The panels are same as those in Figure 2.2.	41
2.4	Results from applying our model to the ELM WDs. The panels are the same as in Figures 2.2 and 2.3. The left-most panel shows both the MAP M_2 distribution (solid black) and random samples from the posterior (gray lines). The three systems in the right-most panel with all $P_{\text{NS}} = 0\%$ are the eclipsing systems with measured M_2	42
3.1	Normalized orbital separation distribution of binaries produced by our population synthesis code once they become DWDs (solid line) and after perturbing effects have been taken into account (dashed line). The compact systems are depleted due to mergers, while the widest systems are disrupted due to three-body interactions.	51
3.2	Expected cumulative percentage of DWD as a function of separation once projection effects are taken into account. The binaries are artificially placed at a distance of 250 pc. Close pairs dominate the distribution, but $\sim 15\%$ have $\theta \gtrsim 2'$	53
3.3	$(g - r)$ vs. $(u - g)$ for 8605 spectroscopically confirmed DAs with a unique entry in the new Kleinman et al. catalog and with $ugriz$ photometric errors ≤ 0.15 mag (stars and dark contours). The points and light-colored contours to the upper right indicate the colors of $>99,000$ randomly selected stars with $ugriz$ errors ≤ 0.1 mag, $ugriz \geq 15.5$ mag, and $g \leq 20$ mag (these stars also meet the same proper motion constraints that were applied to our primary WDs). These stars are included to highlight the small overlap between the WD locus and the Main Sequence. Overplotted are different regions used to photometrically select WDs and A stars. The region defined by Girven et al. (2011) traces the empirical DA locus extremely well and includes 96% of the 8605 DAs, a significantly larger fraction than returned by the standard Richards et al. (2002) color-cuts.	54
3.4	θ distribution of real (solid line) and of false (dashed) candidate CPMBs. The primary WD positions were shifted by $\pm 1^\circ$ in both α and δ ; we then applied our method for identifying common proper motion companions to these shifted stars. There is an excess in the distribution of real candidates for $\theta \leq 1.5 - 2'$; at larger θ , the contamination by false pairs is essentially 100%.	59

3.5	<p>θ distribution of the 41 actual DWD candidates (solid line) compared to that of the artificially generated candidate CPMBs (dashed line). The dotted line is the predicted distribution from population synthesis (shown in Figure 3.2) normalized to the first bin in the real distribution, and suggests that our sample is incomplete at $\theta < 2'$. Our distribution of real candidates includes more candidates at large θ than is expected from our population synthesis results, and is strongly contaminated for $\theta > 2'$.</p>	60
3.6	<p>Percentage of model realizations that return a random star with the same properties as those of the 41 primary WDs in our candidate DWD binaries; θ is the separation of the corresponding candidate DWDs. The arrows indicate WDs for which P_m is either less than or greater than the y-axis limits. P_m can be $>100\%$ because a given realization may have more than one star with properties matching those of the candidate being tested. Note that there is a primary at $\theta \sim 5'$ with $P_m \sim 100\%$ and two primaries at $\theta \sim 8'$ that are also partially covered by the arrows. 13 primaries have $P_m < 1\%$ and $\theta < 2'$.</p>	61
3.7	<p>Reduced proper motion as a function of $(g - i)$ for the SDSS stars presented in Figure 3.3 (points and contours) and for members of our high-confidence candidate DWDs. Spectroscopically confirmed WDs are shown as blue stars, while the red stars lack spectra. The $V_T = 30$ km/s line marks the expected location of disk WDs and the $V_T = 150$ km/s line that of halo WDs (Kilic et al. 2006). All of our candidates lie in the expected region for WDs, far from the Main Sequence locus.</p>	65
3.8	<p>Projected separation of our high-confidence DWDs as a function of θ. We use the spectroscopically determined distances to the primary WDs to estimate s. Lines of constant distance are plotted as dashed lines.</p>	66
3.9	<p>DWD proper motions as a function of θ. Previously known systems are plotted as open stars, while our high-confidence pairs are filled stars. The dashed lines indicate the median μ and θ values for the previously known DWDs; our high-confidence systems are a significant addition to the sample of pairs with small μ and large θ.</p>	67

3.10 Normalized orbital separation distributions for the DWDs generated by our population synthesis (dashed line) and for the wide Main Sequence binaries identified by Dhital et al. (2010, solid line). For the latter, we use $a = 1.1 \times s$ to convert the observed (projected) orbital separations into true orbital separations (Dupuy & Liu 2011). The synthesized systems are those that remain after perturbing effects are taken into account (dashed line in Figure 3.1). The projected separations for the 12 high-confidence DWDs identified here have also been converted; their orbital separations are indicated by the arrows. 71

4.1 $(u - g)$ versus $(g - r)$ for $\approx 4 \times 10^4$ SDSS objects with $\sigma_{ugr} < 0.15$ mag, $\sigma_{iz} < 1.0$ mag, $\mu > 35$ mas yr $^{-1}$, and $\sigma_{\mu} < 10$ mas yr $^{-1}$. The plot boundaries define the box in color space within which we sought to identify new WDs. The sickle-shaped band corresponds to the DA cooling sequence, with hotter, younger WDs toward the upper left, and cooler, older WDs toward the bottom right. The width of the band is primarily due to variations in the DA masses: for example, WDs slightly more massive than the canonical $0.6 M_{\odot}$ have slightly higher surface gravities, and therefore slightly bluer $(u - g)$. The band of objects with bluer $(u - g)$ for a given $(g - r)$ is the cooling sequence for non-DA WDs. Hot DB WDs lie at the upper left of this band; as they cool to $\lesssim 12,000$ K they appear as DC WDs with featureless blackbody spectra. The red circles are the candidate WDs in 23 new candidate wide DWDs identified here; the green squares are candidate WDs in four additional new candidate systems, while the teal triangles are the WDs in the 13 known systems we re-detect. 79

- 4.2 Reduced proper motion H_r versus $(g - i)$ for the objects in Figure 4.1. The locus at $(g - i) \approx 2.5$ is of Main Sequence stars, while that at $(g - i) \approx 1$ is of subdwarfs. The spectroscopically confirmed WDs in the Kleinman et al. (2013) SDSS catalog with a measured μ are shown by the contours peaking at $(g - i) \approx -0.5$. We used the dashed line, adapted from Smith et al. (2009), to separate subdwarfs from candidate WDs. The solid lines represent the locations of WDs for transverse velocities $V_T = 30 \text{ km s}^{-1}$ (corresponding to the disk population) and 150 km s^{-1} (the halo population), and show that our candidates are likely in the Galactic disk. The symbols are the same as in Figure 4.1. Our candidates have systematically larger H_r because we require that they have relatively large μ and because the SDSS photometric catalog extends to fainter magnitudes than the spectroscopic catalog used by Kleinman et al. (2013) to identify WDs. 81
- 4.3 Angular separation (θ) distribution of our candidate common proper motion DWDs. The four pairs with $\Sigma^2 > 2$ but $\mu > 80 \text{ mas yr}^{-1}$ are shown in gray. The probability that a given pair is due to a random alignment should increase roughly linearly with θ . The dashed line shows the best fit line to the distribution beyond $100''$, where the noise dominates, assuming $N(\theta) \propto \theta$ and that the line goes through the origin. Extrapolating this fit to smaller θ suggests that pairs with $\theta < 100''$ are real pairs, while pairs at larger θ are physically unassociated. 82
- 4.4 Distribution in color space of spectroscopically confirmed QSOs (contours) and WDs (black dots) from SDSS (Schneider et al. 2010; Kleinman et al. 2013). The Girven et al. (2011) WD regions are overplotted. Blue dots indicate WDs from the 43 candidate wide DWDs that pass the selection criteria described in Section 4.2.2. The objects in both SDSS catalogs with UKIDSS (Lawrence et al. 2007) counterparts are also plotted in $(z-H)$ versus $(H-K)$ in the bottom right panel. The dashed line in that panel is $(z-K) = 1.3$ mag. While this line cleanly separates WDs from QSOs, the majority of our candidate WDs lack UKIDSS counterparts. Using SDSS photometry alone, $(u - g)$ versus $(g - r)$ colors provide the best constraints to separate QSOs from WDs. 84

4.5	<p>$(u-g)$ versus $(g-r)$ for photometrically identified candidate WDs binned by magnitude. The contours are the spectroscopically confirmed QSOs from the Schneider et al. (2010) catalog, while the solid line in the top two and middle left panels is the Girven et al. (2011) WD region. QSOs become a major source of contamination at fainter magnitudes and redder $(g-r)$. To identify fainter candidate WDs, we therefore added the constraint that for $g > 18$ mag, $(g-r) < -0.1$, resulting in the regions described by the solid line in the middle right and bottom two panels.</p>	85
4.6	<p>Angular separation distribution for astrometrically selected candidate DWDs. For $\theta \gtrsim 20''$, the number of matches increases linearly with θ, as expected for random alignments. The dashed line shows the best fit line to the distribution of random alignments beyond $50''$ where random alignments dominate, again assuming $N(\theta) \propto \theta$ and that the line goes through the origin. Extrapolating this fit to smaller θ shows that pairs with $\theta < 10''$ are excellent candidates for follow-up.</p>	87
4.7	<p>Total proper motion (μ) versus angular separation (θ) for candidate DWDs identified in our search for common proper motion pairs (filled circles), in Baxter et al. (2014, open circles), and in the literature (pluses). Although the Baxter et al. (2014) DWDs were also identified in SDSS, the overlap with our sample is small due to differences in the search techniques. Compared to other searches, we find systems with larger θ and μ.</p>	89
4.8	<p>Sample VLT, APO, and SDSS WD spectra. These DAs have T_{eff} of 10,000–15,000 K. The top two spectra were taken with the VLT ($R \approx 14,000$) and are not flux calibrated. The middle two were taken at APO ($R \approx 2500$) and the bottom two by SDSS ($R \approx 1800$). These WDs range from $g \approx 16$ (HS 2240+1234B) to ≈ 19 mag (J0859+3306B). The spectra here and in Figure 4.23 have been smoothed using a boxcar average of width 5.</p>	103
4.9	<p>Our model fits (red) to the APO spectra of six DA/DA pairs. The number of Balmer lines fit ranges from four to six, starting with $H\beta$ at the bottom. These fits are representative of the fits to all the WDs in our spectroscopic campaign.</p>	105

- 4.10 A comparison of T_{eff} and $\log g$ values derived by Baxter et al. (2014) with the values from our spectroscopic fits to the eight systems contained in both spectroscopic data sets. The dashed line shows the 1:1 correspondence. While the T_{eff} values are broadly consistent, our values appear to be slightly higher in most cases. By contrast, the $\log g$ values are well-matched for only half of the WDs and differ significantly for the other half, with no obvious trend in the differences. 106
- 4.11 Comparison of the M_{WD} of Baxter et al. (2014) and obtained from our spectra for 16 WDs in eight DWDs included in both spectroscopic samples. The dashed line shows the 1:1 correspondence. Our M_{WD} estimates are systematically larger by $\approx 0.05 M_{\odot}$, presumably due to the use of spectra with different resolutions and fitting codes with different model atmospheres. 111
- 4.12 Pre-WD lifetime (approximated by the age at the 1TP) as a function of initial mass. The solid line shows ages produced by our fiducial model, while the triangles show the results of MESA models generated varying a number of prescriptions. The lower panel shows that the pre-WD lifetimes produced by these tests are robust, as they typically vary by less than 5% even for very different models. 115
- 4.13 Converting M_i into pre-WD lifetimes. Finley & Koester (1997) assigned the more massive WD_B in PG 0922+162 a $M_i = 6.5 \pm 1.0 M_{\odot}$, which corresponds to a pre-WD lifetime of 43–90 Myr (we use our mesa stellar lifetime function here). Adding the τ_{cool} difference between the two WDs gives a pre-WD lifetime of 198–265 Myr for the less massive WD_A . We derive a corresponding $M_i = 3.89 \pm 0.20 M_{\odot}$ for WD_A ; Finley & Koester (1997) found $3.8 \pm 0.2 M_{\odot}$. Despite the relatively large uncertainty in the initial mass of WD_B , the uncertainty in the initial mass of WD_A is small, particularly compared to typical uncertainties derived from other observational methods. 118
- 4.14 A schematic summary of our method. Gray boxes indicate observed quantities. We convert each M_{WD} into a M_i using a candidate IFMR, and then find the corresponding pre-WD lifetime, τ , using the function shown in Figure 4.12. The difference of these lifetimes should be equal to $\Delta\tau_{\text{cool}}$, which we obtain from the two observed τ_{cool} . Our problem is then reduced to iterating over our model parameters to find the IFMR that makes this equality true for our set of wide DWDs. 120

4.15	The input mock IFMR is shown in red, while samples from the posterior are semi-transparent in gray. The posterior samples are evenly distributed around the input distribution.	129
4.16	Covariances between the four parameters in Θ_{IFMR} in our model for our mock data set. Lines indicate the input values for our parameters. Our posterior distributions are centered around the input parameters, indicating that our model converged to the correct solutions.	130
4.17	The top panel shows the covariance between the WD mass distribution model parameters μ_{WD} and σ_{WD} for our mock data set. The bottom panel shows a normalized histogram of the WD masses in our test sample. Lines show samples from the posterior distribution of model parameters.	131
4.18	Samples from the posterior distribution for our fiducial model are semi-transparent in gray. The model converges for the second linear component ($M_i = 2\text{--}4 M_{\odot}$), but diverges outside of this mass range.	132
4.19	Samples from the posterior distribution for our eight parameter model in which the pivot points for our three component piecewise model are allowed to vary. The results are consistent with the four parameter model: our DWDs constrain the IFMR between $\approx 2\text{--}4 M_{\odot}$	132
4.20	Covariances of the model parameters for our model applied to our sample of wide DWDs.	134
4.21	A comparison between samples from the posterior distribution from our fiducial model (gray lines) and theoretical IFMRs obtained from three separate stellar evolution codes. The differences between the codes are due primarily to treatment of the dredge-up and wind mass loss.	138
4.22	The top panel shows samples from the posterior distribution for our model (gray lines) and the observational constraints generated by WDs in four older open clusters (from Kalirai et al. 2014). The bottom panel compares the same posterior samples to the semi-empirical linear fits of Catalán et al. (2008a), Kalirai et al. (2008), and Williams et al. (2009).	138

4.23	The two top spectra are for the DBs in our sample: J0849+4712B (CDDS15-A) and J2355+1708B. The other spectra are for five DAHs: J0002+0733B, J0748+3025, J1412+4216B, J2044+4030A, and J2259+1404B. We do not include the SDSS spectra for PG 1258+593B and J1314+1732A, which show Zeeman splitting in the $H\alpha$ line, but not in the higher order Balmer lines.	147
5.1	Balmer absorption lines from $H\beta$ to $H8$ and the corresponding best fit spectral templates (from Tremblay et al. 2011a) for HS 2220+2146A and HS 2220+2146B. Spectra were taken by the SPY survey using the VLT with $R \approx 14,000$ and boxcar averaged with a width of 20 elements. T_{eff} and $\log g$ values and the corresponding M_{WD} and τ_{cool} are given in Table 5.1.	158
5.2	Using the best fit T_{eff} values from our spectral fits, we compare the SED of HS 2220+2146A and HS 2220+2146B with SDSS, 2MASS, and WISE photometry, normalized to the SDSS i band. 2MASS H and K photometry only provides upper limits. WISE cannot resolve the two WDs, and the W1 and W2 photometry (triangles) is for the combined DWD system. The WISE measurements, in particular, match the signal from just the WDs' blackbody radiation, precluding the existence of a hidden late-type stellar companion. In the inset figures, we focus on the visible component (SDSS $ugri$) of the SED. Note that here, we plot F_{λ} , not $\log F_{\lambda}$	161
5.3	The radial velocities for HS 2220+2146A (blue) and HS 2220+2146B (red) calculated from the follow-up spectra taken with the 1.5-meter FLWO. There is no apparent radial velocity variation due to a hidden binary companion. HS 2220+2146B has a larger average radial velocity (red dashed line) than its companion (blue dashed line) because its larger mass causes a larger gravitational redshift. The apparent radial velocity difference provides a consistency check for our spectroscopic solutions.	162
5.4	Our proposed formation history for HS 2220+2146 described in Section 5.3. The inner binary in a hierarchical triple system merged forming a blue straggler. The two stars then evolved independently, forming the WDs observed today. The provided timeline is inferred by working backwards from the observed WD cooling ages and stellar lifetimes assumed to form each WD. These are only rough times, rounded to the nearest 25 Myr.	165

5.5 The quadrupolar timescale given in Equation 5.2 as a function of the outer orbital separation, A_2 , for three different inner binary orbital separations, A_1 , of 0.1 AU, 1 AU, and 10 AU (we have assumed $e_2 = 0.1$). The horizontal dashed lines indicate 1/5th and 1/100th of 475 Myr, the calculated t_{merge} . Naoz et al. (2013) find that the inner binary typically merges between 5 and 100 t_{quad} , indicated by the gray, filled region between the two dashed lines. HS 2220+2146 is consistent with having been formed through the EKL mechanism if the system began as a hierarchical triple with $A_1 \approx 1$ AU and $A_2 \approx 200 - 500$ AU. 168

List of Tables

1.1	Stellar Clusters and their Associated WDs	15
2.1	Model Results	36
3.1	Initial Conditions for Population Synthesis	50
3.2	Candidate Wide DWDs with SDSS Spectra for Both Components	57
3.3	High-Confidence Candidate Wide DWDs	63
3.4	Wide DWDs – Derived Quantities	68
4.1	DWDs in the DR9 Footprint not Recovered in this Search	90
4.2	Wide Double White Dwarf – Observed Quantities	92
4.3	Fit Results for the DA/DA DWD Spectroscopic Sample	107
4.4	DA/DA DWDs Used to Constrain the IFMR	113
4.5	MESA Model Parameters	114
4.6	Mock Data Parameters	128
4.7	Fit Results for the non-DA/DA Spectroscopic Sample	149
5.1	Spectroscopic Fits	159
5.2	System Characteristics	160

(This page left intentionally blank.)

ACKNOWLEDGMENTS

This dissertation is the result of six years of research by many people. First among them is my advisor, Marcel Agüeros, who, more than anyone else, taught me how to be a scientist. His influence on me and the work here is unquestionable. Marcel taught me how to develop a scientific idea from its inception to its completion and the importance of expressing that idea with clarity, concision, and accuracy. Without his trust in my abilities and his encouragement to remain persistent in spite of inevitable road blocks, the work here would have fallen far short of its potential.

I began my transition into a scientist at my alma mater, Northwestern University, and two professors there deserve recognition. I want to thank Bill Halperin, who taught me the basics with dedication and sincerity, and Vicky Kalogera, who, over four separate summers of astronomy research, gave me my first taste of the rigors and satisfaction of studying the Universe.

I want to thank Jules Halpern, with whom I studied neutron stars in my first year at Columbia. I also want to specifically thank Mukremin Kilic, who was not only a collaborator, but also an advocate. Mukremin, and my other committee members, Jeno Sokoloski and Joe Patterson, could always be relied upon to freely share their knowledge without hesitation. I want to further thank three post-docs, Josh Peek, Tassos Fragos, and Francesca Valsecchi, with whom I have had the amazing luck to interact.

Without exception, the staff in the Astronomy Department, especially Mildred Kramer-Garcia and Ayoune Payne, were constantly available, and through their dedication, navi-

gating the difficulties of obtaining a Ph.D. became manageable.

I cannot thank my peers enough. Whether it was a small administrative question or a technical scientific question, the other graduate students at Columbia helped immensely. Among others, I want to specifically thank Alex Smith, Lauren Corlies, Christine Simpson, Lia Corrales, Andrew Emerick, Yuan Li, Adrian Price-Whelan, Ximena Fernández, Jenna Lemonias, Dan D’Orazio, David Hendel, Taka Tanaka, Aleksey Generozov, Sarah Pearson, Taka Tanaka, Duane Lee, Cameron Hummels, Maureen Teyssier, Destry Saul, Jennifer Weston, Kathryn Kreckel, Steven Mohammed, and Maria Charisi. Sharing my pains and joys, and being able to share in theirs, throughout six years in astronomy has meant everything.

Finally, I want to thank my sisters, Anne and Jane, and my parents, John and Linda. I could always count on their unwavering support.

2016, New York City

Dedication

For Ben

(This page left intentionally blank.)

Chapter 1

Introduction

Hydrogen-atmosphere (DA) white dwarfs (WDs), the evolutionary endpoints for stars with Main Sequence (MS) masses less than roughly $8 M_{\odot}$, are second in number only to low-mass MS stars in the solar neighborhood (Rowell & Hambly 2011). However, while they can remain at relatively high temperatures for Gyr, WDs are small and therefore usually faint objects, so that assembling complete catalogs of WDs has historically been challenging. For instance, of the roughly 6000 naked eye stars in the entire sky only a few dozen have intrinsic luminosities fainter than our Sun and none are WDs. Fully aware that a volumetric stellar sample would produce drastically different statistics, Willem Luyten devoted his career to identifying nearby, intrinsically faint stars, generating a census of the nearby stellar population (Ungren 1996).¹

¹Incidentally, Luyten coined the term “white dwarf” in 1922 (Holberg 2005).

1.1 A Brief Observational History of White Dwarfs

Luyten developed a technique to differentiate between types of stars using a quantity created by Ejnar Hertzsprung called reduced proper motion, H :

$$H = m + 5 \log(\mu) + 5, \quad (1.1)$$

where m is the apparent magnitude and μ is the proper motion. One can make the substitution $\mu = V_{\text{trans}}/D$, where V_{trans} is the transverse velocity in units of length per time, and D is the physical distance. When apparent magnitude is converted to absolute magnitude M , we can express H as:

$$H = M + 5 \log(V_{\text{trans}}). \quad (1.2)$$

Since V_{trans} is typically small (hypervelocity stars are an obvious, important exception), H serves as a proxy for M . It was shown early on that H can be used to effectively differentiate between dwarf and giant stars (Stromberg 1939). If all stars had equivalent V_{trans} , a reduced proper motion diagram, which shows the relation between H and photometric color, would be equivalent to a color-magnitude diagram (Salim & Gould 2002).

Since they are intrinsically faint objects, WDs have a large H and are therefore easily identified using reduced proper motion diagrams. This requires measurements of μ which is observationally challenging since throughout much of the 20th century, astronomy was based on photometric plates and the sensitivity of measurements of μ is dependent upon both the astrometric precision and the time baseline between observations.

Between 1896 and 1910, the Bruce telescope in Ariquepa, Peru, photographed nearly the entire southern sky, reaching stars as faint as 17th mag (Pickering 1899; Upgren 1996). Starting in 1927, Luyten began the Bruce Proper Motion Survey to re-image these stars and search for proper motions and hence measure H (Luyten 1987). Stars with proper motions were identified using a “blinking” technique in which images of the same region of the sky were blinked back and forth until high proper motion stars that had moved between the two images were identified. The final catalog contained nearly 100,000 high proper motion stars (Luyten 1963).

Luyten teamed up with Guillermo Haro to take *UBV*-filtered images of stars near the South Galactic Pole (Haro & Luyten 1962). Figure 1.1 shows a sample plate from their survey; they exposed the same plate to all three filters, slightly shifting the plate position between exposures so each star appears as a triplet, ordered as *B*, *V*, and *U* from left to right. The arrow points to a star in the middle (PHL 384), which shows a clear excess in the UV. Although their method was highly subjective and introduced a number of data analysis hurdles, their catalog identified over 8000 faint blue stars (Haro & Luyten 1962).² Unfortunately, only roughly 300 of these stars had proper motions large enough to be measured in Luyten’s catalogs. Nevertheless, Haro and Luyten were able to identify 12-15 WDs, thus establishing the basic method for identifying WD candidates: **cross-match multi-band photometric catalogs with proper motion catalogs to find blue stars with large proper motions.** The methods used to identify WD samples throughout the remainder of this work follow this same basic premise.

With a grant from the *National Geographic*, Luyten expanded his survey to fainter mag-

²Interestingly, this catalog contained some 36 “white or blue double stars.”

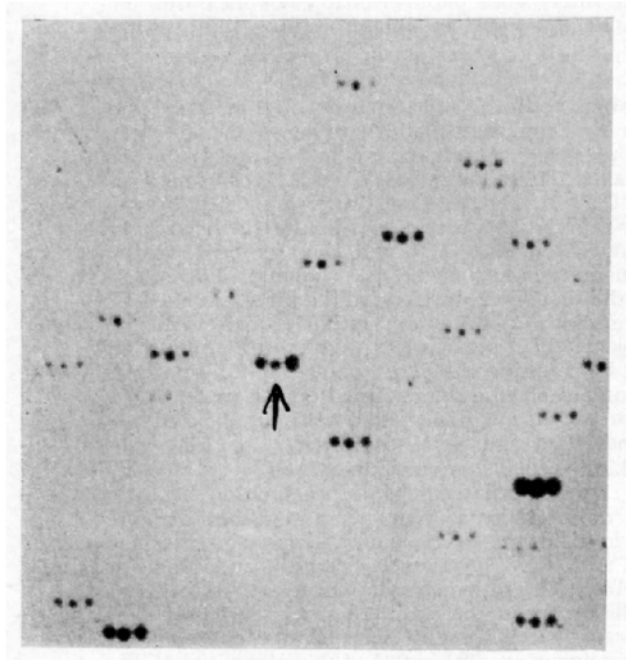


Figure 1.1 A sample photometric plate from the data set of Haro & Luyten (1962). The photometric plate was exposed three separate times using, from left to right, *B*, *V*, and *U* filters, so each star appears as a triplet. The arrow points to the star PHL 384, a star with a *B* and *U* excess.

nitudes in the Northern Hemisphere. In lieu of blinking images, Luyten commissioned the construction of a machine (rapid-scanning microdensitometer) that could measure and blink the images automatically (Upgren 1996). His New Luyten Two Tenths Catalog (NLTT) contained some 60,000 stars with proper motions greater than $0.2'' \text{ yr}^{-1}$ (Luyten 1979). Since its publication, various researchers have spectroscopically confirmed many of the WD candidates within the NLTT catalog (e.g., Kawka & Vennes 2005). These were collected, along with spectroscopic WDs from other studies, in the Villanova WD Catalog (McCook & Sion 1977, 1987, 1999).

1.2 Modern White Dwarf Observations

The last decade has seen an impressive growth in our ability to find and characterize WDs, largely thanks to efforts by spectroscopic surveys such as the Palomar Green survey (PG; Green et al. 1986) and the Sloan Digital Sky Survey (SDSS; York et al. 2000). The PG survey contains 348 WDs (Liebert et al. 2005a). The first SDSS WD catalog included 2551 WDs (Kleinman et al. 2004); the second nearly quadrupled that number, and included 6000 new, spectroscopically confirmed WDs (Eisenstein et al. 2006a). The SDSS Data Release 7 (DR7; Abazajian et al. 2009) again doubled the size of the WD catalog, bringing the total to $\sim 20,000$ WDs (Kleinman et al. 2013). The most recent SDSS WD catalog from DR10 includes nearly 30,000 spectroscopically identified WDs (Kepler et al. 2015). In the modern age of large-scale surveys, obtaining large WD spectroscopic samples is no longer an observational hurdle.

Although a number of techniques, such as trigonometric parallax or gravitational redshift, exist to measure the mass of a DA WD, Bergeron et al. (1992) established the spectroscopic method as the standard. This method obtains the effective temperature, T_{eff} , and the surface gravity, $\log g$, by comparing line profiles from atmospheric models to the observed Hydrogen Balmer line absorption profiles. When combined with a mass-radius relation, the WD mass, M_{WD} , can be measured. By applying this technique to the thousands of WD spectra produced by the PG survey and SDSS, bulk statistics about WDs were obtained. For instance, studies confirmed that the DA M_{WD} distribution is strongly peaked at $0.6 M_{\odot}$ with small but important outlier populations at $M \lesssim 0.4 M_{\odot}$ and $\gtrsim 1.0 M_{\odot}$ (Liebert et al. 2005a; Kepler et al. 2007; Tremblay et al. 2011b; Kepler et al. 2015).

1.3 Short Period WD Binaries

How are these WD populations with significantly smaller and larger masses formed? Some of the higher-mass WDs may have formed through standard single-star evolution from higher-mass stars. Many of these, however, were likely formed through binary interactions. Stellar binaries come in many flavors, but one possible end state is a double white dwarf (DWD), a binary in which both components have evolved into WDs. If their combined mass is below the Chandrasekhar limit and the orbital period, P_{orb} , is small enough, a DWD may merge due to gravitational wave radiation, forming a high mass WD (García-Berro et al. 2012).

Less-massive WDs were probably formed through binary evolution channels as well. Except in cases of extreme metallicity (Kilic et al. 2007), the Galaxy is not old enough to produce low-mass white dwarfs (LMWDs; $M < 0.45 M_{\odot}$) through single-star evolution. Indeed, with few exceptions follow-up observations consistently find companions to LMWDs (Marsh et al. 1995; Maxted et al. 2000; Nelemans et al. 2005; Rebassa-Mansergas et al. 2011). Instead, LMWDs are expected to form through a common envelope (CE; Han 1998; Nelemans et al. 2000, 2001a; van der Sluys et al. 2006; Woods et al. 2012).

A CE occurs when a star in a close binary enters unstable mass transfer, typically when a star expands upon evolving into a first ascent or asymptotic giant branch (AGB) star (for a recent review, see Ivanova et al. 2013). Due to their large convective envelope, giant stars have a very low entropy gradient, so that when mass is removed (by overflowing its Roche lobe during mass transfer), the star will try to maintain hydrostatic equilibrium by adiabatically expanding. This expansion leads to more mass loss, which in turn causes

the star to expand. The process forms a positive feedback loop and quickly runs away to instability. Hydrodynamic drag and (in most cases) mass transfer conspire to rapidly shrink the binary. Orbital energy is tapped to gravitationally unbind the giant star's envelope, leaving the system as a close binary composed of the core of the giant star and its companion in a much tighter orbit, possibly by as much as or more than an order of magnitude. Exactly how much the orbit shrinks (usually quantified as how efficiently the orbital energy can be used to remove the giant's envelope) has been the subject of much work on binaries over the past several decades (De Marco et al. 2011).

LMWDs comprise a unique sample with which to constrain this efficiency. The Extremely Low Mass WD Survey has identified 61 LMWDs in SDSS and elsewhere (Brown et al. 2010; Kilic et al. 2011; Brown et al. 2012; Kilic et al. 2012; Brown et al. 2013). Because of the high-resolution spectra over multiple epochs compared with state-of-the-art spectral templates, precision P_{orb} , M_{WD} , and mass function measurements are available for these WDs. Since each of these WDs is the direct result of a CE, this high quality data set has the potential to test CE theory in new ways.

One of the difficulties of using these binaries is that, although we can measure M_{WD} , P_{orb} , and the WD's maximum radial-velocity variation, we cannot directly measure the companion's mass due to the unknown inclination angle. In Andrews et al. (2014), we approached this problem statistically. We utilized the fact that inclination angles are not evenly distributed (an edge-on orbit is more likely than a face-on orbit) to constrain the overall population of companions to ELM WDs. We employed a Bayesian statistical model and used a Markov Chain Monte Carlo algorithm to make these constraints. We found

that most ELM WDs have relatively massive WD companions, with $M > 0.7 M_{\odot}$, an unexpected result when compared to theoretical studies of close DWDs (Toonen et al. 2012). Furthermore, we showed that a small but not insignificant set of ELM WDs could have pulsar companions. We are currently engaged in searches for putative pulsar companions around ELM WDs, looking for both pulsed radio emission and surface blackbody X-ray emission. This study constitutes Chapter 2.

1.4 Wide DWDs

If ELM WDs, with their extremely tight orbits, form one end of the DWD binary spectrum, wide DWD binaries, with orbital separations of 10^3 AU and larger, form the other. These binaries provide a unique perspective on stellar evolution: for those with orbital separations $a \gtrsim 10^2$ AU, the coeval components are far enough apart that mass exchanges are unlikely to have significantly impacted their individual evolutions (Silvestri et al. 2001; Farihi et al. 2006). Wide DWDs with precise cooling ages, masses, and (projected not physical) binary separations have the potential to uniquely constrain certain stellar and Galactic physics:

- By identifying three wide DWDs, the faintest such systems discovered at that point, Hintzen et al. (1989) calculated WD cooling ages in excess of several Gyr. In the case of the system LP 197-5/6, they found a cooling age, τ_{cool} , of 8 Gyr, important evidence supporting the conclusion by Winget et al. (1987) that the Galactic disk has an age in excess of 9 Gyr.

- In their study of a larger sample of 21 wide DWDs, Sion et al. (1991) argued that the orbit of a binary should expand upon mass loss. With statistically significant populations of wide MS-MS, MS-WD, and WD-WD binaries, wide DWDs could provide tests of the effects of mass loss on a binary orbit, after observational biases are taken into account.
- Sion et al. (1991) further discussed the possibility for the widest DWDs to constrain the cumulative effects of nearby objects perturbing relatively fragile wide DWDs; a wide binary may become unbound due to perturbations by passing stars, nearby giant molecular clouds, and even the differential Galactic potential causing a Galactic tide (Weinberg et al. 1987; Jiang & Tremaine 2010). In their sample of MS-MS binaries, Dhital et al. (2010) observe a falloff in the number of wide disk dwarf binaries as orbital separations increase, which these authors argued is due to disrupted binaries.
- Finally, Finley & Koester (1997) used the wide DWD PG 0922+162 to test the initial-final mass relation (IFMR; the relation between a MS star's mass and its final, WD mass). This method is of primary importance to this dissertation, and we discuss their work in depth in Section 1.5.5.

Despite their value for addressing certain stellar and binary evolution problems, the population of wide, resolved DWDs remains mostly unexplored, largely because of the observational challenges these types of binaries present. Their orbital periods are much longer than human lifetimes, and therefore members of these systems can only be identified astrometrically. Here again, Luyten developed the predominant method to identify wide binaries by searching for pairs of astrometrically close stars with matching

proper motions (see for example the discussion in Luyten 1988). The resulting pairs are known as common proper-motion binaries (CPMBs). This method is now commonly used and generally relies on high-proper-motion, magnitude-limited catalogs, so that searches for CPMBs tend to uncover nearby stars (Dhital et al. 2010, and references therein).

The first wide DWD was identified by Sanduleak & Pesch (1982) by comparing an observation of a pair of WDs with a Palomar Sky Survey plate from 1955 and taking spectra of the WDs. Greenstein et al. (1983) quickly followed up with CCD spectra of the pair, measuring T_{eff} , M_{WD} , and τ_{cool} for each of the WDs (although their quoted numbers are inaccurate due to the crude WD atmospheric and cooling models available at the time). They attempt to describe the evolutionary history of the WD pair, claiming that the overall system age should be the same for each WD. The analysis of Greenstein et al. (1983) was ahead of its time; these authors link their observed masses with the best IFMR available at the time (from Weidemann 1977) to get MS masses. They further discuss the consequence of having different initial stellar masses with different lifetimes lead to differences in the WD cooling ages. Unfortunately, their work was fundamentally flawed. Maxted et al. (2000) showed that one of these WDs is actually an unresolved close DWD, making this system not the first wide DWD, but the first known triple WD. Due to the potential for prior mass transfer phases within the close pair, which would affect both the observed mass and cooling ages, the assumption of independent evolution is incorrect.

Following Sanduleak and Pesch's success, Greenstein (1986c) identified six wide double degenerates from his sample of 319 WDs confirmed with spectrophotometry (Greenstein 1984). Calling these the "rarest and most interesting" visual binaries, which have

“special evolutionary significance,” Greenstein (1986a) noted that both WDs in each of the five pairs (the Sanduleak and Pesch binary is the exception) are consistent with having identical overall ages, but WD cooling theory was still not sufficiently developed to make strong conclusions.

Prior to the work presented here in Chapter 3, the study by Sion et al. (1991) was the last comprehensive search for wide DWDs. Their work was still limited to searching the available catalogs from Luyten and Giclas. Several wide DWDs were serendipitously discovered in other surveys, for instance by Farihi et al. (2005) in these authors’ search for faint (not necessarily white) dwarf stars in the PG survey. Additionally of note, an amateur astronomer identified eight WDs with proper motion companions in SDSS Data Release 1, two of which are in DWDs (Greaves 2005). Altogether, there were 35 known wide DWDs identified throughout the literature prior to Andrews et al. (2012).

In that paper we engaged in a search for wide DWDs in SDSS, following the techniques developed by Luyten, Greenstein, and Sion et al. (1991). SDSS’s large number of sources, combined with its high-precision astrometric and photometric measurements gives it a distinct advantage over previous data sets to search for blue objects with large proper motions. The spectroscopic survey from SDSS allowed us to adapt and improve previous search techniques; we used the spectroscopically confirmed WD catalog from Data Release 7 (Kleinman et al. 2013) as a starting set. We then searched for blue objects with high proper motions around these spectroscopic WDs. Using two separate techniques to eliminate randomly aligned stars, we were able to identify 12 new wide DWDs. This study gave us confidence that we could effectively identify wide DWDs and

eliminate false positives from our searches.

In Chapter 4, we adapt our method from Andrews et al. (2012) to search for wide DWDs in the SDSS Ninth Data Release (DR9). DR9 has some 260 million unique objects, nearly double the size of DR7. In this study, we use two methods to identify wide DWDs. First, we search for pairs of blue stars with matching proper motions, and second, we search for pairs of astrometrically close blue stars. We use photometric constraints to discern WDs from subdwarfs, quasars, and early-type stars. Using these two methods, we identify 65 new wide DWDs, bringing the total to 142 candidate or spectroscopically confirmed wide DWDs. We present the details of this search in the first half of Chapter 4. In the second half of Chapter 4, we show how, with this much larger sample, we can constrain the IFMR.

1.5 Initial-Final Mass Relation

Robust observational constraints on the IFMR are difficult to make since the evolution from a MS star into a WD occurs on a timescale much longer than the history of human civilization. Constraints on this relation must therefore be made in an indirect way. There are five major methods used to place constraints on the IFMR which we discuss briefly here.³

³There are a number of additional, lesser used methods of constraining the IFMR that I will not discuss here. One notable example is an unproven method alluded to by Parker (2011) who plan to model a planetary nebula associated with an open cluster

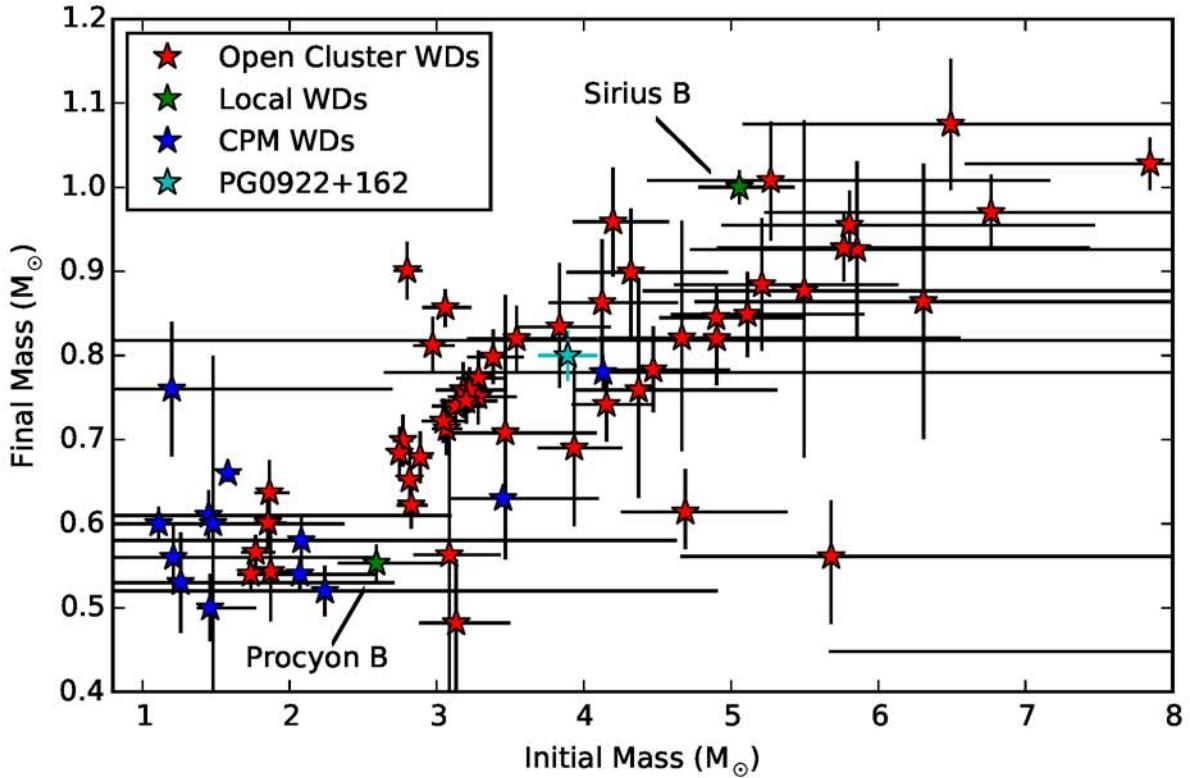


Figure 1.2 Constraints on the IFMR from Method 1 using WDs in clusters (red) and Method 4 using WDs in common proper motion pairs (blue). We also show constraints from the nearby WDs Sirius B and Procyon B (green). Finally, we show the IFMR constraint from the wide DWD PG 0922+162 (teal).

1.5.1 Method 1: WDs in Clusters

From early on, WDs were discovered in open clusters, first in the Pleiades (Luyten & Herbig 1960), then in the Hyades (Luyten 1963; Eggen & Greenstein 1965). Auer & Woolf (1965) quickly realized that at least some stars more massive than the Hyades turn-off mass ($M_i \approx 3.5 M_\odot$) must evolve into WDs, and that if the association of a WD with the Pleiades was to be believed, then stars as massive as $7 M_\odot$ form WDs.

It was Sweeney (1976) who first reversed this relation: any WD in a cluster had to

have originated from a star initially more massive than the cluster's turn-off mass. By measuring the T_{eff} of the WD and converting that into a cooling age, one could obtain the pre-WD lifetime by subtracting the WD's cooling age from the cluster age. Applying a stellar lifetime function, the star's initial mass could be quantified from the pre-WD lifetime. Unfortunately, obtaining WD masses was difficult at the time, and different measurement methods often disagreed substantially.

In their early review, Weidemann & Koester (1983) discussed the difficulty of placing constraints on the IFMR. At the time it was straightforward to identify blue objects in open cluster fields using multi-band photometry, but confirmation that these objects were WDs required spectroscopic follow-up. Most importantly, cluster membership has been notoriously troublesome to determine, particularly for widely dispersed open clusters such as the Hyades. The survey by Romanishin & Angel (1980) provides an elucidating example. These authors searched photometric plates of the open clusters NGC 2168, 2287, 2422, and 6633 for blue objects, identifying 17 candidates. However, in a spectroscopic follow-up campaign, Koester & Reimers (1981) could only show that four of these were WDs, at least one of which was probably a foreground WD. Even today, with modern CCD observations, identifying bona fide WD members of open clusters is difficult.⁴ Nevertheless, this method is arguably the most straight-forward, and prolific; roughly 50 WDs have been studied in this manner (e.g., Kalirai et al. 2005; Rubin et al. 2008). Table 1.1 summarizes the known WDs in clusters used for constraining the IFMR. Figure 1.2 shows the constraints (from Salaris et al. 2009) that these WDs place on the IFMR.

⁴As an illustration, in a recent study, Casewell et al. (2015) searched for WDs in the open cluster α Per, finding 10 WDs, none of which are associated with the cluster.

Table 1.1 Stellar Clusters and their Associated WDs

Cluster	# of WDs	Age ^a	References ^b
Pleiades	1	85 Myr	D06
NGC 2168 (M35)	6	120 Myr	W04, W09
NGC 2516	4	150 Myr	K96
NGC 2287	4	243 Myr	D12
NGC 1039 (M34)	3	250 Myr	R08
NGC 3532	7	300 Myr	K96, D09, D12
NGC 2099 (M37)	12	320 Myr	K05, C15
Hyades	7	640 Myr	D04
Praesepe	11	650 Myr	D04, D06
NGC 7789	3	1.5 Gyr	K08
NGC 6819	2	2.0 Gyr	K08
M4	6	11.6 Gyr	K09

^a Where available, ages are from Salaris et al. (2009).

^b References: D06 – Dobbie et al. (2006); W04 – Williams et al. (2004); W09 – Williams et al. (2009); K96 – Koester & Reimers (1996); D12 – Dobbie et al. (2012b); R08 – Rubin et al. (2008); D09 – Dobbie et al. (2009); K05 – Kalirai et al. (2005); C15 – Cummings et al. (2015); D04 – Dobbie et al. (2004); K08 – Kalirai et al. (2008); K09 – Kalirai et al. (2009).

Several aspects of Figure 1.2 are concerning. First, at the high-mass end, the relation is poorly constrained. At these masses, the difference in stellar lifetimes are of order the uncertainties in cluster ages. Even more concerning is the presence of several discrepant data points lying far from the general increasing trend at the bottom right and top left of Figure 1.2. It is possible that some of these are contaminating WDs that have been incorrectly assigned as cluster members. Even if these are eliminated from the plot there appears to be a spread in the IFMRs. It is unclear whether this is due to a real spread in the IFMR or simply to noise, but there appear to be indications that metallicity, at least, will lead to different IFMRs (Kalirai et al. 2005; Meng et al. 2008).

Some of the discrepancies in these data points may be due to the difficult-to-model systematics involved, particularly those introduced when estimating open cluster ages. As pointed out by Salaris et al. (2009), ages for key clusters used in this analysis (e.g., the Hyades and Pleiades) are often adopted from multiple sources, which in turn often have used completely different stellar evolution codes to generate their isochrones. Furthermore, when Salaris et al. (2009) test different isochrones to assign self-consistent ages to the clusters, these authors uncover another problem, which is that uncertainties in the basic cluster parameters (e.g., reddening or metallicity) also contribute significantly to uncertainties in the derived ages.

Finally, for $M_i < 3 M_\odot$, there are very few data points. This is due to the difficulty of finding WDs within the relatively few nearby open clusters old enough for these less massive stars to have evolved into a WD. Table 1.1 shows that most WDs are found in open clusters younger than ~ 650 Myr. This is a serious problem, since the field WD population is very narrowly peaked around $0.6 M_\odot$ (see discussion in Section 1.2 Kleinman et al. 2013), which evolve from stars with $M_i < 3 M_\odot$. Future observations of WDs in the older open clusters M 67 and NGC 188 could help.

1.5.2 Method 2: AGB Star Population Models

The second method used to constrain the IFMR involves modeling populations of the progenitors of WDs, AGB stars.⁵ This method relies on the fact that a WD evolves from the core of an AGB star, and it is assumed that the core mass does not change in the transition

⁵While the majority of IFMR constraints use whole populations, there are some attempts to place constraints from individual AGB stars. For instance, Bedijn (1988) attempted to model mass loss from individual O-rich AGB stars to determine their core mass, and hence future WD mass.

into a WD. While mass loss on the AGB phase is complicated to model, observations of large populations can probe it. Aaronson & Mould (1985) collected data on some two dozen clusters in the Magellanic Clouds, observing both the luminosity of the tip of the AGB and fitting for the cluster age. By converting the cluster age to a stellar lifetime, they determined the initial masses of those stars at the tip of the AGB, the immediate progenitors of WDs. Using a core-mass luminosity relation, Aaronson & Mould (1985) converted the luminosity to a core (and hence WD) mass. These data produced constraints on the IFMR for $M_i \approx 1 - 2 M_\odot$, a range difficult to probe using Method 1 described above.⁶

Reid & Mould (1984) and Reid & Mould (1985) developed a theoretical model based on the same idea. These authors were interested in the AGB luminosity function for the Large Magellanic Clouds, particularly to constrain recent star formation and determine the amount of material reprocessed through AGB winds. Using a star formation rate (SFR), an initial mass function (IMF), and a model for AGB evolution, they generated synthetic populations of AGB stars, then fit these to LMC observations. Using a core mass-luminosity relation allows a conversion from luminosity to core mass, and hence core mass evolution along the AGB.

As discussed by Weidemann (1987), this method faces a number of difficulties. First, it depends on observational selection effects that could change the observed AGB populations. More ruinous, however, is that this method is strongly dependent upon stellar evolution models, in particular an accurate core mass-luminosity relation, which Herwig et al. (1998) showed is not universal due to complexities in late stage stellar evolution.

⁶It appears that Frantsman (1986) and Frantsman (1988) may have done something similar, explicitly showing that certain IFMRs could not explain the population of AGB stars in the Magellanic Clouds. Unfortunately I have not been able to obtain access to these articles.

Due to these uncertainties, this method has largely been abandoned. Most recently, however, Girardi et al. (2010) compared AGB populations of 12 metal-poor galaxies (with very large number statistics) to modern AGB evolution models. Their best fit models show that stars with $M_i \approx 1 M_\odot$ produce WDs with $M = 0.51 - 0.55 M_\odot$. It seems this method is best applied to the older AGB stars in globular clusters and nearby galaxies with statistically large stellar populations.

1.5.3 Method 3: WD Population Models

Koester & Weidemann (1980) demonstrated that WDs are important probes of Galactic evolution; using different IMFs, SFRs, and IFMRs, they compared the synthesized populations of WDs with the observed WD mass distribution and formation rates. Although their statistics were too poor to discern between various IFMRs, they demonstrated that large samples of WDs could constrain Galactic evolution.

The number of WDs expanded substantially with improved observational techniques, and Yuan (1992) performed an extensive study comparing synthesized WD populations with observed WD mass distributions, space densities, and luminosity functions. They found that the detailed shape of the IFMR, particularly in its lower part, has the strongest impact on the WD mass distribution. In their study of the IFMR, Catalán et al. (2008a) agree, explicitly showing that different IFMRs substantially affect WD luminosity functions. Using a greatly expanded sample of WDs from the PG survey, Liebert et al. (2005a) followed the calculation by Yuan (1992) and performed a basic population synthesis calculation, but fell short of an extensive parameter study.

Recently, Dawson & Schröder (2012) (see also Schröder et al. 2004) attempted a comparison between the volume complete sample of WDs within 13 pc (Holberg et al. 2008). Although this sample only contained 13 single WDs, Dawson & Schröder (2012) extrapolated to generate a synthesized population of WDs within 100 pc. Unfortunately, their statistics are not large enough to place strong constraints on the IFMR. Similar recent studies of the larger WD populations in 47 Tuc (García-Berro et al. 2014) and the Galactic disk (Cojocaru et al. 2014; Torres et al. 2014) typically adopt an IFMR, without testing different relations. In the future, these studies could be expanded to explicitly model different IFMRs.

While modeling statistically large populations of WDs has the potential to place strong constraints on the IFMR, Yuan (1992) pointed out that such studies are strongly dependent upon a number of assumptions as well as significant observational biases. Large, well-studied populations such as those in the nearby globular clusters 47 Tuc (García-Berro et al. 2014) and M4 (Kalirai et al. 2009) may be complete enough to provide stringent constraints in the near future. With modern samples of WDs, such as that from SDSS or the upcoming population from *Gaia*, stronger constraints may soon be possible.

1.5.4 Method 4: Wide (Non-Double) WD Binaries

Identifying five separate wide binaries containing a WD and a MS star, Wegner (1973) came up with a new method of constraining the IFMR. Assuming the two stars in a wide binary are coeval and separated far enough that no mass has been exchanged, he argued that the age of the system could be determined from isochrone fits to the MS star. Subtracting the

WD cooling age would then give the stellar lifetime of the WD progenitor. Combined with stellar evolution codes, this lifetime could be converted to a MS mass. Unfortunately, at the time stellar evolution theory and WD models were still poorly constrained, and both the WD mass and its derived progenitor mass suffered from large uncertainties.

This method was then largely ignored until it was taken up by Catalán et al. (2008b), who placed constraints on six WDs in wide binary systems with MS and post-MS companions. To determine the age of the companion to the WD, these authors used a combination of isochrone fits, metallicity indicators, and X-ray luminosity. More recently, Zhao et al. (2012) performed a similar analysis using an expanded sample of 10 WDs in wide binaries. Figure 1.2 shows the constraints from the 11 systems studied from this method. Because precisely dating a MS or evolved star is difficult, the constraints from this method typically have very large uncertainties.

Importantly, there are three WD binaries in the stellar neighborhood to which this method has been applied: Sirius (Barstow et al. 2005; Liebert et al. 2005b), 40 Eri (Weidemann 1977), and Procyon (Liebert et al. 2013). We show the constraints from Sirius B and Procyon B in Figure 1.2. Since these systems are all close to the Sun, precise radii and masses measurements allow the WD companions' ages to be determined. Sirius B provides a very important constraint; however, one should approach the derived constraints from Procyon B and 40 Eri with caution. 40 Eri is actually a triple system with its nearest neighbor some $7000 R_{\odot}$ away, and there was likely some interaction between the stars in the past. Procyon B is a DB WD, and there is some uncertainty about its mass and cooling age (see Liebert et al. 2013, and references therein).

As currently implemented, this method still leaves much to be desired: all methods to estimate MS star ages seem to suffer from large uncertainties. Recent work has focused on identifying wide systems composed of WDs with evolved, subgiant companions (J. Chanamé, priv. communication), which have substantially more precise isochrone-derived ages. The key is identifying populations of wide binaries in these relatively short lived phases, which is now possible with current large-scale surveys. Accurate distances from the upcoming release of *Gaia* astrometry may soon give this method more traction.

1.5.5 Method 5: Wide Double White Dwarfs

Using the wide DWD Sanduleak A/B, Greenstein et al. (1983) built the foundation upon which constraints on the IFMR can be placed using wide DWDs. They took spectra of both WDs and fit for the equivalent widths of Balmer lines. Using WD models they then matched the widths to T_{eff} and $\log g$ and hence M_{WD} and τ_{cool} solutions. They argued that since the overall lifetime of the system should be the same for each star, and that for each star, the overall lifetime is the sum of the cooling age and the stellar lifetime. Estimating a cooling age difference of 1.1×10^8 yr, Greenstein et al. (1983) argued that this should also be the difference in the stellar lifetime. Ultimately, they concluded only that the more massive WD must have come from a star initially more massive than $4 M_{\odot}$. At the time, the maximum initial mass producing a WD was still relatively unconstrained. While their conclusion was ultimately correct, the Sanduleak A/B system has since been shown to be a triple system (Maxted et al. 2000); the less massive component of the binary is actually composed of a close binary WD system. Because mass transfer significantly affects the

both the mass and cooling timescale of the system, the Greenstein et al. (1983) assumption that each star evolves like a single star is incorrect.

The same basic analysis was used on the wide DWD PG 0922+162 by Finley & Koester (1997). These authors compared the more massive WD ($\gtrsim 1.10 M_{\odot}$) to similarly massive WDs in open clusters for which M_i had been published, thereby obtaining $M_i = 6.5 \pm 1.0 M_{\odot}$ for this WD. Finley & Koester (1997) converted this mass into a pre-WD lifetime of 42–86 Myr, to which they added the τ_{cool} of the massive WD to derive a system age of 320 ± 32 Myr. Finley & Koester (1997) then used the less massive WD in PG 0922+162 to constrain the IFMR: they derived a pre-WD lifetime for this WD of 231 ± 34 Myr by subtracting its τ_{cool} from the system age, and obtained $M_i = 3.8 \pm 0.2 M_{\odot}$ for its progenitor. Because the relation between lifetime and mass is steeper for longer-lived/lower-mass MS stars, even relatively large uncertainties in the assumed M_i for the more massive WD in PG 0922+162 results in stringent constraints on the M_i of the less massive WD. Figure 1.2 shows that the uncertainty on this point in the initial-final mass plane is comparable to that for the best data obtained using Method 1.

Recently, Girven et al. (2010) applied this method to PG 1258+593 to constrain the initial mass of its magnetic companion SDSS J130033.48+590407.0. While of use for studying the origin of magnetic WDs (e.g., Dobbie et al. 2012b), magnetic WDs may be formed through alternative evolutionary channels compared with the standard, non-magnetic WDs (magnetic WDs may be the result of merging WDs, c.f. García-Berro et al. 2012).

Most recently, Catalán (2015) produced constraints using a sample of wide DWDs identified in SDSS DR9. Their method, while promising, has produced only four systems

with meaningful constraints from a sample of 14 systems.

One of the difficulties in applying the Finley & Koester (1997) method to a larger sample of DWDs is that the first step was comparing the more massive WD in PG 0922+162 to massive WDs in open clusters, something that cannot be done for a generic set of DWDs. Yet, with an optimal system, the constraint is very powerful. Indeed, the Finley & Koester (1997) result is one of the most stringent constraints on the IFMR, and is one of the reasons why Weidemann (2000) anchored his semi-empirical IFMR at $M_i = 4.0 M_\odot$ and $M_{\text{WD}} = 0.80 M_\odot$.

In Andrews et al. (submitted) we develop a new method to constrain the IFMR using our sample of 142 wide DWDs. This method allows every well-characterized system to be used. We employ a parameterized form of the IFMR and determine which parameter values best explain the cooling age and mass differences in the ensemble of wide DWDs. We describe the details of this method in the second half of Chapter 4.

1.6 Triple Systems

It is commonly stated that only half of all stars are born and evolve alone; the other half are found in binary or higher order stellar systems. In their study of stars in the *Hipparchos* catalog, Raghavan et al. (2010) estimate that roughly 33% of stars are in binaries and 8% are in triples. If DWDs are the endpoints of binary evolution, triple WDs form the endpoints of triple stellar evolution. Indeed, in our sample of 142 wide DWDs, there are two spectroscopically confirmed triple degenerate systems, Sanduleak A/B (Maxted et al. 2000) and G 21-15 (Farihi et al. 2005). In our more recent search for wide DWDs described in

Chapter 4, we identified a third candidate triple system, PG 0901+140. These systems are composed of an unresolved pair of WDs, with a widely separated, visual WD companion. The inner binary in each of these systems contains a LMWD, indicating that the inner binary interacted, likely through a CE as we previously described. Reipurth & Mikkola (2012) argue that hierarchical triple systems may be the natural result of energy exchange in newborn triple systems: the inner binary tightens, while the outer companion's orbit expands. If the inner binary survives any phase of mass transfer or dynamical interaction and all three stars have had enough time to completely evolve, the system will form a triple degenerate.

While these triple degenerate systems survived the inner binary interacting, some systems may also exist in which the inner binary merged, forming a blue straggler, with an outer, binary companion. Such systems would then evolve into wide DWDs, but these would look different from those wide DWDs forming from a stellar binary. In a standard binary system, the more massive star in the pair evolves first into a WD more massive than that of its less massive counterpart. Interestingly, in our sample of wide DWDs described in Chapter 4, we find several wide DWDs that show the opposite effect; the hotter (and hence younger) WD is the more massive of the pair. These systems could be the result of this triple star evolutionary channel in which the inner binary merged. Since the evolution of the blue straggler is essentially delayed, this system would appear as a wide DWD, but the cooling ages and masses would be discrepant. Most of these systems have large uncertainties in their spectroscopic solutions, so this discrepancy may be due simply to noise in the spectral fits. However, one system, HS 2220+2146, has

high-resolution VLT spectra with a high signal-noise ratio.⁷ In Chapter 5 we describe in detail how HS 2220+2146 could have formed through this evolutionary channel.

If this evolutionary formation scenario is correct, HS 2220+2146 is important for two reasons. First, for the most part, blue stragglers are found in dense stellar environments, where their formation is likely due to significant mass transfer. For instance, in the open cluster NGC 188, a large fraction are found in stellar binaries (Mathieu & Geller 2009). Gosnell et al. (2014) identified three specific blue stragglers with young WD companions. The widest orbital period binary, WOCS 4540, has a $P_{\text{orb}} = 3030 \pm 70$ days. These authors argue that although the binary is difficult to create via standard Roche lobe overflow, it can be formed through accretion from the stellar wind of a binary. With its extremely large orbital separation, HS 2220+2146 would be the first blue straggler binary shown to have been formed through a stellar merger.

Second, since the progenitor of this system began as a hierarchical triple system, it may have gone through secular evolution due to the eccentric Kozai-Lidov (EKL) mechanism (Kozai 1962; Lidov 1962). This mechanism trades angular momentum between the inner and outer orbits, resulting in large oscillations in the inner binary's eccentricity and mutual inclination of the two orbital planes. Perets & Fabrycky (2009) first suggested that the EKL mechanism combined with tidal dissipation could cause the inner binary to merge, forming a blue straggler in a binary. Naoz & Fabrycky (2014) expanded the EKL equations to include the octopolar term, and these authors ran a suite of simulations finding the distribution of blue straggler binary orbital periods resulting from the merger of an inner

⁷Recently, the more massive WD in the DWD SDSS J1257+5428 (Badenes et al. 2009; Marsh et al. 2011) was also shown to have a younger age than its companion (Bours et al. 2015). Since this system is a close DWD, it may have formed from binary evolution in which mass transfer affected the WDs' cooling ages.

binary in a hierarchical triple. The evolutionary product of these simulations would be a wide DWD. HS 2220+2146 could be evidence for the importance of the EKL mechanism for higher order stellar systems. We discuss the implications of our evolutionary formation scenario for HS 2220+2146 in Chapter 5.

1.7 Dissertation Structure

The work presented in this manuscript builds toward the goal of constraining the IFMR using wide DWDs. The outline is as follows.

In Chapter 2, we discuss our project modeling the companions to LMWDs. Our Bayesian statistical model argues for an enhanced mass distribution compared with the field, indicating a degree of mass accretion in the system's evolutionary past.

In Chapter 3 we address the relative paucity of wide DWDs in the literature. We collect the wide DWDs already published, then search SDSS DR7 for new wide DWDs.

Bolstered by the success of this study, we expanded our search in Chapter 4. We analyzed the expanded SDSS DR9, searching for wide DWDs using two separate methods. The yield from this study was substantial: we more than doubled the number of known wide DWDs. We further engaged in a spectroscopic follow-up campaign to study these systems, searching for those systems which would best constrain the IFMR. We then develop our method to constrain the IFMR. This method is based on the original assumptions from Greenstein et al. (1983) and Finley & Koester (1997). However, our updated model is very different; we employ a Bayesian hierarchical framework to simultaneously use all wide DWDs to constrain the IFMR. We further compare our results with previous

constraints, both theoretical and observed.

Throughout our analysis, we found several interesting systems, one of which we discuss in detail in Chapter 5: the strange system HS 2220+2146, which is potentially the first candidate post-blue straggler binary system.

In Chapter 6, we conclude, placing our results in the context of the study of WDs in binaries and providing several avenues for future progress.

(This page left intentionally blank.)

Chapter 2

ELM WDs

2.1 Introduction

Recently, the ELM WD Survey has identified 61 extremely LMWDs ($M \lesssim 0.3 M_{\odot}$) in the Sloan Digital Sky Survey (SDSS; York et al. 2000) and elsewhere (Brown et al. 2010; Kilic et al. 2011; Brown et al. 2012; Kilic et al. 2012; Brown et al. 2013). We refer to the 55 WDs found by these authors that have a measured radial velocity (RV) and orbital period (T) as the ELM sample.

These RV and T measurements indicate that the LMWDs companions are most likely WDs. However, since the inclination angle i is unknown, LMWDs could have neutron star (NS) companions. Indeed, LMWDs are known companions to millisecond pulsars, although these WDs are generally too faint for spectroscopy (van Kerkwijk et al. 1996;

⁰This section is a reformatted version of an article by the same name by Jeff J. Andrews, Adrian M. Price-Whelan, & Marcel A. Agüeros, that can be found in the *Astrophysical Journal Letters*, Volume 797, Issue 2, p. 32 (2014). The abstract has been removed, and slight modifications have been made (such as in acronyms) to ensure consistency throughout this dissertation. Portions of this paper's introduction appear in the introduction to this dissertation.

Callanan et al. 1998; Bassa et al. 2006; Antoniadis et al. 2012). Finding even one NS companion to a spectroscopically characterized LMWD would be very valuable, since this system could constrain the NS mass. To date, unfortunately, radio and X-ray searches for NS companions to LMWDs have been unsuccessful (van Leeuwen et al. 2007; Agüeros et al. 2009b,a; Kilic et al. 2013).

For each LMWD in the ELM sample, spectroscopy provides T , the primary WD mass M_1 , and the projected orbital velocity $K = v \sin i$. Assuming circular orbits, we can write:

$$\frac{(M_2 \sin i)^3}{(M_1 + M_2)^2} = \frac{T}{2\pi G} K^3, \quad (2.1)$$

where the right side is the mass function m_f . The companion mass, M_2 , is minimized for an edge-on orbit ($i = 90^\circ$). Because of this dependence on i , the nature of the companion cannot usually be determined based on m_f alone. Figure 2.1 shows that the population of LMWDs with pulsar companions occupies the same region in $M_1 - T$ space as those with WD companions. Therefore, barring rare circumstances such as eclipsing systems, individual LMWDs with NS companions cannot be identified from optical observations alone.

The ELM sample is now large enough that the M_2 distribution and NS companion fraction can be constrained statistically. We have developed a probabilistic model to infer parameters of an assumed form for the M_2 distribution. Our method is similar to that employed by Özel et al. (2012) and Kiziltan et al. (2013) to describe the mass distribution of NSs in binaries using post-Keplerian parameters. We focus on the following questions: Can the companion population be modeled using a simple description of M_2 ? How

does the M_2 distribution compare to predictions from population synthesis simulations? What is the rate of LMWD-NS binaries implied by our model? What are the resulting distributions of NS probabilities for individual systems in the ELM sample?

To answer these questions, we build the mathematical framework (Section 2), then test our resulting model (Section 3). We apply our model to the ELM sample (Section 4) before concluding (Section 5).

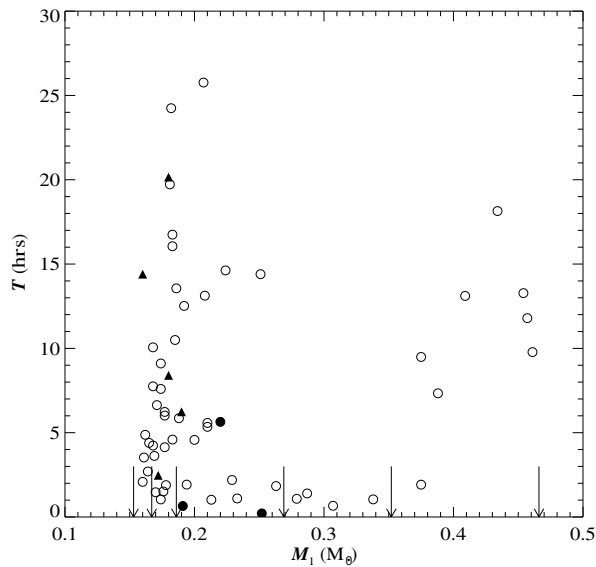


Figure 2.1 The $M_1 - T$ distribution of the ELM sample (circles) and the known WD-NS binaries (triangles). The three eclipsing systems in the ELM sample with known M_2 are shown as filled circles, and the masses of the ELM WDs without detected RV variations are shown by the arrows. From M_1 and T alone, the two populations are indistinguishable.

2.2 Building our model

We construct a statistical model to constrain a parametric model for the distribution of LMWD companion masses, $p(M_2 | \boldsymbol{\theta})$.¹ For each system, we assume we have K , T , and M_1 , and therefore know m_f . We wish to derive posterior constraints on the model parameters, $\boldsymbol{\theta}$, which describe the distribution of companion masses, $p(M_2 | \boldsymbol{\theta})$, given the set of observed mass functions, \mathbf{m}_f , by deconvolving the m_f distribution from the unobserved inclinations. Using Bayes' rule,

$$p(\boldsymbol{\theta} | \mathbf{m}_f) = \frac{1}{\mathcal{Z}} p(\mathbf{m}_f | \boldsymbol{\theta}) p(\boldsymbol{\theta}), \quad (2.2)$$

where $p(\mathbf{m}_f | \boldsymbol{\theta})$ is the likelihood, $p(\boldsymbol{\theta})$ is the prior on parameters $\boldsymbol{\theta}$, and the evidence integral, \mathcal{Z} , is a constant that depends only on the data. The likelihood, $p(\mathbf{m}_f | \boldsymbol{\theta})$, can be split into a product over the likelihoods of individual systems:

$$p(\mathbf{m}_f | \boldsymbol{\theta}) = \prod_j p(m_f | \boldsymbol{\theta}), \quad (2.3)$$

where the product is over each of the j systems. This marginal likelihood involves integrals over the unobserved quantities i and M_2 ,

$$p(m_f | \boldsymbol{\theta}) = \int_0^\infty dM_2 \int_0^{\pi/2} di p(m_f | M_1, M_2, i) p(M_2 | \boldsymbol{\theta}) p(i). \quad (2.4)$$

¹We represent vectors or sets of parameters or quantities by bold symbols.

We neglect observational uncertainties in m_f and M_1 ,² and assume the inclination angles are isotropically distributed:

$$p(m_f | M_1, M_2, i) = \delta [m_f - f(M_1, M_2, i)], \quad (2.5)$$

where

$$f(M_1, M_2, i) = \frac{(M_2 \sin i)^3}{(M_1 + M_2)^2} \quad (2.6)$$

and

$$p(i) = \sin i. \quad (2.7)$$

For now, we do not specify a parametric form for the companion mass distribution, $p(M_2 | \theta)$. With the above assumptions, the marginal likelihood integral is:

$$p(m_f | \theta) = \int_0^\infty dM_2 p(M_2 | \theta) \int_0^{\pi/2} di \sin i \delta [g(M_1, M_2, i)], \quad (2.8)$$

where

$$g(M_1, M_2, i) = m_f - \frac{M_2^3}{(M_1 + M_2)^2} \sin^3 i. \quad (2.9)$$

The inner integral (over i) has the form:

$$\int dx F(x) \delta [G(x)] = \sum_j \frac{F(x_j^*)}{|G'(x_j^*)|} \quad (2.10)$$

²The fractional uncertainties in these quantities are small, $\sigma_x/x \sim 0.05 - 0.1$ (Gianninas et al. 2014).

where the sum is over the roots, x_j^* , of the function $G(x)$. The root, i^* , and derivative of the argument of the delta function in Equation 2.8 are:

$$\sin i^* = \frac{[m_f(M_1 + M_2)^2]^{1/3}}{M_2}, \quad (2.11)$$

$$\left. \frac{\partial g}{\partial i} \right|_{i^*} = \frac{3M_2^3}{(M_1 + M_2)^2} \sin^2 i^* \sqrt{1 - \sin^2 i^*}. \quad (2.12)$$

We may rewrite the marginal likelihood as:

$$p(m_f | \theta) = \int_0^\infty dM_2 p(M_2 | \theta) \sin i^* \left(\left. \frac{\partial g}{\partial i} \right|_{i^*} \right)^{-1} \quad (2.13)$$

$$= \int_{M_{2,\min}}^\infty dM_2 p(M_2 | \theta) h(M_2, m_f, M_1). \quad (2.14)$$

The bottom bound in the integral in Equation 2.14 is set by the minimum companion mass for which the integrand is real, $M_{2,\min}$, determined by setting $i = 90^\circ$ in Equation 2.1 and solving for M_2 , and

$$h(M_2, m_f, M_1) = \frac{(M_1 + M_2)^{4/3}}{3 m_f^{1/3} M_2 \sqrt{M_2^2 - [m_f(M_1 + M_2)^2]^{2/3}}}. \quad (2.15)$$

2.2.1 Our Model

We must now choose a functional form for the companion mass distribution, $p(M_2 | \theta)$. We use a two-component Gaussian mixture model. We truncate the distributions using physically motivated bounds: the WD component is restricted to $M_2 \in [0.2, 1.44] M_\odot$ and

the NS component is restricted to $M_2 \in [1.3, 2.0] M_\odot$. We then have:

$$p(M_2 | \boldsymbol{\theta}) = [(1 - f_{\text{NS}}) p_{\text{WD}} + f_{\text{NS}} p_{\text{NS}}], \quad (2.16)$$

where f_{NS} is the NS fraction and

$$p_{\text{WD}} = \mathcal{N}(M_2 | \mu_{\text{WD}}, \sigma_{\text{WD}}^2); 0.2 < \frac{M_2}{M_\odot} < 1.44, \quad (2.17)$$

$$p_{\text{NS}} = \mathcal{N}(M_2 | \mu_{\text{NS}}, \sigma_{\text{NS}}^2); 1.3 < \frac{M_2}{M_\odot} < 2. \quad (2.18)$$

\mathcal{N} is the (truncated, but properly normalized) normal distribution with mean μ and variance σ^2 ; the distributions are limited to the ranges specified. To reduce the number of parameters in our model we fix μ_{NS} and σ_{NS} to:

$$\mu_{\text{NS}} = 1.4 M_\odot, \quad (2.19)$$

$$\sigma_{\text{NS}} = 0.05 M_\odot, \quad (2.20)$$

as some NSs in binaries may be somewhat more massive than the canonical NS mass of $1.35 M_\odot$ (Kiziltan et al. 2013; Smedley et al. 2014).

The probability of any particular WD having a NS companion, P_{NS} , can be computed for a given set of parameters for the M_2 distribution:

$$P_{\text{NS}} = \frac{\int_{M_{2,\text{min}}}^{\infty} dM_2 f_{\text{NS}} p_{\text{NS}} h(M_2, m_f, M_1)}{p(m_f | \boldsymbol{\theta})}. \quad (2.21)$$

Table 2.1 Model Results

		μ_{WD} [M_{\odot}]	σ_{WD} [M_{\odot}]	f_{NS}
Priors		$\mathcal{U}(0.2, 1)$	$\propto \sigma^{-1}$ ($0.02 < \sigma/M_{\odot} < 2.0$)	$\mathcal{U}(0, 1)$
Test Cases				
Test 1	True	0.7	0.2	0
	MAP	0.72	0.20	0.0
Test 2	True	0.7	0.2	0.10
	MAP	0.74	0.19	0.11
Test 3	True	0.10
	MAP	0.63	0.52	0.14
PCEB	True	0
	MAP	0.58	0.16	0.0
ELM Sample				
MAP		0.74	0.24	0.0

Note. – Parameter information for the form of the M_2 distribution used in the tests described in Section 2.3. \mathcal{U} is the uniform distribution. We additionally fix the NS mass distribution: $\mu_{\text{NS}} = 1.4 M_{\odot}$ and $\sigma_{\text{NS}} = 0.05 M_{\odot}$.

Our companion mass model parameters are then $\theta = (\mu_{\text{WD}}, \sigma_{\text{WD}}, f_{\text{NS}})$. For μ_{WD} , we use a uniform prior from $0.2 - 1.0 M_{\odot}$; for σ_{WD} , we use a logarithmic (scale-invariant) prior over the range $0.02 - 2.0 M_{\odot}$. Finally, we use a uniform prior over the dimensionless f_{NS} from $0 - 1$. The model parameters are summarized in Table 2.1.

We use a Markov Chain Monte Carlo algorithm (Goodman & Weare 2010) to draw samples from the posterior distribution, $p(\mu_{\text{WD}}, \sigma_{\text{WD}}, f_{\text{NS}} | \mathbf{m}_f, \mathbf{M}_1)$.³ The algorithm uses an ensemble of individual “walkers” to naturally adapt to the geometry of the parameter-space being explored. We run the walkers for a burn-in period of 500 steps starting from

³Our model uses emcee, implemented in Python (Foreman-Mackey et al. 2013a).

randomly drawn initial conditions (sampled from the priors in Table 2.1). We then re-initialize the walkers from their positions at the end of this run and run again for 1000 steps. We remove the burn-in samples to eliminate any effects due to our choice of initial conditions.

2.3 Testing Our Model

We test the performance of this Gaussian mixture model on four separate data sets: three mock data sets and a sample of SDSS post-common-envelope binaries (PCEBs; Nebot Gómez-Morán et al. 2011). Each of the 100 systems in our three mock data sets is generated by computing a m_f from a random M_1 (drawn from a uniform distribution, $\mathcal{U}(0.2, 0.4) M_\odot$), M_2 (from the distributions described below), and i (from an isotropic distribution). We apply the same Gaussian mixture model to all four tests to infer the parameters of the WD mixture component and f_{NS} .

2.3.1 Test 1: Single Gaussian (WD)

We first generate companion masses by drawing from a single, truncated Gaussian with the parameters given in Table 2.1. This mock sample contains no NSs. In the top row of Figure 2.2, the left-most panel shows that our model finds a maximum a posteriori (MAP) M_2 distribution (black line) that qualitatively matches the input distribution (gray histogram). The second and third panels show samples from the posterior distributions and contours containing 68% and 95% of the samples for our three model parameters. The

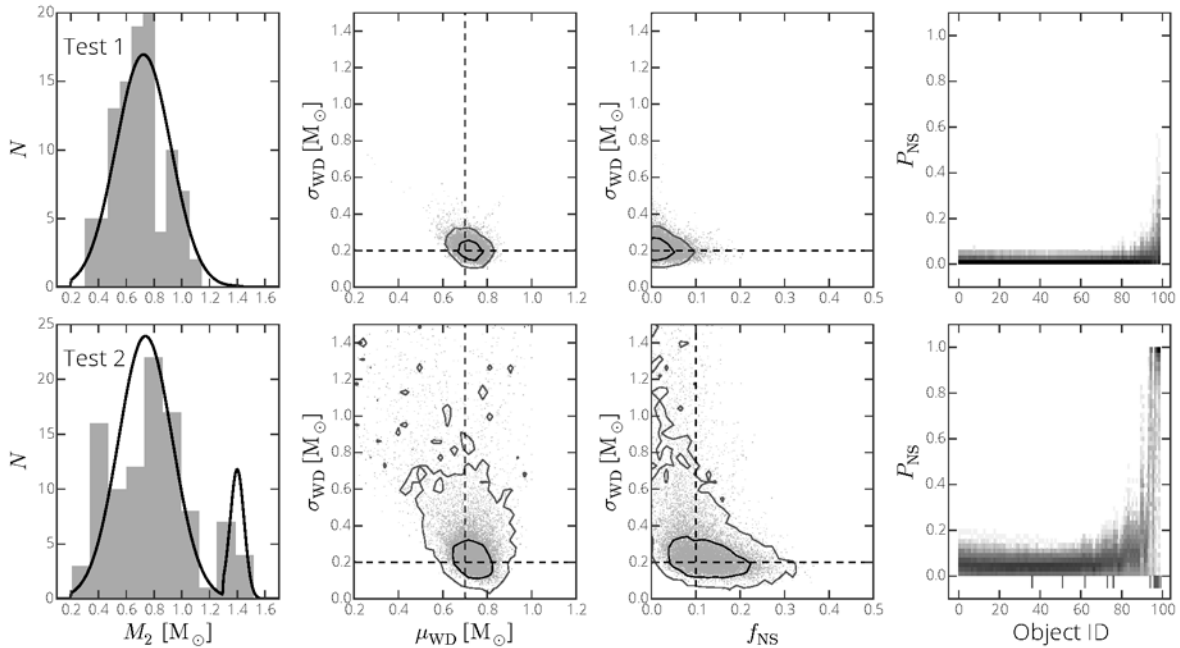


Figure 2.2 Results from testing the first two mock data sets described in Section 2.3. The left-most panels show the companion masses (gray histogram) randomly drawn from each of our test distributions and our MAP models (black line). Panels in the second and third columns show samples from the posterior distributions of μ_{WD} and σ_{WD} and f_{NS} . Contours designate the 68% and 95% confidence levels. Dashed lines in these panels show the true values from which the sample systems were drawn. The fourth panel shows individual mock LMWD systems (ordered by increasing m_f) and their corresponding P_{NS} distribution. Tick marks along the bottom indicate inputted LMWD-NS systems.

input values (dashed lines) lie cleanly within the inner contour in both panels, although f_{NS} has a tail up to $\approx 10\%$.

Equation 2.21 gives the probability of an individual system hosting a NS. Using posterior samples, we can determine the distribution of P_{NS} for each system. The right-most panel in Figure 2.2 includes all the individual systems, ordered by m_f , and shows the distributions of P_{NS} for each. For most systems, there is negligible probability above $P_{\text{NS}} \sim 5\%$.

2.3.2 Test 2: Two Gaussians (WD + NS)

We use the same Gaussian distribution to generate companion masses for the WDs but add a NS component with $f_{\text{NS}} = 10\%$. The bottom row of Figure 2.2 shows that our model again recovers the input values for μ_{WD} and σ_{WD} . Importantly, the third panel shows that our model also recovers f_{NS} , although the posterior shows a substantial tail toward higher f_{NS} . Tick marks in the right-most panel of Figure 2.2 indicate “true” NSs in our mock data. Our model correctly assigns high P_{NS} to roughly half of these. However, many systems with NS companions have inclinations too low to be statistically differentiated from those with WD companions.

2.3.3 Test 3: Uniform (WD) + Gaussian (NS)

We generate companion masses for the WDs by sampling from a uniform distribution over $[0.2, 1.2] M_{\odot}$, again with $f_{\text{NS}} = 10\%$. The top row of Figure 2.3 shows the results. The posterior distribution in the second panel indicates that μ_{WD} and σ_{WD} are not well constrained. The preference for larger σ_{WD} is expected, as the model flattens the Gaussian model distribution to match it with the input uniform distribution. Interestingly, the third panel shows that despite having a non-Gaussian input distribution for M_2 , and a poorly constrained σ_{WD} , our model still recovers f_{NS} approximately as accurately as in Test 2. Furthermore, the fourth panel of Figure 2.3 demonstrates that our model effectively identifies which LMWDs host NS companions.

2.3.4 Test 4: PCEBs

PCEBs are composed of WDs in close orbits with Main Sequence companions. The Nebot Gómez-Morán et al. (2011) sample of 54 SDSS PCEBs, which have precisely determined K , T , and masses for the Main Sequence companions, are an ideal test sample for our model. Our model uses these parameters to try and recover the PCEBs WD mass distribution, which we can then compare to the spectroscopically determined WD masses. Our MAP distribution (black line) is shown in the left-most panel in the bottom row of Figure 2.3. Our model qualitatively recovers the true M_{WD} distribution (gray histogram). The third panel shows that the posterior f_{NS} distribution is very low, as expected since there are no NS companions in the PCEB sample. This is further illustrated in the right-most panel, where every PCEB in the sample has low P_{NS} values.

2.4 Applying our model

2.4.1 The ELM Sample

The ELM WD Survey is based on the Hypervelocity Star Survey (Brown et al. 2006), and includes previously identified SDSS LMWDs (Eisenstein et al. 2006a; Liebert et al. 2004). Objects are chosen for spectroscopic follow-up based on their ugr colors, and this choice is independent of the mass and nature of any putative companions. Therefore, at least with regard to i and M_2 , the population is unbiased.

The ELM WD sample includes 55 systems with RV variations fit to orbital solutions, which provide precise measurements of T and K . WD masses in these systems are derived

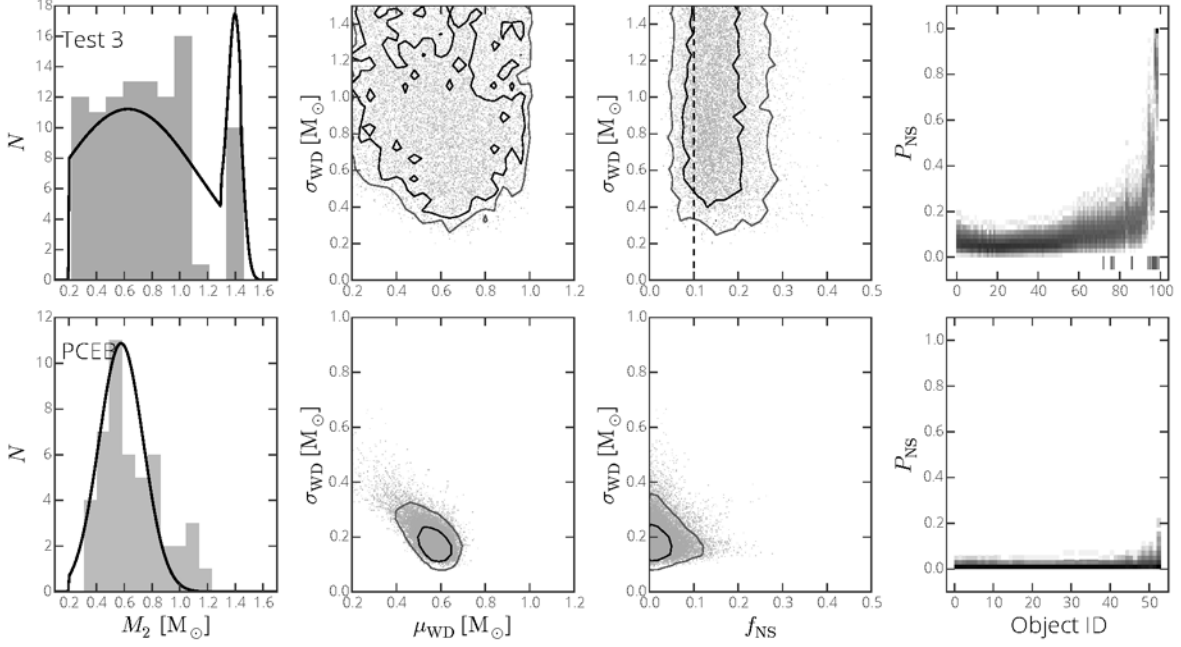


Figure 2.3 The results of our model when applied to our third mock data set and the SDSS PCEB sample. The panels are same as those in Figure 2.2.

from fits to spectroscopic templates, which are generally precise to $\approx 10\%$ (Gianninas et al. 2014). The masses of cool LMWDs may suffer somewhat from inaccuracies in the one-dimensional WD atmospheric models (Tremblay et al. 2013). However, since this should only affect the coolest WDs in the ELM sample, we expect any impact on our results to be minor.

Three systems are eclipsing binaries, with known companion masses: NLTT 11748 ($M_2 = 0.72 M_\odot$; Kaplan et al. 2014), SDSS J065133.3+284423.3 ($M_2 = 0.50 M_\odot$; Brown et al. 2011b), and SDSS J075141.2–014120.9 ($M_2 = 0.97 M_\odot$; Kilic et al. 2014). For these systems, the likelihood reduces to:

$$p(m_f | \theta) = (1 - f_{\text{NS}}) \mathcal{N}(M_2^* | \mu_{\text{WD}}, \sigma_{\text{WD}}^2), \quad (2.22)$$

where M_2^* is the mass of the WD companion.

The other six ELM systems show no evidence of orbital motion, with RV upper limits of $\approx 20\text{-}50 \text{ km s}^{-1}$. Some of these systems may be in low i binaries with RVs below the detection limit, or may have $T \approx 24 \text{ hr}$, which is difficult to measure (Brown et al. 2013). These LMWDs could also have companions at systematically longer T , resulting in orbital velocities below the detection limit. We do not include these systems in our analysis.

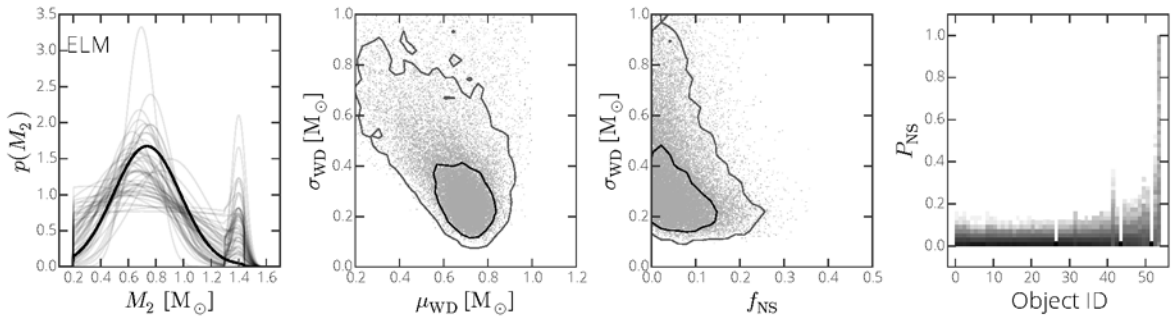


Figure 2.4 Results from applying our model to the ELM WDs. The panels are the same as in Figures 2.2 and 2.3. The left-most panel shows both the MAP M_2 distribution (solid black) and random samples from the posterior (gray lines). The three systems in the right-most panel with all $P_{\text{NS}} = 0\%$ are the eclipsing systems with measured M_2 .

2.4.2 Results and Discussion

The results from applying our model to the ELM sample are shown in Figure 2.4. The MAP model gives $\mu_{\text{WD}} = 0.74 M_{\odot}$, $\sigma_{\text{WD}} = 0.24 M_{\odot}$, and $f_{\text{NS}} = 0\%$. The marginal posterior over μ_{WD} and σ_{WD} has a tail toward larger σ_{WD} , which could indicate that the true WD distribution may not be exactly Gaussian.

It is interesting that the best-fit Gaussian for the companions to the ELM WDs is similar to that of the population of single hydrogen-atmosphere WDs in SDSS, with a mean

of $0.6 M_{\odot}$ (Kleinman et al. 2013). Our MAP variance is significantly larger: $\sigma \approx 0.26 M_{\odot}$, compared to $\sigma \approx 0.1 M_{\odot}$, possibly due to past mass transfer phases increasing the masses of the unseen primary WDs.

The low combined mass in these systems indicates that, although several of them will merge within a Hubble time (Brown et al. 2013), the majority of the ELM systems are unlikely to be type Ia SN progenitors. However, we cannot rule out the possibility that some individual LMWD binaries may be massive enough to produce type Ia SNe (Justham et al. 2009).

Our posterior distributions further suggest that the companions to LMWDs have predominantly CO cores. This is in contrast to population synthesis models, which suggest that LMWDs should predominantly have He-core WD companions (Toonen et al. 2012). With a larger sample, a more sophisticated LMWD companion model could place quantitative constraints on population synthesis predictions.

The third panel in Figure 2.4 shows a f_{NS} strongly peaked toward 0%. However, there is a significant tail toward higher NS probabilities. Our model indicates $f_{\text{NS}} < 16\%$ at the 68% confidence level, in agreement with independent constraints from van Leeuwen et al. (2007, $f_{\text{NS}} < 18 \pm 5\%$) and Agüeros et al. (2009b, $f_{\text{NS}} < 10_{-2}^{+4} \%$), both based on radio non-detections of LMWD companions.

The right-most panel in Figure 2.4 indicates there are two LMWDs with substantial P_{NS} : SDSS J081133.6+022556.8 and J174140.5+652638.7. However, the X-ray non-detection of SDSS J174140.5+652638.7 suggests its companion is unlikely to be a NS (Kilic et al. 2014). Searches for radio and X-ray emission from SDSS J081133.6+022556.8 are on-going. We

note that the P_{NS} distributions in each of our samples show a trend such that systems with higher m_f have higher P_{NS} values. These high m_f systems are therefore ideal targets to search for NS companions to LMWDs.

2.5 Conclusions

We have developed a statistical model to infer the companion mass distribution for a sample of single-line, spectroscopic binaries. This model can be applied to any such sample with measured M_1 and m_f . When tested on three separate mock data sets with unseen WD and NS companions to LMWDs, our model recovers the input parameters. Even when the companion mass distribution is not drawn from a Gaussian distribution, our model still infers the input NS fraction to within a few percent. We further apply our model to the SDSS PCEBs (Nebot Gómez-Morán et al. 2011), and our model qualitatively recovers the independent, spectroscopically measured M_{WD} distribution.

We applied our model to the set of LMWDs from the ELM WD survey. The resulting posterior distribution is qualitatively similar to our two-component Gaussian test case, suggesting that the companion mass distribution to the LMWDs in the ELM sample is well-described by our model. Our model returns a MAP $\mu_{\text{WD}} = 0.74 \pm 0.24 M_{\odot}$, suggesting that a majority of ELM WDs have CO-core WD companions. This is in contrast to predictions from population synthesis models, which find that the dominant companion population should be He-core WDs (e.g., Toonen et al. 2012). Our model further indicates that the fraction of ELM WDs with NS companions is consistent with 0%, but could be as high as $\approx 16\%$ (within $1-\sigma$). Finally, our model identifies the LMWD SDSS J081133.6+022556.8 as

having the highest median probability of hosting a NS companion.

To determine the probability of any particular LMWD hosting a NS, we make our model posteriors publicly available on [figshare](#).⁴ We further provide a Python script that calculates P_{NS} and the mass distribution for a WD companion for any LMWD with a measured M_1 and m_f . This script can be applied to newly discovered LMWDs as well as those already in the ELM sample.

There are several ways in which our model can be expanded. By modeling photometric variability, Hermes et al. (2014) recently constrained the inclination of 20 LMWDs in the ELM sample; we could include these constraints. Furthermore, our model can place tighter constraints on f_{NS} by factoring in radio and X-ray non-detections. We plan to develop our method to quantitatively compare our model to the results of population synthesis codes, potentially constraining the formation of LMWDs.

2.6 Acknowledgments

The authors wish to acknowledge David Hogg and DJ D’Orazio for useful discussions, and the organizers of the *AstroData Hack Week* (2014). APW is supported by a National Science Foundation Graduate Research Fellowship under Grant No. 11-44155. This research made use of Astropy, a community-developed core Python package for Astronomy (Astropy Collaboration et al. 2013).

⁴<http://dx.doi.org/10.6084/m9.figshare.1206621>

(This page left intentionally blank.)

Chapter 3

Searching for Wide Double White Dwarf Binaries in SDSS DR7

3.1 Introduction

Only 35 wide DWDs have been previously identified in the literature. Yet, since most of these were discovered over 20 years ago from even older surveys, it is clear that these 35 only represent the tip of a much larger population. As pioneered by Luyten and Greenstein, systematically identifying wide DWDs requires multi band photometric and proper motion surveys. In the past decade, astronomical surveys and large data sets have, in particular, benefited from the boon of modern computing. In particular, the Sloan Digital Sky Survey (SDSS) has revolutionized our understanding of the stellar population

⁰This section is a reformatted version of an article by the same name by Jeff J. Andrews, Marcel A. Agüeros, Krzysztof Belczynski, Saurav Dhital, S. J. Kleinman, & Andrew A. West that can be found in the *Astrophysical Journal*, Volume 757, Issue 2, p. 170 (2012). The abstract has been removed, and slight modifications have been made (such as in acronyms) to ensure consistency throughout this dissertation. Portions of this paper's introduction appear in the introduction to this dissertation.

of the Galaxy.

The photometric survey covered a large area to unprecedented depth ($>10^4$ deg² and ~ 22 mag; Abazajian et al. 2009), and matches between SDSS and USNO-B have been used to generate a proper motion catalog (Munn et al. 2004) that is integrated into the SDSS database. Indeed, Dhital et al. (2010) used SDSS to uncover wide companions to low-mass Main Sequence stars based on common proper motions: these authors identified over 1300 CPMBs, of which 21 include one WD.

We adapt the method developed by Dhital et al. (2010) to search for widely separated WD companions to the set of spectroscopically confirmed DA WDs included in the Kleinman et al. (2013) catalog of spectroscopically confirmed WD binaries. In Section 3.2 we discuss the population synthesis predictions for the orbital distribution of WD binaries that motivated this search. We present in Section 3.3 our method for identifying candidate CPMBs and in Section 3.4 the properties of our newly discovered DWDs; we also compare these properties to those of the previously known pairs. We provide some concluding thoughts for this chapter in Section 3.5.

3.2 Motivation

Whether a DWD is observed today as a tight or a wide binary depends primarily on the orbital separation of the binary at birth. Because WD progenitors go through mass-losing giant phases, wide DWD orbits may expand up to a factor of five due to conservation of angular momentum (Greenstein 1986b). If, however, the WD progenitors overflow their Roche lobes while in a giant phase, they will likely enter unstable mass transfer, causing

a rapid, order-of-magnitude shrinking of the orbit (e.g., Iben & Livio 1993). We therefore expect to observe a bimodal distribution of orbital separations, with a population of wide DWDs that avoided any mass transfer phases and one of tight DWDs that underwent unstable mass transfer. We use population synthesis to characterize this distribution in detail.

3.2.1 Population Synthesis of DWD Systems

Population synthesis is commonly used to analyze the formation and evolution of DWDs. For example, Nelemans et al. (2001b) and Nelemans & Tout (2005) have used it to examine the physics of mass transfer, Ruiter et al. (2011) and Meng et al. (2011) to estimate SN Ia rates due to DWD mergers, and Ruiter et al. (2010) and Yu & Jeffery (2010) to predict the gravitational wave signal from inspiraling DWDs — all phenomena related to tight DWDs. Wide DWDs, however, have largely been ignored in these studies.

Using the binary population synthesis code *StarTrack* (Belczynski et al. 2002, 2008), we evolve a sample of 10^6 zero age Main Sequence (ZAMS) binaries and determine the orbital separation distribution of the $\sim 5\%$ that become DWDs. We summarize our initial conditions in Table 3.1 and describe them briefly below.

We use the standard Ambartsumian eccentricity distribution (Ambartsumian 1937; Duquennoy & Mayor 1991). The initial mass of the more massive primary star is drawn from a Kroupa initial mass function (IMF; Kroupa et al. 1993), and the initial mass of the companion star is a random fraction of the primary mass (Kobulnicky & Fryer 2007). Because of the weak dependence of the orbital separation on the component mass and

Table 3.1. Initial Conditions for Population Synthesis

Parameter	Distribution	Range
Eccentricity	$\frac{dn}{de} \propto 2e$	$0 < e < 1$
Primary IMF	$\frac{dn}{dM} \propto \begin{cases} M^{-2.2} \\ M^{-2.7} \end{cases}$	$0.5 < \frac{M}{M_{\odot}} < 1$ $1 < \frac{M}{M_{\odot}} < 10$
Mass ratio	$\frac{dn}{dq} \propto 1$	$0 < q < 1$
Orbital separation	$\frac{dn}{da} \propto a^{-1}$	$R_L < a < 10^5 \text{ AU}$

Note. — R_L is the radius of the Roche lobe.

orbital eccentricity, we expect that other (reasonable) distributions for these variables would not significantly alter the orbital separation distribution.

The initial orbital separations range from the two stars starting just outside of contact to being 10^5 AU apart. The maximum separation of binaries at birth is not well constrained. However, $\sim 15\%$ of all G dwarfs are found in binary systems with separations $\gtrsim 10^4$ AU (Duquennoy & Mayor 1991), the mean radii of pre-stellar cores are $\sim 10^5$ AU (Clemens et al. 1991), and other studies have identified binaries with $a \sim 10^5$ AU (e.g., Dhital et al. 2010), so that this maximum initial separation is a reasonable estimate.

We choose a logarithmically flat distribution for a (Öpik 1924; Poveda et al. 2007). Observationally, the distribution of birth orbital separations may be very different (e.g., Duquennoy & Mayor 1991; Chanamé & Gould 2004; Lépine & Bongiorno 2007). However, when we test the broken power-law distribution of Lépine & Bongiorno (2007), we see no significant differences in the resulting present day orbital separation distribution of DWDs.

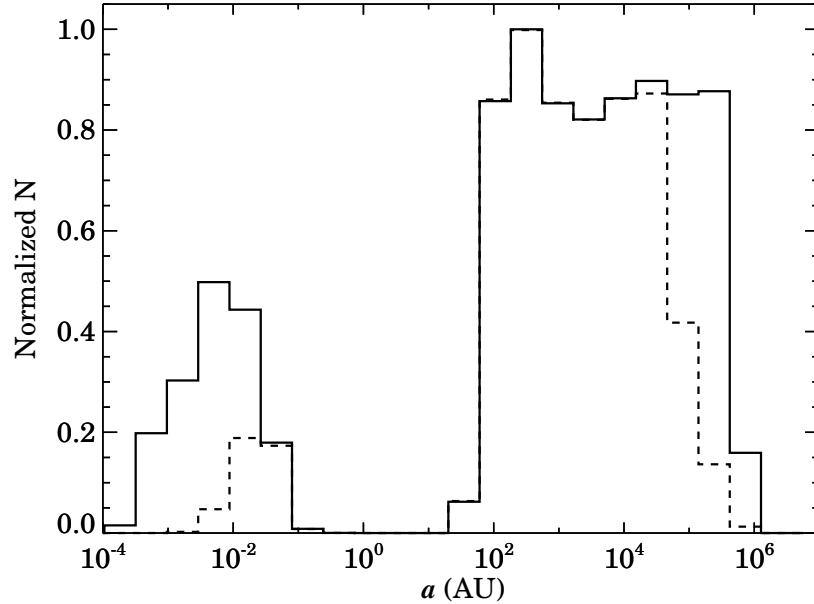


Figure 3.1 Normalized orbital separation distribution of binaries produced by our population synthesis code once they become DWDs (solid line) and after perturbing effects have been taken into account (dashed line). The compact systems are depleted due to mergers, while the widest systems are disrupted due to three-body interactions.

The solid line in Figure 3.1 is the orbital separation distribution immediately after the birth of the second WD. As expected, this distribution is bimodal, with the number of systems with $a \gtrsim 10^2$ AU dominating the overall population. Interestingly, about 10% of these wide pairs did experience mass transfer: the primary underwent stable Roche lobe overflow while on the asymptotic giant branch. In 90% of cases, by contrast, the two stars can be considered to have evolved independently.

While the number and distribution of tight systems in Figure 3.1 is strongly dependent upon e.g., the prescription used to describe common envelope evolution, the existence of a population of a population of DWDs widely separated at birth is a robust prediction of our code.

3.2.2 Evolution of the Synthesized DWD Orbits

DWD orbits are modified over time by gravitational wave radiation and weak interactions with other bodies in the Galaxy. We use the equations of Peters (1964) to model the first of these effects, which is most important for the tightest binaries in Figure 3.1. We model the second effect using the Fokker-Planck approximation, which determines the diffusion of energy into and out of the binary system. Using this approximation, Weinberg et al. (1987) found the characteristic lifetime t of a binary consisting of two $0.6 M_{\odot}$ WDs to be:

$$t \approx 2.9 \left(\frac{a}{10^5 \text{AU}} \right)^{-1} \text{Gyr.} \quad (3.1)$$

The lifetime of a canonical DWD with $a \sim 10^5$ AU is therefore a few Gyr.¹

We assign each ZAMS binary a birth time uniformly distributed over the lifetime of the Galactic disk (0-10 Gyr). The dashed line in Figure 3.1 shows the distribution of surviving binaries at the present day (10 Gyr), after gravitational radiation and Galactic interactions have caused some to merge and disrupted others. Even with our gross overestimate of the effect of Galactic perturbations, a large number of the wide DWDs survive and should be observable today.

3.2.3 Predicted Observed Angular Separation Distribution

To translate our synthesized population into an observable population, we assign each DWD an argument of pericenter, mean anomaly, and cosine of the inclination angle, all

¹This may be an overestimate of a wide binary's lifetime because it ignores the differential pull of the Galactic potential (Jiang & Tremaine 2010). Although this effect is important, applying these authors' semi-analytic method to our population synthesis output is beyond the scope of this work.

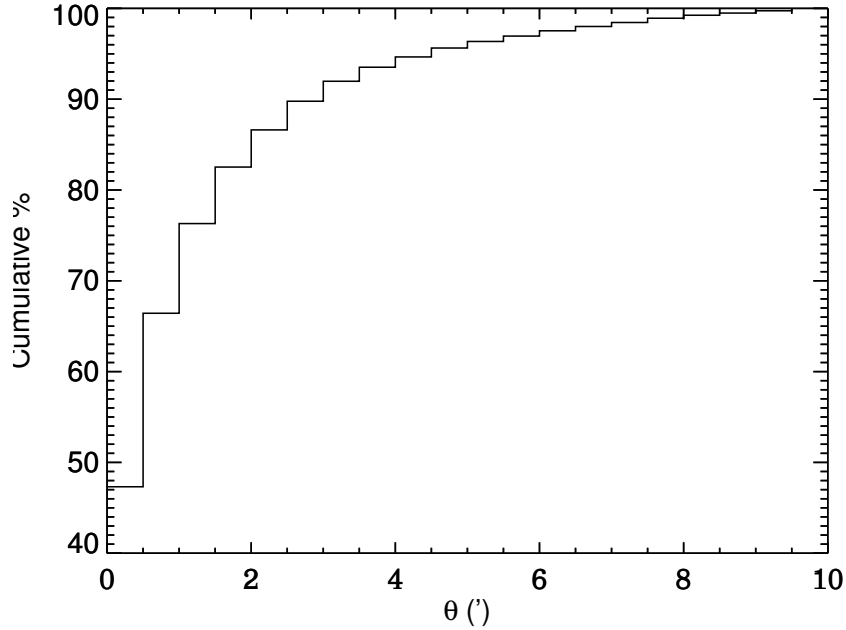


Figure 3.2 Expected cumulative percentage of DWD as a function of separation once projection effects are taken into account. The binaries are artificially placed at a distance of 250 pc. Close pairs dominate the distribution, but $\sim 15\%$ have $\theta \gtrsim 2'$.

randomly selected from flat distributions. These parameters, combined with the intrinsic orbital parameters of the binary (eccentricity, masses, and orbital separation) define the orbital positions of the two WDs. Using a fiducial distance of 250 pc, we then determine the projected angular separation (θ) of each DWD. Binaries with $\theta < 8''$ or $> 10'$ are eliminated because our method for identifying DWDs (described below) is not sensitive to these. The predicted observed θ distribution of our synthesized DWDs is shown in Figure 3.2. We find that the qualitative characteristics of this distribution are conserved for any reasonable assumption for the distance to the binaries. Although the DWD population is dominated by pairs with separations $< 1'$, a small fraction is expected to be observed at separations extending to $10'$.

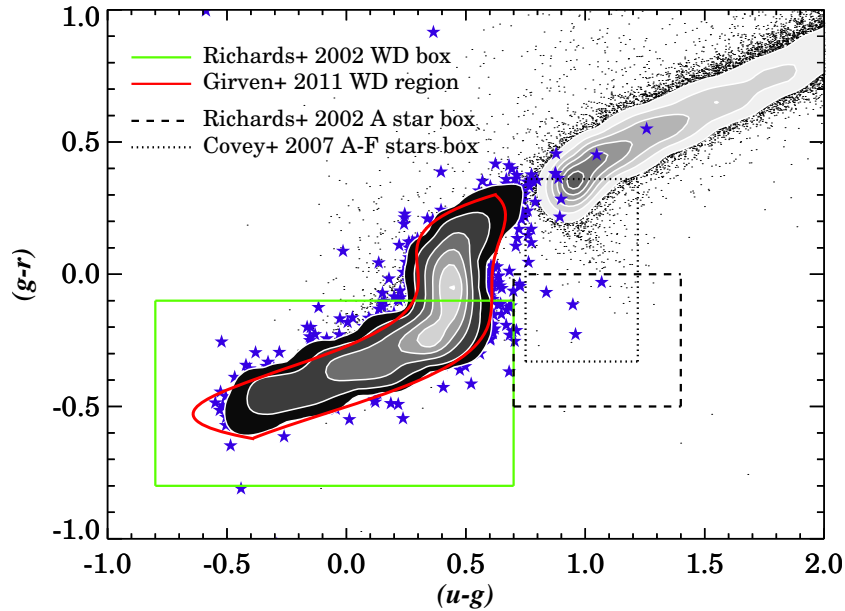


Figure 3.3 $(g - r)$ vs. $(u - g)$ for 8605 spectroscopically confirmed DAs with a unique entry in the new Kleinman et al. catalog and with $ugriz$ photometric errors ≤ 0.15 mag (stars and dark contours). The points and light-colored contours to the upper right indicate the colors of $>99,000$ randomly selected stars with $ugriz$ errors ≤ 0.1 mag, $ugriz \geq 15.5$ mag, and $g \leq 20$ mag (these stars also meet the same proper motion constraints that were applied to our primary WDs). These stars are included to highlight the small overlap between the WD locus and the Main Sequence. Overplotted are different regions used to photometrically select WDs and A stars. The region defined by Girven et al. (2011) traces the empirical DA locus extremely well and includes 96% of the 8605 DAs, a significantly larger fraction than returned by the standard Richards et al. (2002) color-cuts.

3.3 Identifying Wide DWDs in SDSS

3.3.1 Candidate Binary Selection Process

The SDSS data reduction pipeline matches objects to objects in the USNO-B catalog, which has a limiting magnitude of ~ 21 mag. Proper motions calculated during this matching are included in the propermotion table of the DR7 catalog.² We use the CasJobs database³ to

²Proper motions generated from this matching before DR7 contained a systematic error that has since been corrected (Munn et al. 2008).

³<http://cas.sdss.org/casjobs/>

obtain all the available proper motion data for the DA WDs in the Kleinman et al. catalog: 11,563 DAs (92%) have measured proper motions.

Following Munn et al. (2004), we eliminate any WD with a rms fit residual ≤ 350 mas in either right ascension (α) or declination (δ) and any WD with more than one possible USNO-B counterpart (i.e., $\text{match} \neq 1$). We also eliminate any WD with a total $\mu < 20$ mas/yr or with $\sigma_\mu > 10$ mas/yr in either coordinate. $\sim 56\%$ of the DAs in the Kleinman et al. catalog do not survive these cuts; most of these WDs have total proper motions below our threshold. We refer to the remaining ~ 5500 DAs as primaries in our CPMBs and to their candidate companions as secondaries.

Next, we query CasJobs for all objects offset by $< 10'$ from each of our primary WDs, yielding $\sim 4.1 \times 10^6$ objects.⁴ Applying the proper motion quality cuts described above pares our list of potential secondaries down to $\sim 2.2 \times 10^5$ objects. (Most of the eliminated objects lack proper motions only because they are too faint to be included in the USNO-B catalog.) We eliminate objects with poor photometry, i.e., with g -band errors > 0.1 mag or $uriz$ errors > 1.0 mag; this leaves $\sim 2.0 \times 10^5$ objects.

We then search for objects with a proper motion matching that of our primary WDs. Typical proper motion observational errors are ~ 4 mas/yr. In the most extreme case of a face-on orbit at the observational limit $\theta = 8''$ and at a distance of 50 pc, two WDs with typical $M = 0.6 M_\odot$ in a circular binary will have an orbital velocity of ~ 0.8 km/s. This translates to a differential $\mu \sim 3.4$ mas/yr, which is of the same order as our observational σ_μ . Since all our binaries are found at distances > 50 pc (see below) and have $\theta > 8''$, the

⁴We require that these objects be defined by SDSS as primary, meaning they met a number of quality criteria that are described in Stoughton et al. (2002).

orbital velocities of our binaries can be ignored.

We define a proper motion match in the same manner as Dhital et al. (2010):

$$\left(\frac{\Delta\mu_\alpha}{\sigma_{\Delta\mu_\alpha}}\right)^2 + \left(\frac{\Delta\mu_\delta}{\sigma_{\Delta\mu_\delta}}\right)^2 \leq 2, \quad (3.2)$$

where $\Delta\mu$ is the scalar proper motion difference in α and δ , and $\sigma_{\Delta\mu}$ is the error in the corresponding $\Delta\mu$, derived from the quadrature sum of the individual errors in μ . This greatly reduces the number of candidate secondaries, to only 7129.

Finally, to identify candidate WDs among these secondaries, we select objects within 0.5σ of the region in $(g-r)$ versus $(u-g)$ color-color space defined by Girven et al. (2011) as occupied by WDs. This region encompasses a larger area of the WD locus than do the standard Richards et al. (2002) color cuts. Furthermore, the Girven et al. (2011) region does not overlap with the $(g-r)$ versus $(u-g)$ boxes defined by Richards et al. (2002) and Covey et al. (2007) for Main Sequence A and early F stars, the most likely stellar contaminants (see Figure 3.3).⁵ 41 SDSS objects survive this final cut.

3.3.2 Distances (and Radial Velocities)

In addition to matching proper motions, bound binaries should have matching distances and (when available) radial velocities (RVs). For our candidate primaries, we use the spectroscopically derived T_{eff} and $\log g$ values from the Kleinman et al. catalog and linearly interpolate T_{eff} and quadratically interpolate $\log g$ in model evolutionary grids⁶

⁵The separation between these regions is cleanest in this combination of colors.

⁶<http://www.astro.umontreal.ca/~bergeron/CoolingModels/>

Table 3.2. Candidate Wide DWDs with SDSS Spectra for Both Components

Name	D_1 (pc)	D_2 (pc)	RV_1 (km/s)	RV_2 (km/s)
J0332–0049	143 ± 21	194 ± 29	-31 ± 11	-45 ± 7
J0915+0947	216 ± 32	115 ± 17	-58 ± 8	$+18 \pm 7$
J1011+2450	436 ± 65	772 ± 116	$+54 \pm 17$	$+9 \pm 30$
J1113+3238	147 ± 22	106 ± 16	$+63 \pm 36$	$+26 \pm 35$
J1257+1925	516 ± 77	457 ± 69	$+23 \pm 27$	$+33 \pm 22$
J1309+5503	137 ± 21	83 ± 12	-50 ± 23	$+45 \pm 15$
J1555+0239	291 ± 44	143 ± 21	$+11 \pm 14$	-3 ± 27
J2326–0023	115 ± 17	101 ± 15	-23 ± 62	-11 ± 9

Note. — These are all confirmed DA WDs included in either the Eisenstein et al. (2006b) or Kleinman et al. SDSS catalogs.

(Tremblay et al. 2011a; Holberg & Bergeron 2006; Kowalski & Saumon 2006) to determine their absolute magnitudes in each of the five SDSS bands, taking into account the best fit for Galactic reddening.⁷ The distance to each primary is then the average of the distances derived in each band.⁸ Formally, the uncertainties associated with these distances are very small (a few percent). However, these do not reflect the hard-to-quantify uncertainties in the model grids, and we therefore adopt a more realistic uncertainty of 15% for these distances.

Determining photometric distances to our candidate secondaries, which generally lack SDSS spectroscopy, is less straightforward. While T_{eff} can be derived from SDSS

⁷One candidate primary’s T_{eff} and $\log g$ values in the Kleinman et al. catalog were unusable because the code we use to generate these values rejected the associated calibrations. We obtain T_{eff} and $\log g$ estimates for this WD by redoing the fit (K. Oliveira, private communication).

⁸Fits to the grids also provide cooling ages and masses.

photometry to within a few 100 K, the typical photometric errors are sufficient to create uncertainties of order half a decade in the derived $\log g$. As a result, one typically assumes $\log g = 8.0$ (the Kleinman et al. DA sample is strongly peaked at this value). We compare the distances calculated in this manner for our candidate primaries to those derived from their spectroscopically determined T_{eff} and $\log g$ values. We find that they are consistent only to within a factor of 2. In general, therefore, the photometric distance uncertainties are too large for us to differentiate between real and spurious binaries based on comparisons of the distance to the two stars.

There are eight candidate pairs in which both components have SDSS spectra. We provide the spectroscopically derived distances and cataloged RV measurements for these WDs in Table 3.2 and discuss these systems in more detail in Section 3.4.

3.3.3 Estimating the Purity of Our Sample

We use two methods to test the robustness of our selection. First, we estimate the overall contamination of our sample by shifting the positions of our primary WDs and using the same photometric and proper motion criteria to identify (false) companions to these shifted primaries. Second, we use the Monte Carlo approach developed by Dhital et al. (2010) to estimate how likely it is to find a random star whose characteristics match those of our candidate primaries.

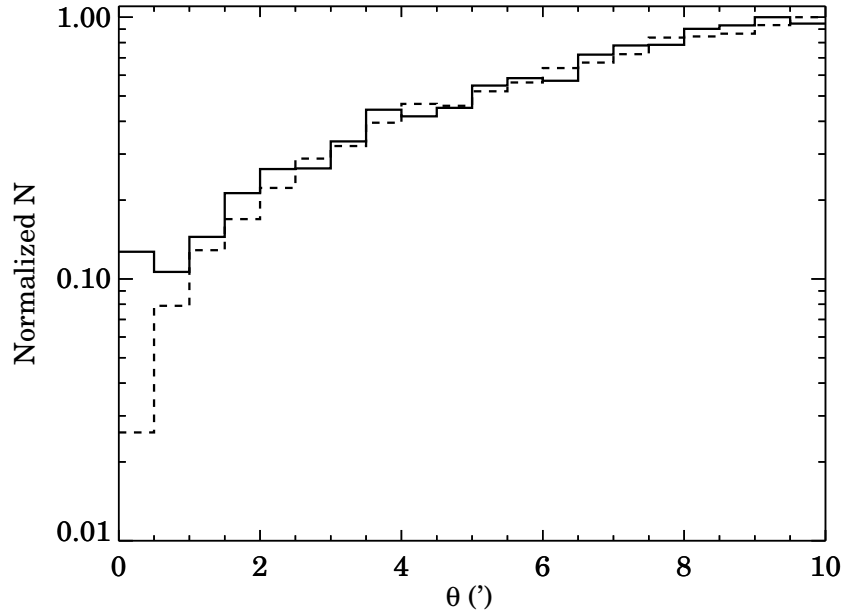


Figure 3.4 θ distribution of real (solid line) and of false (dashed) candidate CPMBs. The primary WD positions were shifted by $\pm 1^\circ$ in both α and δ ; we then applied our method for identifying common proper motion companions to these shifted stars. There is an excess in the distribution of real candidates for $\theta \leq 1.5 - 2'$; at larger θ , the contamination by false pairs is essentially 100%.

3.3.3.1 Empirical False Positive Determination

We shift the positions of our primary DA WDs four times ($\pm 1^\circ$ in both α and δ) and use the μ cuts described above to identify candidate proper-motion companions to these stars. In Figure 3.4, we compare the normalized θ distribution of the resulting population of false candidate CPMBs after these shifts and that of the 7129 candidate CPMBs identified when using the true DA positions. There is an excess in the distribution of real candidates for $\theta \leq 1.5 - 2'$, while at larger separations, the distributions are equivalent, suggesting that most of our actual candidates are due to random matches.

In Figure 3.5, we compare the θ distribution for the candidate DWDs selected from the real CPMB candidates to that for the false candidate CPMBs shown in Figure 3.4.

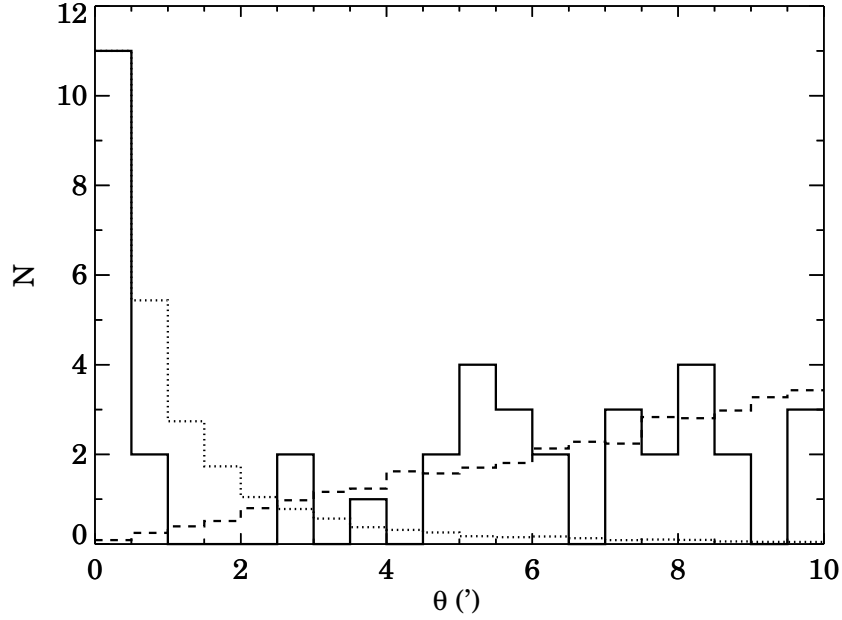


Figure 3.5 θ distribution of the 41 actual DWD candidates (solid line) compared to that of the artificially generated candidate CPMBs (dashed line). The dotted line is the predicted distribution from population synthesis (shown in Figure 3.2) normalized to the first bin in the real distribution, and suggests that our sample is incomplete at $\theta < 2'$. Our distribution of real candidates includes more candidates at large θ than is expected from our population synthesis results, and is strongly contaminated for $\theta > 2'$.

Given the small number of candidate DWDs, we also plot the predicted distribution for DWDs from Figure 3.2 normalized to the first θ bin in our distribution of real candidates. While Figure 3.4 suggests that true binaries are most likely at separations $\leq 1'$, the total expected number of observed wide DWDs (dotted line in Figure 3.5) is significantly larger than the expected number of false positives (dashed line) out to $\theta \sim 2'$. Although none of our actual candidates have $1' < \theta < 2'$, our results suggest that such DWDs, if found in future searches using similar constraints, are likely to be true binaries.

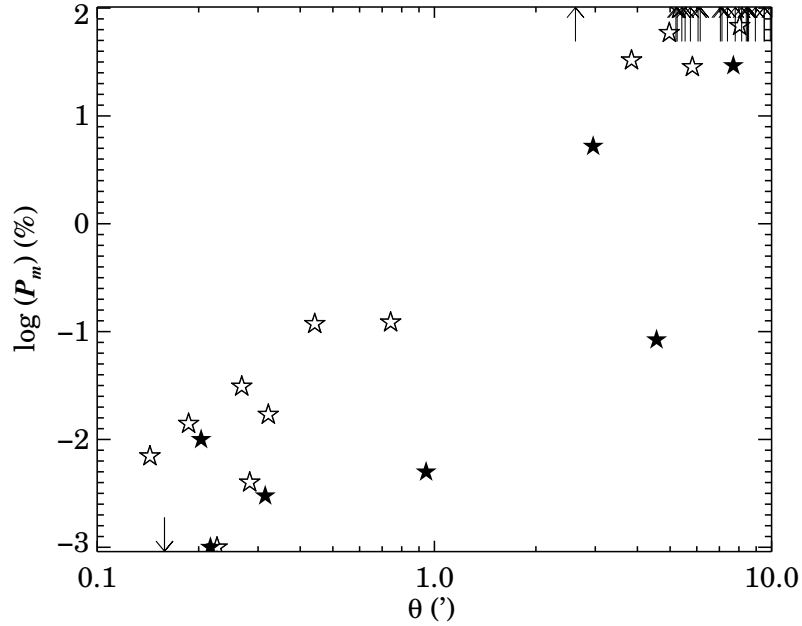


Figure 3.6 Percentage of model realizations that return a random star with the same properties as those of the 41 primary WDs in our candidate DWD binaries; θ is the separation of the corresponding candidate DWDs. The arrows indicate WDs for which P_m is either less than or greater than the y-axis limits. P_m can be $>100\%$ because a given realization may have more than one star with properties matching those of the candidate being tested. Note that there is a primary at $\theta \sim 5'$ with $P_m \sim 100\%$ and two primaries at $\theta \sim 8'$ that are also partially covered by the arrows. 13 primaries have $P_m < 1\%$ and $\theta < 2'$.

3.3.3.2 Galactic Model

Each realization of the Dhital et al. (2010) Galactic model populates a $30' \times 30'$ conical volume centered at the position of the primary WD up to distances of 2500 pc from the Sun. The model assigns a position in six-dimensional phase space to each simulated star, assuming three kinematic components of the Galaxy corresponding to thin disk, thick disk, and halo populations.

After 10^5 realizations of the model, we count the number of rendered stars for which μ matches $\mu_{primary}$ (as defined by Equation 3.2) and that are at a separation from the primary

smaller than or equal to the separation of the corresponding candidate binary. A matching star also has to be at a distance consistent with the distance to the primary WD to within the quadratic sum of the distance uncertainties to the primary and secondary in the binary being tested. In most cases, this corresponds to searching a relatively large volume along the line-of-sight for matches, since while the spectroscopic distances uncertainties are 15%, the photometric distance uncertainties are taken to be 100%. For the eight primaries whose secondaries also have spectroscopic distances and RV measurements (see Table 3.2), the searched volume is smaller, and we further require that a match have an RV consistent with that of the primary WD to within 1σ . Unsurprisingly, this results in a systematically lower number of random matches to the primaries in these pairs.

Figure 3.6 shows the percentage P_m of realizations that return a random star whose properties match those of our 41 candidate primary WDs. These results are in agreement with those from our first test: finding a random match within $2'$ of one of our primary WDs is extremely unlikely, while pairs with $\theta \gtrsim 5'$ are much more likely to be random matches. Interestingly, however, this test suggests that there are systems with $2' < \theta < 5'$ that are more likely to be real than random, as the likelihood of finding a random star with properties matching those of the WD primaries is small.

Table 3.3 High-Confidence Candidate Wide DWDs

Name	α	δ	g (mag)	μ_α (mas/yr)	μ_δ (mas/yr)	Type	θ (")	P_m	Ref.
J0000–1051	00:00:22.5	–10:51:42.1	18.91 ± 0.04	$+45.3 \pm 4.6$	-25.3 ± 4.6	DA	16.1	<0.1%	1,2
	00:00:22.8	–10:51:26.6	20.21 ± 0.04	$+42.3 \pm 4.1$	-24.3 ± 4.1				
J0029+0015 ^a	00:29:25.6	+00:15:52.7	18.48 ± 0.03	-28.9 ± 3.1	-23.0 ± 3.1	DA	8.6	<0.1%	1,2
	00:29:25.3	+00:15:59.8	19.59 ± 0.02	-27.9 ± 3.6	-23.9 ± 3.6				
J0332–0049	03:32:36.6	–00:49:18.4	18.20 ± 0.03	-24.8 ± 5.4	-23.6 ± 5.4	DA	18.9	<0.1%	1,2,3,4
	03:32:36.9	–00:49:36.9	15.64 ± 0.02	-30.9 ± 4.5	-23.3 ± 4.5	DA			
J1002+3606	10:02:44.9	+36:06:29.5	18.92 ± 0.03	-32.9 ± 3.3	-27.5 ± 3.3	DA	26.5	0.12%	1,2
	10:02:45.8	+36:06:53.3	19.04 ± 0.02	-29.9 ± 3.4	-27.0 ± 3.4				
J1054+5307 ^b	10:54:49.9	+53:07:59.2	17.92 ± 0.04	-113.9 ± 3.1	-38.4 ± 3.1	DA	44.5	0.12%	1,2,4,5
	10:54:49.2	+53:07:15.2	17.52 ± 0.03	-112.9 ± 2.9	-36.0 ± 2.9	DA			
J1113+3238 ^c	11:13:19.4	+32:38:17.9	19.03 ± 0.03	-162.9 ± 3.1	$+58.0 \pm 3.1$	DA	56.7	<0.1%	2
	11:13:22.6	+32:38:58.9	19.12 ± 0.04	-158.8 ± 3.2	$+58.0 \pm 3.2$	DA			
J1203+4948	12:03:11.5	+49:48:32.4	19.03 ± 0.03	-97.6 ± 3.4	-36.5 ± 3.4	DA	19.3	<0.1%	2
	12:03:11.0	+49:48:50.8	17.35 ± 0.02	-98.2 ± 2.9	-39.1 ± 2.9				
J1257+1925	12:57:20.9	+19:25:03.7	19.88 ± 0.06	-38.4 ± 5.4	-31.6 ± 5.4	DA	12.2	<0.1%	2
	12:57:21.1	+19:24:51.8	17.07 ± 0.03	-33.0 ± 2.7	-33.5 ± 2.7	DA			
J1412+4216 ^d	14:12:08.9	+42:16:24.6	18.46 ± 0.02	-80.3 ± 3.1	-57.5 ± 3.1	DA	13.6	<0.1%	1,2
	14:12:07.7	+42:16:27.1	15.83 ± 0.01	-81.7 ± 2.7	-61.4 ± 2.7	DA			
J1703+3304	17:03:55.9	+33:04:38.3	18.81 ± 0.02	-1.8 ± 3.4	-51.2 ± 3.4	DA	11.2	<0.1%	1,2
	17:03:56.9	+33:04:35.8	18.16 ± 0.01	$+0.3 \pm 3.1$	-50.5 ± 3.1				
J2115–0741 ^e	21:15:07.4	–07:41:51.5	17.47 ± 0.02	-25.2 ± 2.9	-117.2 ± 2.9	DA	17.0	<0.1%	1,2
	21:15:07.4	–07:41:34.5	16.81 ± 0.01	-30.0 ± 2.8	-117.9 ± 2.8				
J2326–0023 ^e	23:26:58.8	–00:23:39.9	19.33 ± 0.05	$+51.6 \pm 3.3$	-30.7 ± 3.3	DA	9.5	<0.1%	1,2
	23:26:59.3	–00:23:48.1	17.49 ± 0.02	$+53.0 \pm 2.8$	-28.8 ± 2.8	DA			

^a The secondary in this pair has an unidentified SDSS spectra.

^b J1054+5307 is a wide DWD previously identified by McCook & Sion (1999).

^c The secondary in J1113+3238 is included in the hypervelocity star survey of Lépine & Shara (2005).

^d The secondary in J1412+4216 is included in the hypervelocity star survey of Brown et al. (2007).

^e J2115–0741 and J2326–0023 were proposed as wide DWDs by Greaves (2005).

References: 1–Eisenstein et al. (2006b), 2–Kleinman et al., 3–Wegner et al. (1987), 4–McCook & Sion (1999), 5–Oswalt & Strunk (1994), 6–Green et al. (1986).

3.4 Results and Discussion

3.4.1 New DWDs

Based on the tests described above, we set $\theta < 2'$ and $P_m < 1\%$ as our criteria for identifying true pairs. Of the candidate pairs with SDSS spectra for both WDs, J1011+2450 and J1555+0239 have $\theta > 2'$ and $P_m > 1\%$, and are therefore very likely to be random

alignments. The distance and RV data in Table 3.2 are consistent with this, as the disagreements in one or both measurements are significant. J0915+0947, for which $\theta = 4.5'$, does have $P_m < 1\%$, but the RV measurements for the two WDs are highly discrepant (-58 ± 8 and $+18 \pm 7$ km/s), implying that this is a random match.

Conversely, five pairs listed in Table 3.2 have $\theta < 2'$ and $P_m < 1\%$: J0332–0049, J1113+3238, J1257+1925, J1309+5503, and J2326–0023. We check the distances to the two components and the RV measurements for these for consistency: of the five, J1309+5503 is the only one for which the disagreements between the measurements for each DA (-50 ± 23 and $+45 \pm 15$ km/s) are significant enough to eliminate it from our list of candidate pairs. We identify the other four pairs as high-confidence candidate DWD systems and present them along with the eight systems that lack SDSS spectra for the secondaries but also meet our criteria in Table 3.3.

In addition to the four pairs with SDSS spectra for both DAs, a SIMBAD⁹ search finds that two systems in Table 3.3 have secondaries classified as DAs by McCook & Sion (1999). Spectroscopic follow-up is clearly needed to confirm the nature of the secondary in the remaining six systems. For objects $17 \leq g \leq 19$ mag, Girven et al. (2011) estimate that their photometric selection leads to a quasar contamination rate of $\lesssim 35\%$, primarily at the faint end. At the bright end, Girven et al. (2011) find that early-type Main Sequence stars and subdwarfs are the main contaminants, and estimate their contamination rate to be $\lesssim 20\%$.

However, the contamination rate drops sharply when a proper motion constraint is applied: if one imposes $\mu \gtrsim 20$ mas/yr, the quasar contamination rate becomes negligible and $\sim 90\%$ of the hot stars are eliminated. Considering that our high-confidence pairs all

⁹<http://simbad.u-strasbg.fr/simbad/>

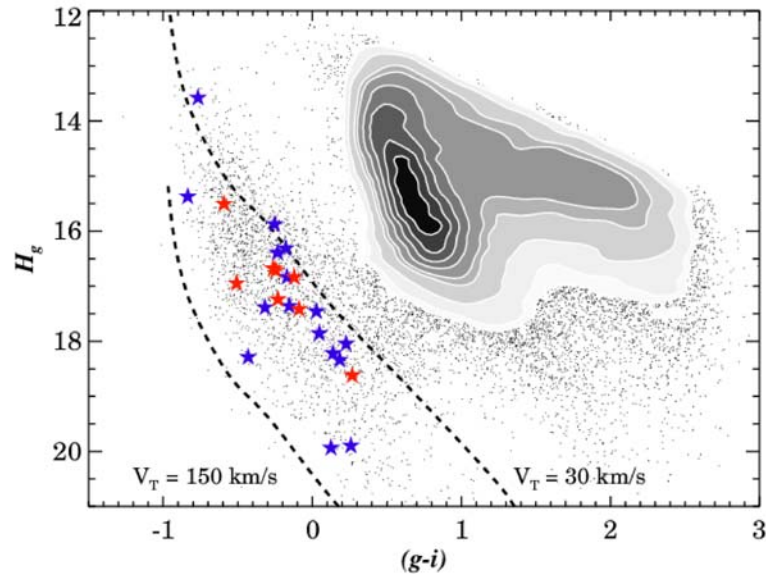


Figure 3.7 Reduced proper motion as a function of $(g - i)$ for the SDSS stars presented in Figure 3.3 (points and contours) and for members of our high-confidence candidate DWDs. Spectroscopically confirmed WDs are shown as blue stars, while the red stars lack spectra. The $V_T = 30$ km/s line marks the expected location of disk WDs and the $V_T = 150$ km/s line that of halo WDs (Kilic et al. 2006). All of our candidates lie in the expected region for WDs, far from the Main Sequence locus.

have $\mu > 30$ mas/yr, we expect that no more than one of our high-confidence pairs contains a non-WD.

As a further test, we calculate the reduced proper motion (H_g) for each of our pairs. H_g , which combines photometric and kinematic information, is an effective tool for separating WDs from other objects (Kilic et al. 2006). Figure 3.7 shows the reduced proper motions for the >99,000 SDSS stars presented in Figure 3.3, as well as lines of constant transverse velocity representing the disk and halo WD populations ($V_T = 30$ and 150 km/s, respectively). All of the stars in our high-confidence pairs, whether spectroscopically confirmed as WDs or lacking spectra, lie far from the Main Sequence locus and are consistent

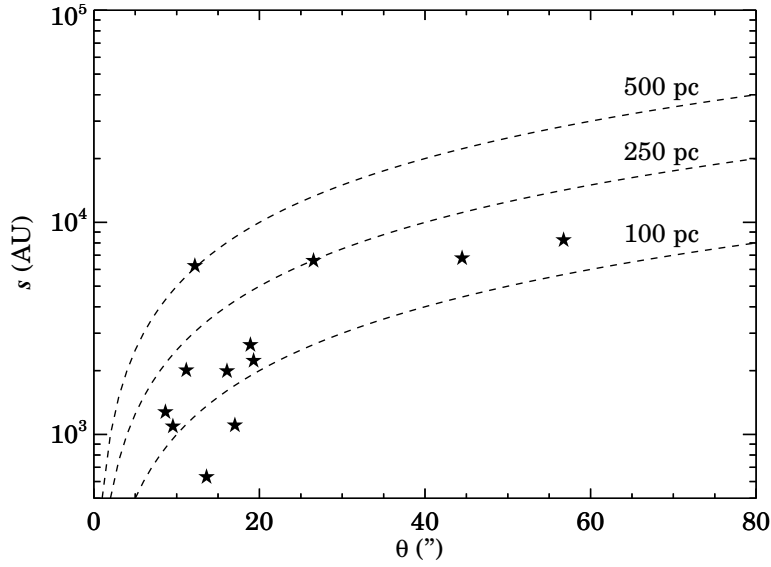


Figure 3.8 Projected separation of our high-confidence DWDs as a function of θ . We use the spectroscopically determined distances to the primary WDs to estimate s . Lines of constant distance are plotted as dashed lines.

with being WDs.

We note that two of these pairs, J2115–0741 and J2326–0023, were identified as wide DWDs candidates by Greaves (2005) in a search for CPMBs in SDSS Data Release 1.

In Figure 3.8, we plot s , the projected orbital separation found using the spectroscopically derived distance to the primary WDs, as a function of θ for our high-confidence DWDs. We find no pair with $s > 10^4$ AU, while our population synthesis predictions are that a significant population exists at such separations; we also appear only to be identifying very nearby DWDs. However, our method cannot yield a complete sample: Girven et al. (2011) estimate the completeness of WD spectroscopic coverage in SDSS at only $\sim 44\%$ for $g \leq 19$ mag.

Our tightest pair has $\theta \sim 8''$, while we expect binaries to exist at smaller θ . This is due to the difficulty in matching an object in the SDSS catalog to its USNO-B counterpart

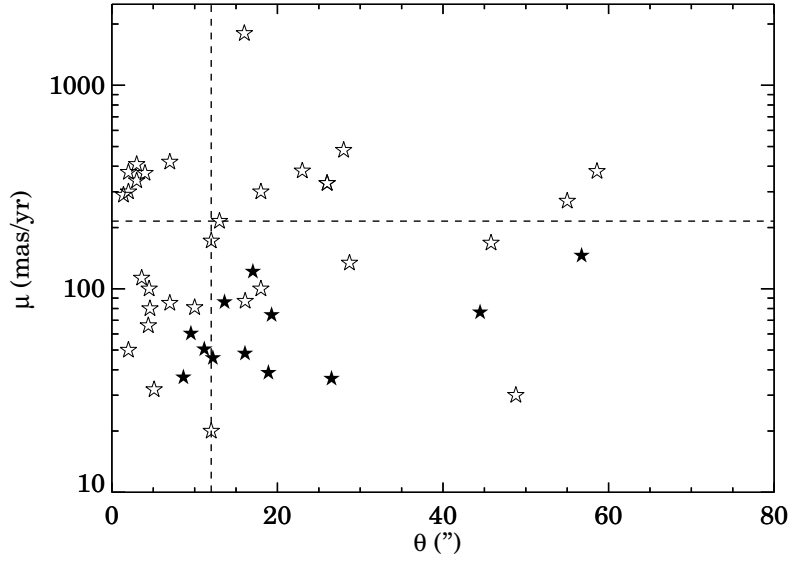


Figure 3.9 DWD proper motions as a function of θ . Previously known systems are plotted as open stars, while our high-confidence pairs are filled stars. The dashed lines indicate the median μ and θ values for the previously known DWDs; our high-confidence systems are a significant addition to the sample of pairs with small μ and large θ .

when the matching radius is of order the separation with another object.

3.4.2 Comparison with Previously Known DWDs

Table 3.4 is a compilation of the properties of all of the wide DWDs reported to date. We include our 12 high-confidence DWDs and 33 systems from the literature and present T_{eff} , $\log g$, mass, and cooling age (τ), when these measurements exist. The available data and their quality vary greatly from system to system, but simple comparisons can be made between our sample and the previously known DWDs. In Figure 3.9, we show μ as a function of θ for the previously known systems and for our pairs. Our high-confidence DWDs are a significant addition to the sample of pairs with small μ (<200 mas/yr) and large θ ($>10''$).

Table 3.4 Wide DWDs – Derived Quantities

Name	θ (")	μ (mas/yr) ^a	T_{eff} (K)	Primary log g	M (M_{\odot})	log τ	T_{eff} (K)	Secondary log g	M (M_{\odot})	log τ	Ref.
High-Confidence Wide DWDs Identified in This Work											
J0000–1051	16.1	49.7±8.7	8598±72	8.32±0.13	0.80±0.09	9.23±0.11					
J0029+0015	8.6	36.8±6.7	9947±67	8.22±0.08	0.74±0.06	8.97±0.08					
J0332–0049 ^b	18.9	36.5±9.9	11012±50	8.27±0.04	0.77±0.03	8.85±0.02	34288±42	7.83±0.02	0.58±0.01	6.60±0.01	
J1002+3606	26.5	37.2±6.1	11326±181	8.05±0.13	0.63±0.08	8.68±0.09					
J1054+5307 ^b	44.5	77.6±5.0	10985±60	8.08±0.05	0.65±0.03	8.73±0.04	11120	8.01			1,2,3
J1113+3238	56.7	147.3±5.8	6853±69	7.56±0.20	0.38±0.08	8.99±0.08	7580±88	8.40±0.15	0.85±0.10	9.46±0.09	
J1203+4948	19.3	73.6±5.3	7064±46	8.05±0.10	0.62±0.06	9.21±0.08					
J1257+1925	12.2	46.9±8.3	11829±218	7.72±0.14	0.46±0.06	8.46±0.05	47818±590	7.85±0.05	0.62±0.02	6.33±0.02	
J1412+4216	13.6	84.4±5.1	6706±70	8.76±0.15	1.07±0.09	9.64±0.01					
J1703+3304	11.2	50.9±6.0	9587±75	8.11±0.11	0.66±0.07	8.92±0.09					
J2115–0741	17.0	120.7±5.6	7913±32	8.16±0.05	0.69±0.03	9.19±0.04					
J2326–0023	9.5	60.2±6.1	7503±67	8.42±0.12	0.87±0.07	9.48±0.05	10513±46	8.24±0.05	0.75±0.04	8.90±0.04	
Previously Identified Wide DWDs											
LP406–62/63	28	480	5320	8.0	0.58	9.63	4910	8.0	0.58	9.78	1,2,4
LP707–8/9	12	172									1
LP647–33/34	2	374									1
LP197–5/6	7	420				9.48				9.94	1,5
RE J0317–853 ^c	7	85	30000–50000	ζ1.1	~8.4		16000	8.19	0.76–0.84	~8.4	6,7
LP472–70/69 ^d	3										1
HS 0507+0434 ^b	18	100	20220	7.99	0.62	7.90	~12000	8.1	0.69	8.71	8
WD 0727+482A/B ^d		1340	5020	7.92	0.53	9.66	5000	8.12	0.66	9.85	9
LP543–33/32	16	1800	4170	7.65	0.39	9.67	4870	8.05	0.6	9.84	1,2,4,9
LP035–288/287	3	340									1
PG 0901+140	3.6	113	9500	8.29		9.10	8250				10,11
PG 0922+162	4.4	66	22740	8.27	0.79	7.95	22130	8.78	1.1	8.41	10,12
J0926+1321 ^c	4.6	80	9500±500		0.62±0.10	8.86	10482±47	8.54±0.03	0.79±6	8.92	13
LP462–56A/B	4	370	10240	8.0	0.58	8.90	8340	7.5	0.35	8.77	1,2
LP370–50/51	13	215									1
LP549–33/32	26	330									1,3
PG 1017+125	48.8	30									10
ESO439–162/163	23	380	5810	8.0	0.57	9.52	4780	8.0	0.57	9.82	1,2,14
GD 322 ^c	16.1	87	14790	7.87	0.54	8.26	6300	7.93	0.54	9.27	10,15
LP322–500A/B	12	20									1
LP096–66/65	18	300									1,16
L151–81A/B	2	50	14050	7.96	0.57	8.38	12000				1,17,18,19
J1507+5210 ^c	5.1	32	17622±95	8.13±0.02	0.70±0.04	8.17	18000±1000		0.99±5	8.51	13
Gr576/577 ^e	4.5	100	12500	8.34	0.8		9500/8500		0.39/0.56		1,20,21,22
LP567–39/38	2	300									1
G206–17/18	55	270	7380	7.65		8.93	6480	7.75		9.12	1,9
G021–15 ^e	58.6	378	10000/15000	8.0/7.4	0.6/0.35	8.08	4750	8.0	0.57		9,10
GD 392	45.8	168	12220	9.09	1.23	9.22	~3600				10,19,23
G261–43	1.4	289	16000				5000				10,24
HS 2240+1234	10	81	14700	8.1			13200	7.9			8
LP701–69/70	26	330				9.34				9.88	1,5
GD 559	28.7	134									10,25
LP077–57/56	3	409				9.62				9.92	1,5

^a As in the text, μ refers to the total proper motion of the system.

^b J0332–0049, J1054+5307, and HS 0507+0434 include a ZZ-Ceti-type variable.

^c The primaries in RE J0317–853 and J0926+1321 and secondaries in GD 322 and J1507+5210 have been identified as magnetic WDs.

^d LP472–70/69 lacks a published μ , and WD 0727+482A/B lacks a published θ .

^e Gr576/577 and G021–15 have both been identified as triple degenerate systems.

References: 1–Sion et al. (1991), 2–Bergeron et al. (1997), 3–Eisenstein et al. (2006b), 4–Kilic et al. (2009), 5–Hintzen et al. (1989), 6–Barstow et al. (1995), 7–Külebi et al. (2010), 8–Jordan et al. (1998), 9–Bergeron et al. (2001), 10–Farihi (2004a); Farihi et al. (2005), 11–Liebert et al. (2005c), 12–Finley & Koester (1997), 13–Dobbie et al. (2012a), 14–Ruiz & Takamiya (1995), 15–Girven et al. (2010), 16–Kleinman et al. (2004), 17–Oswalt et al. (1988), 18–Wood & Oswalt (1992), 19–Bergeron et al. (2011), 20–Sanduleak & Pesch (1982), 21–Greenstein et al. (1983), 22–Maxted et al. (2000), 23–Farihi (2004b), 24–Zuckerman et al. (1997), 25–McCook & Sion (1999).

Note. – The quoted values and uncertainties for T_{eff} and log g are from the Kleinman et al. catalog. Uncertainties on the WD masses and cooling ages are formal and do not include significant systematic uncertainties.

Interestingly, four of the systems listed in Table 3.4 include WDs with masses $\lesssim 0.5 M_{\odot}$. The Galaxy is not thought to have had time to produce such low-mass WDs, as the youngest WDs in the oldest Galactic globular clusters have $M \sim 0.5 M_{\odot}$ (Hansen et al. 2007). Instead, WDs with $M < 0.5 M_{\odot}$ are likely to form in close binaries whose evolution included a phase of mass transfer. These four systems are therefore excellent candidate triple systems, with the low-mass WD likely to have a close-by companion. (Two additional systems in the literature are triple degenerate systems.)

The previously known pairs include four WDs that are in the Kleinman et al. WD catalog. Of these, only LP 128–254/255 (J1054+5307) is recovered by our search; our primary in this case is LP 128–255. PG 0901+140 and J1507+5210 were excluded as candidate binaries because three of the four WDs in these pairs lack proper motion information in SDSS. LP 549–33/32 is not recovered because the secondary (in our case, LP 549–32) has colors outside the regions defined by Girven et al. (2011) for DA WDs; indeed, McCook & Sion (1999) classify it as a DC WD. The non-detection of three of these four systems is therefore not surprising, but confirms that our reliance on the Kleinman et al. DA catalog leads us to miss a number of wide DWDs in the SDSS footprint.

3.4.2.1 Binary Separation and Stability

As mentioned in Section 3.2, wide DWD orbits are thought to be $\sim 5\times$ larger than those of their progenitor systems; mass lost as the stars evolve expands the orbits from a more compact state (Greenstein 1986b). We compare the projected orbital separations for the DWDs produced by our population synthesis to those for the wide Main Sequence pairs

identified by Dhital et al. (2010) in Figure 3.10. (We also show the individual values for our 12 DWDs; this sample is too small and incomplete for a comparison to the separation distribution to be meaningful.)

The apparent deficit of progenitor pairs for the synthesized DWDs with $10^2 \lesssim a \lesssim 10^3$ AU is unsurprising, as those progenitors presumably are tighter than the tightest pairs to which Dhital et al. (2010) are sensitive ($\theta \sim 8''$). More interesting is the apparent lack of a significant population of DWDs wider than the widest Main Sequence pairs identified by Dhital et al. (2010). This may be because as the widest Main Sequence pairs evolve to larger separations, they become more likely to be disrupted by interactions with other bodies in the Galaxy.

One test of this hypothesis is to compare the ages of our DWDs to those of the Dhital et al. (2010) binaries. We use the cooling ages of our primaries as a rough estimate of the cooling ages of the systems (we do not know whether they evolved first). This cooling age provides an upper limit on the DWDs' lifetimes as truly wide binaries, since it is only after both stars have evolved into WDs that the pairs reach maximum separations. The characteristic lifetimes of the DWDs in Table 3.4 derived in this manner are all $\gg 1$ Gyr. By contrast, Dhital et al. (2010) find that many of their pairs have characteristic lifetimes $\lesssim 1$ Gyr. A larger sample of DWDs will allow for an improved test of this hypothesis.

3.4.2.2 Initial-Final Mass Relation

Most of the 45 systems in Table 3.4 lack spectroscopic information, and many of the WDs with spectra have large error bars on T_{eff} or $\log g$ because these were derived from low

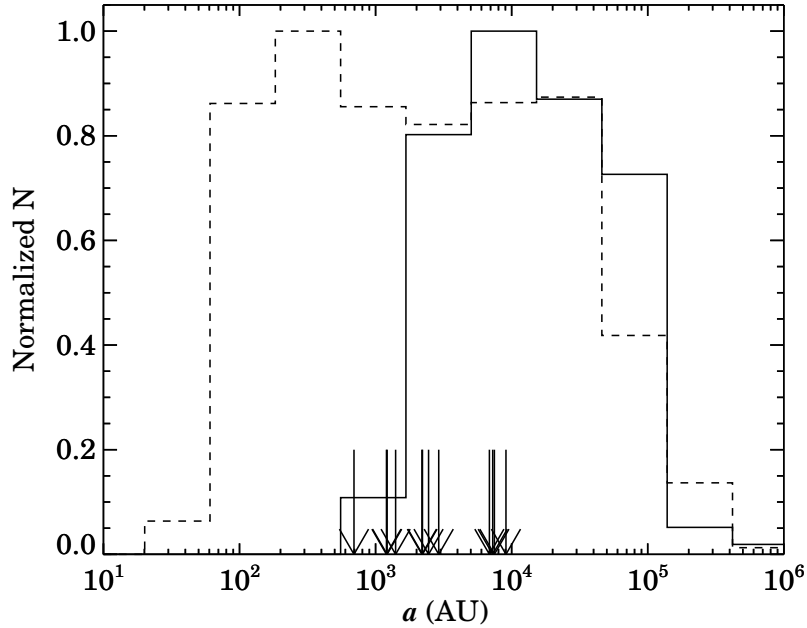


Figure 3.10 Normalized orbital separation distributions for the DWDs generated by our population synthesis (dashed line) and for the wide Main Sequence binaries identified by Dhital et al. (2010, solid line). For the latter, we use $a = 1.1 \times s$ to convert the observed (projected) orbital separations into true orbital separations (Dupuy & Liu 2011). The synthesized systems are those that remain after perturbing effects are taken into account (dashed line in Figure 3.1). The projected separations for the 12 high-confidence DWDs identified here have also been converted; their orbital separations are indicated by the arrows.

signal-to-noise spectra. Such errors can propagate into large uncertainties in the masses and cooling ages. In principle these wide DWDs can be used to constrain the IFMR with a method similar to that of Finley & Koester (1997), we defer this question to Chapter 4. It is clear from the imprecision and heterogeneity of the available spectroscopic data for the wide DWD sample in Table 3.4 that these data in their current form cannot constrain the IFMR. Spectroscopic follow-up is required.

For now, as a simple consistency check, we compare the cooling ages and masses of the WDs in the eight systems for which both stars have spectroscopically derived T_{eff}

and differing masses (and that are not a potential triple system). We expect that in these binaries the more massive WD has a larger cooling age. Our simple test holds for all eight of these systems.

3.5 Conclusions

In this chapter to expand the sample of known DWDs, we adapted the method of Dhital et al. (2010) to search the SDSS DR7 catalog for WD common proper motion companions to spectroscopically confirmed DA WDs out to $\theta = 10'$. We found 41 candidate wide DWDs. These are pairs in which the secondary's colors fall within 0.5σ of the region in $(g - r)$ versus $(u - g)$ color space occupied by DA WDs (Girven et al. 2011). We then used two complementary techniques to measure the contamination of our sample by randomly aligned false matches. We first estimated the overall contamination of our sample by false binaries by shifting the positions of our primaries several times by 1° and applying our μ and color criteria to identify false companions to the shifted primaries. We also used the Monte Carlo approach developed by Dhital et al. (2010) and searched 10^5 iterations of the line-of-sight to each of our primaries for stars whose properties randomly match those of these WDs.

These two tests suggest that, absent other information, the highest probability real pairs in our sample are those with $\theta < 2'$ and primaries with random matches in fewer than 1% of our rendered lines-of-sight. 13 of our candidates meet these criteria; one of these pairs has inconsistent spectroscopically derived distance and RV measurements for the two WDs, so that our final sample includes 12 high-confidence wide DWDs. (Three

of these were previously reported as candidate DWDs.)

Four of these pairs have SDSS spectra for both DAs, while two others have secondaries classified as DAs by McCook & Sion (1999). Spectroscopic follow-up is clearly needed to confirm the nature of the secondaries in the remaining six systems. However, a color selection combined with a minimum proper motion requirement returns a very clean sample of DAs (Girven et al. 2011); furthermore, based on their reduced proper motions, all of our candidates are consistent with being WDs. We therefore expect no more than one of our high-confidence pairs to contain a non-WD. These systems are a significant addition to the known population with small μ (<200 mas/yr) and large θ ($>10''$).

Girven et al. (2011) estimate the completeness of WD spectroscopic coverage in SDSS at $\sim 44\%$ for $g \leq 19$ mag, and it decreases for fainter magnitudes. Since we would like to extend this technique to the entire SDSS photometric catalog, in Chapter 3 we will further adapt this method to identify new wide DWDs, extending to even fainter magnitudes.

3.6 Acknowledgments

We are grateful to the anonymous referee whose comments improved this work. We thank Sebastian Lépine and Marten van Kerkwijk for useful discussions about identifying false pairs. We thank Kepler Oliveira for obtaining T_{eff} and $\log g$ for a WD primary whose data in our catalog were unusable. We also thank Mukremin Kilic for his help with Figure 3.7.

This research has made use of the SIMBAD database, operated at CDS, Strasbourg, France.

Funding for the SDSS and SDSS-II has been provided by the Alfred P. Sloan Founda-

tion, the Participating Institutions, the National Science Foundation, the U.S. Department of Energy, the National Aeronautics and Space Administration, the Japanese Monbukagakusho, the Max Planck Society, and the Higher Education Funding Council for England. The SDSS Web Site is <http://www.sdss.org/>.

The SDSS is managed by the Astrophysical Research Consortium for the Participating Institutions. The Participating Institutions are the American Museum of Natural History, Astrophysical Institute Potsdam, University of Basel, University of Cambridge, Case Western Reserve University, University of Chicago, Drexel University, Fermilab, the Institute for Advanced Study, the Japan Participation Group, Johns Hopkins University, the Joint Institute for Nuclear Astrophysics, the Kavli Institute for Particle Astrophysics and Cosmology, the Korean Scientist Group, the Chinese Academy of Sciences (LAMOST), Los Alamos National Laboratory, the Max-Planck-Institute for Astronomy (MPIA), the Max-Planck-Institute for Astrophysics (MPA), New Mexico State University, Ohio State University, University of Pittsburgh, University of Portsmouth, Princeton University, the United States Naval Observatory, and the University of Washington.

Chapter 4

Constraining the Initial-Final Mass Relation

4.1 Introduction

Accurate mass measurements for large numbers of hydrogen-atmosphere (DA) white dwarfs (WDs), which dominate the WD population, became commonplace with the advent of spectroscopic surveys such as the Palomar-Green Survey (Green et al. 1986) and the Sloan Digital Sky Survey (SDSS; York et al. 2000). These confirmed that the DA mass distribution is strongly peaked at $0.6 M_{\odot}$ (e.g., Kepler et al. 2015). However, matching these final WD masses to initial, zero age Main Sequence masses is challenging, and large uncertainties about which Main Sequence stars evolve into which WDs are still the norm.

⁰This section is a reformatted version of an article by the same name by Jeff J. Andrews, Marcel A. Agüeros, A. Gianninas, Mukremin Kilic, Saurav Dhital, & Scott Anderson that has been recently submitted to the *Astrophysical Journal*. The abstract has been removed, and slight modifications have been made (such as in acronyms) to ensure consistency throughout this dissertation. Portions of this paper's introduction appear in the introduction to this dissertation.

For example, the data cannot accurately tell us which stars produce those $0.6 M_{\odot}$ DAs, with estimates ranging from 1.0 to $2.5 M_{\odot}$ (Weidemann 2000). This implies that predictions for mass loss as stars evolve into $0.6 M_{\odot}$ WDs can differ by $>1 M_{\odot}$.

Sweeney (1976) pioneered the most commonly used method for constraining the initial-final mass relation (IFMR). The cooling age (τ_{cool}) of a WD in an open cluster is derived from spectroscopy, and this age is subtracted from the cluster's age to determine the WD progenitor's Main Sequence lifetime. Using stellar evolution codes, this lifetime is converted into an initial mass M_i ; paired with its spectroscopically determined mass, this M_i then provides a constraint on the IFMR (e.g., Weidemann & Koester 1983; Weidemann 2000).

In practice, this method is often difficult to implement: the open clusters must have accurate ages, member WDs must be identified and separated from contaminating objects, and these often faint WDs must be observed with high-resolution spectrographs. Furthermore, most accessible open clusters are $\lesssim 600$ Myr old, so that only stars with $M_i \gtrsim 3.5 M_{\odot}$ have evolved into WDs (there has been some recent work to identify WDs in older clusters; e.g., Kalirai et al. 2008, 2014).

Finley & Koester (1997) used a different approach. The co-eval WDs in the wide double WD (DWD) PG 0922+162 can be considered to have evolved independently. By comparing the more massive WD to massive WDs with accurate M_i determinations in open clusters, these authors assigned PG 0922+162B a M_i of $5.5\text{--}7.5 M_{\odot}$. Adding the corresponding Main Sequence lifetime to the massive WD's τ_{cool} , Finley & Koester (1997) derived a system age of $\approx 320 \pm 32$ Myr. Finally, these authors calculated the pre-WD

lifetime of the less massive WD by subtracting its τ_{cool} from the system age, and, using stellar evolution codes, found $M_i = 3.8 \pm 0.2 M_{\odot}$ for this WD. The uncertainty on this point in the initial-final mass plane is comparable to that for the best open cluster data.

While promising, this study has not been widely replicated. Until recently, there were only ≈ 35 known wide DWDs, and many were poorly characterized. Many lacked spectra, and even those with spectra were ill-suited to this analysis because of large uncertainties in their τ_{cool} . Furthermore, it has not been clear how to convert observations into robust constraints on the IFMR.¹

In this work, we develop a statistical model that allows any well-characterized wide DWD to constrain the IFMR. We first construct a likelihood function to determine the probability that any particular IFMR fits a sample of wide DWDs, while taking into account observational uncertainties by marginalizing over the underlying parameters from the observables. We then develop a four-parameter piecewise-linear model for the IFMR, and iterate over the model parameters using a Markov Chain Monte Carlo technique to find the best parameters indicated by our wide DWDs.

In Andrews et al. (2012, hereafter Paper I) we presented the results of a search for new DWDs in the SDSS Data Release 7 (DR7; Abazajian et al. 2009). Here, we begin by describing in Section 4.2 the results of a search for DWDs in the larger SDSS Data Release

¹We have found three other instances where this method was applied to a wide DWD. It was first used by Greenstein et al. (1983) on Gr 576/577, but one of the WDs in this pair is composed of an unresolved double degenerate (Maxted et al. 2000). Because of the potential for mass transfer within the unresolved binary system, this is not a good system for constraining the IFMR. Girven et al. (2010) applied the method to PG 1258+593 to constrain the initial mass of its magnetic companion SDSS J130033.48+590407.0. While of use for studying the origin of magnetic WDs (e.g., Dobbie et al. 2012b), this is another instance where the system does not place useful constraints on the IFMR. Recently, Catalán (2015) developed her own form of this method. Although promising, it has generated meaningful constraints for only four systems so far.

9 (DR9; Ahn et al. 2012). We assemble a catalog of 142 candidate and confirmed DWDs that includes new systems, those found in Paper I and in the literature, and those recently published by Baxter et al. (2014). In Section 4.3, we discuss our spectroscopic follow-up observations of a subset of WDs in these binaries, and present the results of our model fits to these spectra. In Section 4.4, we revisit the Finley & Koester (1997) result and develop our hierarchical Bayesian model. We test our model on mock data, then apply it to a well-characterized subset of wide DWDs. In Section 4.5 we discuss our resulting constraints on the IFMR; we conclude in Section 5.5.

4.2 Searching for Wide DWDs

4.2.1 Common Proper Motion Pairs

We first search for DWDs by matching proper motions of WD candidates in SDSS, which requires accurate photometry and astrometry. Although the SDSS Data Release 8 is nearly triple the size of the DR7 photometric catalog, the astrometric solutions are not calibrated against the USNO CCD Astrograph Catalog data (Zacharias et al. 2004), causing a systematic shift of $\approx 50 \text{ mas yr}^{-1}$ (Munn et al. 2008). DR9, however, includes an expanded photometric catalog and improved astrometric solutions (with a precision of a few mas yr^{-1}), which allowed us to expand the search for DWDs described in Paper I. From the $>9 \times 10^8$ primary photometric objects in DR9, we selected those classified as stars ($\text{ptype} = 6$) and matching our photometric and proper motion (μ) quality constraints ($\sigma_{ugr} < 0.15 \text{ mag}$, $\sigma_{iz} < 1.0 \text{ mag}$, $\mu > 35 \text{ mas yr}^{-1}$, $\sigma_{\mu} < 10 \text{ mas yr}^{-1}$).

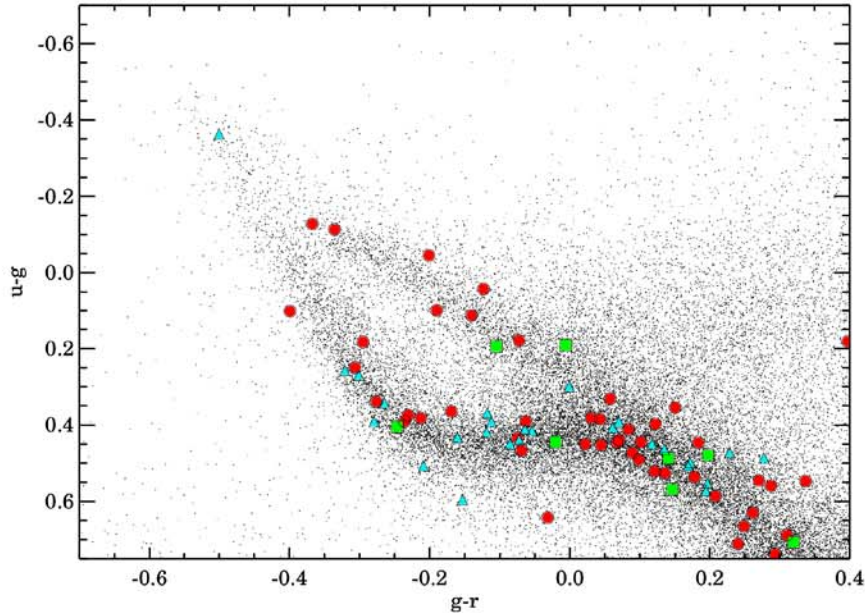


Figure 4.1 $(u - g)$ versus $(g - r)$ for $\approx 4 \times 10^4$ SDSS objects with $\sigma_{ugr} < 0.15$ mag, $\sigma_{iz} < 1.0$ mag, $\mu > 35$ mas yr $^{-1}$, and $\sigma_{\mu} < 10$ mas yr $^{-1}$. The plot boundaries define the box in color space within which we sought to identify new WDs. The sickle-shaped band corresponds to the DA cooling sequence, with hotter, younger WDs toward the upper left, and cooler, older WDs toward the bottom right. The width of the band is primarily due to variations in the DA masses: for example, WDs slightly more massive than the canonical $0.6 M_{\odot}$ have slightly higher surface gravities, and therefore slightly bluer $(u - g)$. The band of objects with bluer $(u - g)$ for a given $(g - r)$ is the cooling sequence for non-DA WDs. Hot DB WDs lie at the upper left of this band; as they cool to $\lesssim 12,000$ K they appear as DC WDs with featureless blackbody spectra. The red circles are the candidate WDs in 23 new candidate wide DWDs identified here; the green squares are candidate WDs in four additional new candidate systems, while the teal triangles are the WDs in the 13 known systems we re-detect.

In Paper I, we used the color-color regions defined by Girven et al. (2011) to identify WDs in $(u - g)$ versus $(g - r)$ space (the regions are shown in Figure 4.4). To include helium-atmosphere DB WDs in this search, we used a more liberal color constraint, selecting those stars with $-0.7 < (g - r) < 0.4$ and $-0.7 < (u - g) < 0.75$. Figure 4.1 shows the $(u - g)$ versus $(g - r)$ colors of the $\approx 4 \times 10^4$ SDSS objects that met our quality constraints and fell within

this region of color space.

Quasars (QSOs) are by far the biggest contaminant in this region of color-color space. Munn et al. (2004) found that requiring $\mu > 10 \text{ mas yr}^{-1}$ eliminated 95% of QSOs with $r < 20 \text{ mag}$. Our $\mu > 35 \text{ mas yr}^{-1}$ criterion should eliminate nearly all QSOs. Contaminating Main Sequence stars and subdwarfs are more difficult to remove, as these objects may overlap with WDs in color and may have $\mu > 35 \text{ mas yr}^{-1}$. As shown in Kilic et al. (2006), however, WDs can be effectively separated from blue stars in a reduced proper motion (H_r) diagram.²

Figure 4.2 is H_r versus $(g - i)$ for the objects in our sample. Because of their smaller radii, WDs are clearly separated from subdwarfs (and Main Sequence stars). We used the dashed line in Figure 4.2, adapted from Smith et al. (2009), to separate subdwarfs from WDs, thereby reducing our sample to $\approx 34,000$ objects.

Next, we searched for common proper motion matches within these data. We defined a match as occurring when two WDs had an angular separation $\theta < 5'$, and, following Dhital et al. (2010), that their proper motions have a matching parameter $\Sigma^2 < 2$.³ Among our $\approx 34,000$ objects, we thus identify 57 candidate DWDs.

Some of these candidate pairs may contain WDs at different distances and with different radial velocities, which, when projected on the sky, happen to result in $\Sigma^2 < 2$. Since the probability of finding a randomly aligned pair depends on the volume of phase space being searched, the random alignment likelihood should scale linearly with θ , and

$$^2H_r = r + 5 \log \mu + 5.$$

$$^3\Sigma^2 = \left(\Delta\mu_\alpha / \sigma_{\Delta\mu_\alpha} \right)^2 + \left(\Delta\mu_\delta / \sigma_{\Delta\mu_\delta} \right)^2, \text{ where } \Delta\mu \text{ is the difference in } \mu \text{ measured in right ascension } (\alpha) \text{ and declination } (\delta), \text{ and } \sigma_\mu \text{ is the error in } \mu.$$

a critical θ should separate pairs more likely to be real from those more likely to be contaminants. In Paper I, we found that pairs with $\theta < 1'$ are most likely real. However, because our selection criteria have changed, we re-estimate this critical θ .

Figure 4.3 shows a clear excess in the number of candidate pairs with $\theta < 100''$. We determine a linear fit to the distribution of systems with $\theta > 100''$, those that are most likely to be random alignments. Extrapolating this fit to those pairs with smaller θ

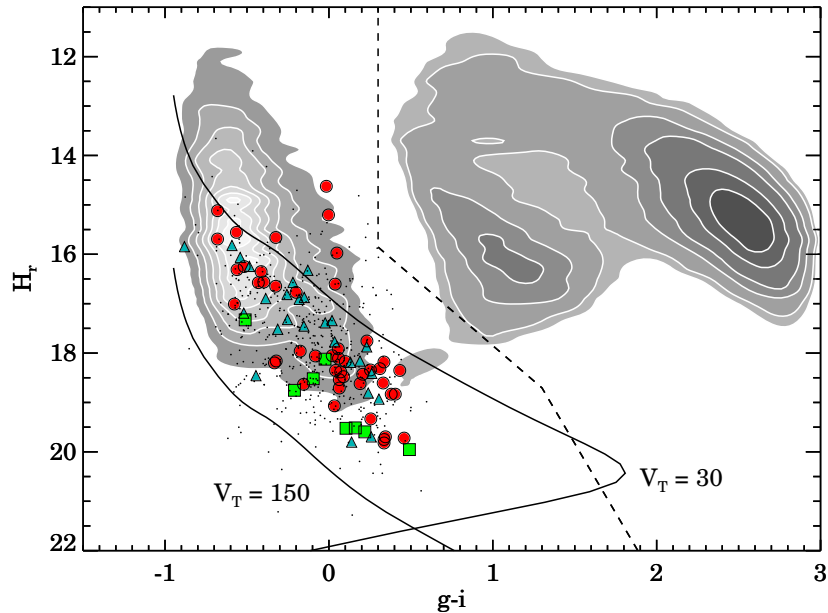


Figure 4.2 Reduced proper motion H_r versus $(g - i)$ for the objects in Figure 4.1. The locus at $(g - i) \approx 2.5$ is of Main Sequence stars, while that at $(g - i) \approx 1$ is of subdwarfs. The spectroscopically confirmed WDs in the Kleinman et al. (2013) SDSS catalog with a measured μ are shown by the contours peaking at $(g - i) \approx -0.5$. We used the dashed line, adapted from Smith et al. (2009), to separate subdwarfs from candidate WDs. The solid lines represent the locations of WDs for transverse velocities $V_T = 30 \text{ km s}^{-1}$ (corresponding to the disk population) and 150 km s^{-1} (the halo population), and show that our candidates are likely in the Galactic disk. The symbols are the same as in Figure 4.1. Our candidates have systematically larger H_r because we require that they have relatively large μ and because the SDSS photometric catalog extends to fainter magnitudes than the spectroscopic catalog used by Kleinman et al. (2013) to identify WDs.

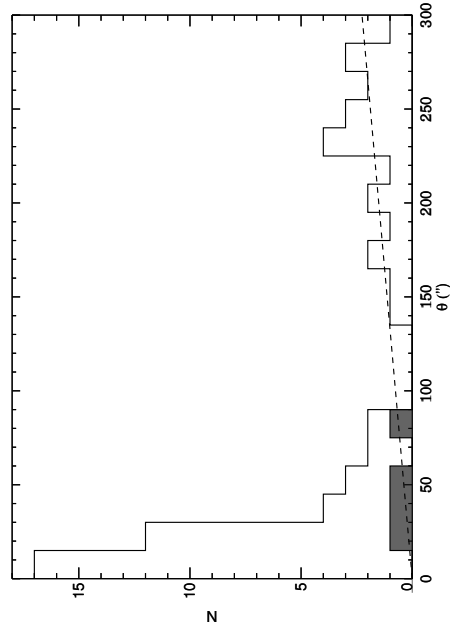


Figure 4.3 Angular separation (θ) distribution of our candidate common proper motion DWDs. The four pairs with $\Sigma^2 > 2$ but $\mu > 80 \text{ mas yr}^{-1}$ are shown in gray. The probability that a given pair is due to a random alignment should increase roughly linearly with θ . The dashed line shows the best fit line to the distribution beyond $100''$, where the noise dominates, assuming $N(\theta) \propto \theta$ and that the line goes through the origin. Extrapolating this fit to smaller θ suggests that pairs with $\theta < 100''$ are real pairs, while pairs at larger θ are physically unassociated.

suggests that $\lesssim 2$ of the systems with $\theta < 100''$ are likely to be random alignments. We conclude that the 36 pairs with $\theta < 100''$ are high-probability DWD candidates (13 are re-detections of previously known systems).

The likelihood of random alignments drops dramatically as μ becomes larger. We therefore also searched for pairs with $\mu > 80 \text{ mas yr}^{-1}$, requiring only that $\Sigma^2 < 10$. We identified an additional four pairs in this manner, bringing the total number of newly identified candidate common proper motion DWDs to 27.

4.2.2 Astrometrically Close Pairs

The population synthesis simulations described in Paper I predicted that the population of wide DWDs should have a minimum orbital separation of a few 10^2 AU. At typical distances to photometrically identified WDs, this corresponds to $\theta \approx 1''$, within the resolving limit of SDSS photometry. There should therefore be a substantial population of wide DWDs in SDSS with $\theta \leq 7''$, the minimum separation identifiable through proper motion matching to the USNO-B photometric plates. Can these pairs be identified through other means?

Dhital et al. (2015) search for photometrically resolved pairs of low-mass stars in SDSS with small θ . These authors identify >40,000 binaries with θ of 04–10'' and argue that wide pairs can be efficiently identified without having to match proper motions. Similarly, Baxter et al. (2014) identified a set of wide DWDs with $\theta \lesssim 30''$ in DR7 based exclusively on photometry.

To identify such pairs in DR9, we again started with the photometric catalog and extracted a sample of candidate WDs. Since μ measurements are generally unavailable for objects with nearby companions in SDSS, subdwarfs and QSOs are now significant sources of contamination. To reduce the contamination due to subdwarfs, we applied a more stringent color-color cut to our sample, selecting only those objects in the photometric catalog that fall in the Girven et al. (2011) DA WD region (cf. discussion in Paper I).

Girven et al. (2011) estimated that 17% of the objects falling within this color-color region are QSOs. However, this was based on a $g < 19$ mag sample of objects with SDSS spectra. Our sample extends to $g = 21$, and we expected QSOs to be a more significant

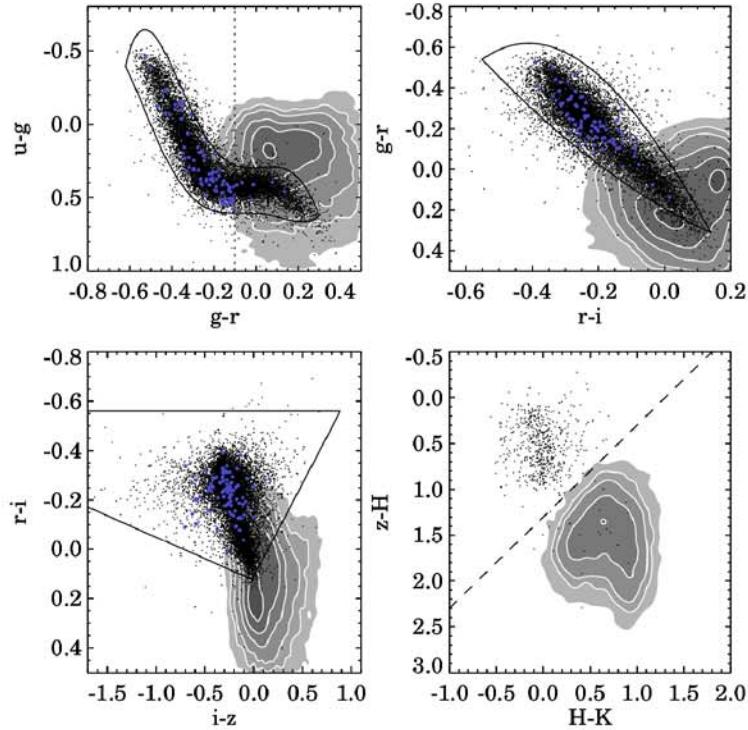


Figure 4.4 Distribution in color space of spectroscopically confirmed QSOs (contours) and WDs (black dots) from SDSS (Schneider et al. 2010; Kleinman et al. 2013). The Girven et al. (2011) WD regions are overplotted. Blue dots indicate WDs from the 43 candidate wide DWDs that pass the selection criteria described in Section 4.2.2. The objects in both SDSS catalogs with UKIDSS (Lawrence et al. 2007) counterparts are also plotted in $(z - H)$ versus $(H - K)$ in the bottom right panel. The dashed line in that panel is $(z - K) = 1.3$ mag. While this line cleanly separates WDs from QSOs, the majority of our candidate WDs lack UKIDSS counterparts. Using SDSS photometry alone, $(u - g)$ versus $(g - r)$ colors provide the best constraints to separate QSOs from WDs.

contaminant.

To determine the extent of the overlap between QSOs and WDs, we examined the distribution in $ugrizHK$ color space of spectroscopically confirmed SDSS QSOs (Schneider et al. 2010) and WDs (Kleinman et al. 2013). While QSOs and WDs can be cleanly separated using SDSS+infrared colors (see bottom right panel of Figure 4.4), the majority of the SDSS

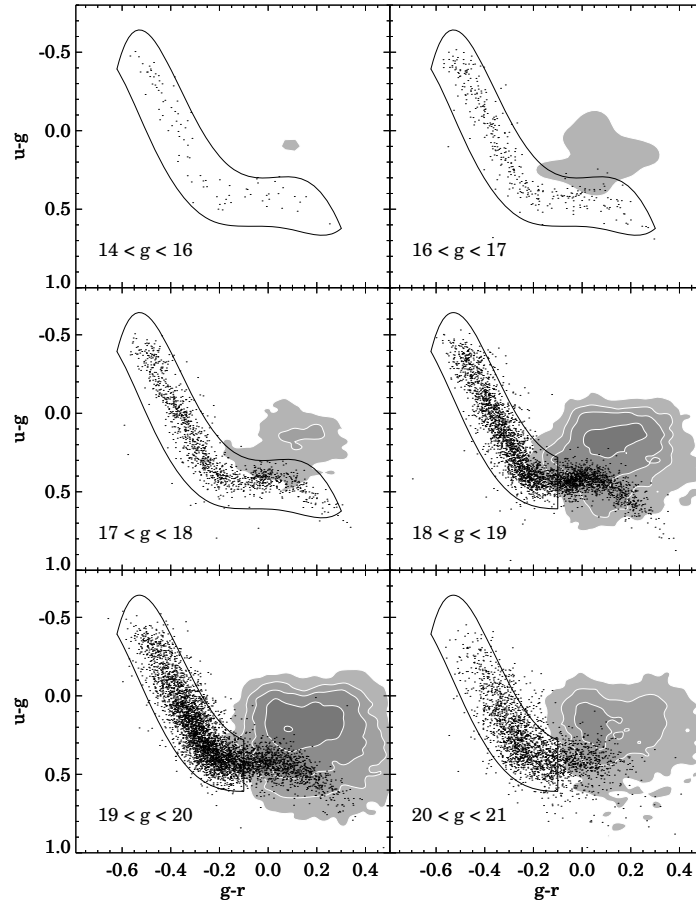


Figure 4.5 ($u - g$) versus ($g - r$) for photometrically identified candidate WDs binned by magnitude. The contours are the spectroscopically confirmed QSOs from the Schneider et al. (2010) catalog, while the solid line in the top two and middle left panels is the Girven et al. (2011) WD region. QSOs become a major source of contamination at fainter magnitudes and redder ($g - r$). To identify fainter candidate WDs, we therefore added the constraint that for $g > 18$ mag, $(g - r) < -0.1$, resulting in the regions described by the solid line in the middle right and bottom two panels.

photometric catalog lacks UKIDSS counterparts and infrared photometry.⁴

Of the *ugriz* color-color pairings, the least overlap between QSOs and WDs occurs

⁴The UKIRT Infrared Deep Sky Survey (UKIDSS) project is defined in Lawrence et al. (2007). UKIDSS uses the UKIRT Wide Field Camera (WFCAM; Casali et al. 2007). The photometric system is described in Hewett et al. (2006), and the calibration is described in Hodgkin et al. (2009). The pipeline processing and science archive are described in Hambly et al. (2008). We used the Eighth Data Release.

in $(u - g)$ versus $(g - r)$. The bottom panels of Figure 4.5 show that, in this color combination, the number of QSOs falling in the Girven et al. (2011) region increases at fainter magnitudes, but primarily at redder $(g - r)$. In addition to using the Girven et al. (2011) color-color regions to identify candidate WDs, for objects with $g > 18$ we added the additional requirement that $(u - g) < -0.1$. There are 67,640 objects in DR9 that satisfy these photometric constraints.

We searched for pairs of objects within this sample with $\theta < 2'$, removing pairs within crowded fields. Figure 4.6 is a histogram of the resulting θ distribution. For $\theta \gtrsim 20''$, the rate of matches increases linearly with θ , as expected for random alignments. We fit a line through the origin to the θ distribution for pairs with $\theta > 50''$. When extrapolating to smaller θ values, the line suggests that $\lesssim 5$ of the systems with $\theta < 10''$ are likely to be random alignments. Accordingly, we selected the 43 pairs with $\theta < 10''$ as high-confidence candidate DWDs. Five of these were previously known, so that we have 38 new candidate DWDs.

Among the previously known wide DWDs are the 11 systems identified in Paper I and 36 systems identified elsewhere in the literature. To that sample we add 27 systems identified by common proper motions and 38 identified by their small astrometric separations. Baxter et al. (2014) found 53 wide DWDs in SDSS and spectroscopically confirmed 26 of these (one additional pair was found to be a contaminant). Thirty of the 53 DWDs are new, and 11 of these are spectroscopically confirmed. In Table 4.2 we provide positions, g magnitudes, and μ_α and μ_δ , when available, for the combined catalog of 142 candidate and confirmed wide DWDs, including the 19 candidate and 11 spectroscopically confirmed

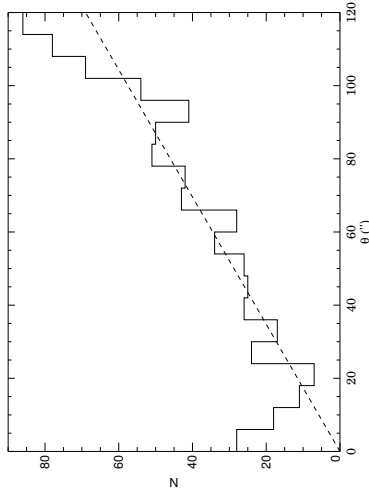


Figure 4.6 Angular separation distribution for astrometrically selected candidate DWDs. For $\theta \gtrsim 20''$, the number of matches increases linearly with θ , as expected for random alignments. The dashed line shows the best fit line to the distribution of random alignments beyond $50''$ where random alignments dominate, again assuming $N(\theta) \propto \theta$ and that the line goes through the origin. Extrapolating this fit to smaller θ shows that pairs with $\theta < 10''$ are excellent candidates for follow-up.

pairs from Baxter et al. (2014).

4.2.3 Comparison with Previous Samples

Figure 4.7 shows μ versus θ for our new DWDs, as well as for pairs from the literature, including the Baxter et al. (2014) DWDs. Our pairs are very different from those in the literature, and in particular from the DWDs identified by Baxter et al. (2014), despite similar source catalogs (SDSS DR9 here, DR7 for Baxter et al. 2014).

These differences are largely due to the search methods employed: Baxter et al. (2014) initially used a less restrictive color-color region to select photometric WD candidates. These authors then searched for candidate wide DWDs by finding nearby pairs of blue

objects without proper motion matching, similar to the astrometric approach described above. Compared to our candidates, these candidate DWDs have smaller θ and μ values. But the small overlap between the two samples argues for the value of both approaches.

We recover all of the new wide DWDs found in Paper I in this search. Another 21 wide DWDs from the literature fall within the SDSS DR9 footprint; we recover eight of these pairs. The reasons we fail to re-detect the other 13 DWDs are given in Table 4.1. Most are not recovered because one or both of the WDs are cool enough to have colors too red to fall within our WD photometric region. This suggests that our detection algorithm is insensitive to the wide DWDs that contain cooler WDs, but these WDs have such large τ_{cool} that they are less useful for constraining the IFMR than the hotter WDs we do find.

4.3 Assembling a Spectroscopic Sample

4.3.1 Observations and Reductions, and Spectra From the Literature

Identifying a large number of DWDs is only the first step toward constraining the IFMR. While the WDs' effective temperatures (T_{eff}) can be derived from SDSS photometry to within a few 100 K, typical SDSS photometric errors are large enough to create uncertainties $\gtrsim 0.5$ dex in the derived surface gravities ($\log g$). As a result, photometry alone is insufficient to determine the mass of a given WD with an accuracy better than $\approx 50\%$. Furthermore, without a precise mass (and therefore radius), τ_{cool} estimates must be based on T_{eff} alone and are uncertain by a factor of two or larger.

We therefore engaged in a campaign to obtain spectra for WDs in DWDs. Our targets

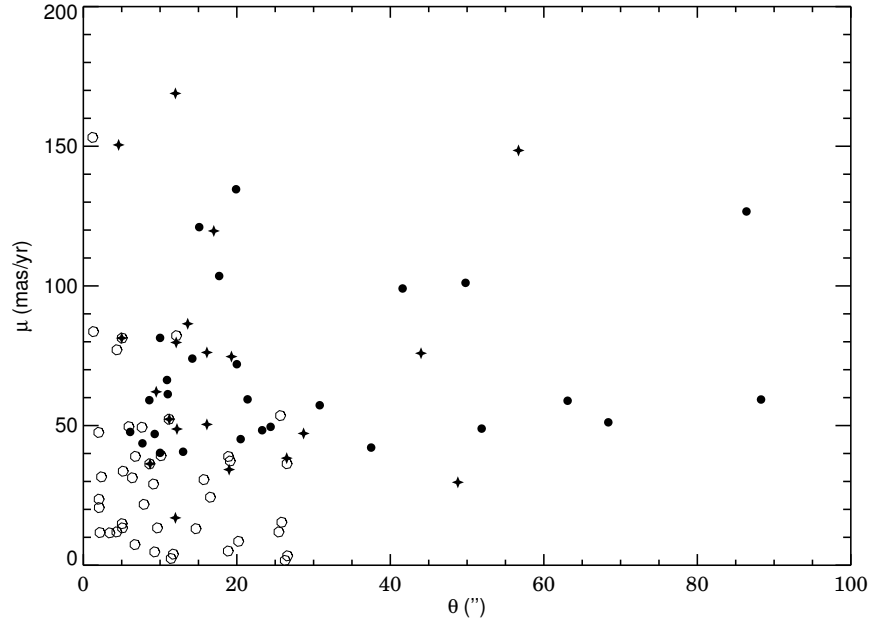


Figure 4.7 Total proper motion (μ) versus angular separation (θ) for candidate DWDs identified in our search for common proper motion pairs (filled circles), in Baxter et al. (2014, open circles), and in the literature (pluses). Although the Baxter et al. (2014) DWDs were also identified in SDSS, the overlap with our sample is small due to differences in the search techniques. Compared to other searches, we find systems with larger θ and μ .

included the new systems identified in Paper I, those photometrically selected from DR9, and WDs from pairs in the literature that lacked spectroscopy.⁵ Roughly 50 systems have $g \leq 19$ mag, making them ideal targets for the 3.5-m telescope at Apache Point Observatory (APO), NM.⁶

Over 13 half nights between 2012 Sep and 2013 Sep, we observed 34 pairs with the Dual Imaging Spectrograph in its high-resolution mode ($R \approx 2500$ at $H\beta$), which provides coverage from 3800 to 5000 Å on the blue CCD. The slit was rotated so that spectra were taken simultaneously of both candidate WDs in each pair. The spectra were therefore not

⁵The Baxter et al. (2014) systems were published too recently to be included in our spectroscopic campaign, although as we discuss below several of these DWDs were also in our sample.

⁶The APO 3.5-m telescope is owned and operated by the Astrophysical Research Consortium.

Table 4.1 DWDs in the DR9 Footprint not Recovered in this Search

System	Reason	$(u - g)$	$(g - r)$
LP 322-500A/B	A: low T_{eff}	0.97	0.35
LP 549-33/32	B: low T_{eff}	1.98	0.89
GD 322	B: low T_{eff}	0.81	0.35
LP 707-8/9	B: low T_{eff}	1.53	0.75
LP 701-69/70	B: low T_{eff}	2.26	0.98
LP 406-62/63	A: low T_{eff}	1.31	0.61
	B: low T_{eff}	1.72	0.83
LP 647-33/34	A: low T_{eff}	1.62	0.68
	B: low T_{eff}	1.65	0.76
LP 543-33/32	A: low T_{eff}	1.76	0.88
	B: low T_{eff}	2.08	1.07
LP 096-66/65	A: low T_{eff}	1.63	0.93
	B: low T_{eff}	1.13	0.53
LP 567-39/38	A: low T_{eff}	1.90	0.75
	B: low T_{eff}	0.96	0.48
G261-43	A: saturated		
J0926+1321	B: low μ^{a}		
GD 559	A,B: not stars ^b		

Note. – Objects with low T_{eff} have $(u - g)$ and $(g - r)$ colors outside our photometric selection region for WDs.

^a J0926+1321 was identified by Dobbie et al. (2012b) as a wide DWD based on these authors' μ calculations.

^b The SDSS pipeline classified both stars as galaxies.

obtained at the parallactic angle. Under ideal conditions, objects with separations as small as $2''$ could be distinguished for reduction.

Table 4.2: Wide Double White Dwarf – Observed Quantities

Name	α	δ	ξ (mag)	μ_α (mas yr ⁻¹)	μ_δ (mas yr ⁻¹)	θ ($''$)	Targeted for Spectroscopy	Source
J0000-0308	00:00:11.63	-03:08:31.88	20.11 ± 0.02	42.43 ± 3.25	-21.97 ± 3.25	6.1	N	1
	00:00:12.04	-03:08:31.34	20.01 ± 0.02	48.15 ± 3.25	-21.02 ± 3.25			
J0000-1051	00:00:22.53	-10:51:42.12	18.90 ± 0.01	45.26 ± 4.65	-23.81 ± 4.65	16.1	N	2
	00:00:22.83	-10:51:26.64	20.21 ± 0.02	42.37 ± 4.08	-23.57 ± 4.08			
CDD51	00:01:42.84	+25:15:06.1	17.79 ± 0.02			2.16	N	3
	00:01:42.79	+25:15:04.0	18.70 ± 0.16					
J0002+0733	00:02:15.33	+07:33:59.14	17.85 ± 0.01	-103.4 ± 2.77	-64.37 ± 2.77	15.1	Y	1
	00:02:16.13	+07:33:49.93	18.07 ± 0.01	-103.62 ± 2.85	-63.59 ± 2.85			
J0029+0015	00:29:25.29	+00:15:59.79	19.59 ± 0.01	-27.87 ± 3.62	-23.24 ± 3.62	8.7	N	2,3
	00:29:25.62	+00:15:52.72	18.46 ± 0.01	-28.33 ± 3.13	-22.58 ± 3.13			
J0030+1810	00:30:51.75	+18:10:53.75	18.72 ± 0.01			7.8	Y	1
	00:30:51.80	+18:10:46.05	18.73 ± 0.01					
CDD53	00:52:12.26	+13:53:02.0	17.71 ± 0.03			6.78	N	3
	00:52:12.73	+13:53:01.1	18.89 ± 0.03					
LP 406-62/63	01:04:56.33	+21:19:54.9	18.30 ± 0.02	-210.33 ± 2.51	-431.2 ± 2.51	28	N	4
	01:04:57.81	+21:20:13.49	18.59 ± 0.02	-209.48 ± 2.62	-436.89 ± 2.62			
J0105-0741	01:05:53.78	-07:41:22.19	20.51 ± 0.03	-47.73 ± 4.65	-66.24 ± 4.65	10	N	1
	01:05:54.14	-07:41:30.84	18.57 ± 0.01	-48.41 ± 2.57	-61.63 ± 2.57			
J0107+0511	01:07:17.20	+05:11:46.78	18.67 ± 0.01	-59.61 ± 2.86	-79.32 ± 2.86	41.6	N	1
	01:07:19.89	+05:11:58.09	20.54 ± 0.02	-49.86 ± 3.48	-73.05 ± 3.48			
LP707-8/9	01:09:03.42	-10:42:14.17	16.77 ± 0.03	169.41 ± 2.65	-28.7 ± 2.65	12	N	4
	01:09:04.23	-10:42:15.45	19.45 ± 0.04	170.79 ± 3.5	-25.88 ± 3.5			
J0117+2440	01:17:14.13	+24:40:20.31	19.84 ± 0.01			5	N	1,3
	01:17:14.49	+24:40:21.46	19.62 ± 0.01					
LP647-33/34	01:17:28.67	-04:39:40.84	18.52 ± 0.04			2	N	4
	01:17:28.48	-04:39:42.12	18.68 ± 0.03					
CDD55	01:27:26.89	+39:15:03.3	18.70 ± 0.02			16.55	N	3
	01:27:25.51	+39:14:59.2	19.99 ± 0.02					
J0133+3011	01:33:10.11	+30:11:53.7	19.19 ± 0.01			7.7	N	1
	01:33:10.69	+30:11:52.61	19.68 ± 0.02					

Continued on next page

Table 4.2 – Continued from previous page

Name	α	δ	δ (mag)	μ_α (mas yr $^{-1}$)	μ_δ (mas yr $^{-1}$)	θ ($''$)	Targeted for Spectroscopy	Source ^a
J0136+3048	01:36:32.28	+30:48:14.97	20.14 \pm 0.03			3	N	1
	01:36:32.46	+30:48:16.73	20.07 \pm 0.02					
J0138+5559	01:38:19.05	+55:59:40.55	19.70 \pm 0.01	15.99 \pm 4.79	-65.7 \pm 4.79	10.9	N	1
	01:38:19.96	+55:59:32.99	19.68 \pm 0.01	21.28 \pm 3.38	-60.16 \pm 3.38			
J0139+1447	01:39:10.70	+14:47:26.51	19.55 \pm 0.01	-19.82 \pm 3.62	-47.44 \pm 3.62	68.4	N	1
	01:39:11.01	+14:48:34.91	19.64 \pm 0.01	-22.61 \pm 5	-40.87 \pm 5			
J0211+1714	02:11:31.51	+17:14:30.44	17.20 \pm 0.01			2.1	N	1,3
	02:11:31.52	+17:14:28.31	16.76 \pm 0.01					
LP 197-5/6	02:25:51.96	+42:28:04.3				7	N	4
	02:25:52.59	+42:28:05.56						
CDDS7	02:27:33.09	+00:52:00.3	19.62 \pm 0.02			6.72	N	3
	02:27:33.15	+00:51:53.6	19.86 \pm 0.02					
J0304+4541	03:04:29.38	+45:41:48.15	20.09 \pm 0.02			6.5	N	1
	03:04:30.00	+45:41:47.83	19.41 \pm 0.01					
J0316+0319	03:16:29.61	+03:18:58.03	20.28 \pm 0.02	-15.31 \pm 4.66	-42.48 \pm 4.66	20.5	N	1
	03:16:30.93	+03:19:04.36	18.14 \pm 0.01	-12.62 \pm 2.65	-35.44 \pm 2.65			
RE J0317-853	03:17:16.18	-85:32:25.45				7	N	4
	03:17:19.31	-85:32:31.15						
LP 472-70/69	03:25:38.33	+15:09:00.89				3	N	4
	03:25:36	+15:08.5						
J0332-0049	03:32:36.59	-00:49:18.42		-24.79 \pm 5.39	-23.63 \pm 5.39	19	N	2,3
	03:32:36.86	-00:49:36.93		-30.91 \pm 4.48	-23.31 \pm 4.48			
J0344+1510	03:44:10.91	+15:10:22.08	16.52 \pm 0.01	21.42 \pm 2.53	-36.7 \pm 2.53	37.5	Y	1
	03:44:11.49	+15:09:45.71	16.89 \pm 0.01	23.79 \pm 2.56	-40.62 \pm 2.56			
HS 0507+0434	05:10:13.52	+04:38:55.2				18	N	4
	05:10:14.0	+04:38:41						
LMC 102.7.22886(769)	05:18:51.10	-68:11:17.7				96.3	N	4
	05:18:54.98	-68:09:48.3						
CDDS9	05:45:19.81	+30:27:54.0	19.82 \pm 0.02			11.72	N	3
	05:45:18.98	+30:27:49.3	19.64 \pm 0.02					

Continued on next page

Table 4.2 – Continued from previous page

Name	α	δ	δ (mag)	μ_α (mas yr $^{-1}$)	μ_δ (mas yr $^{-1}$)	θ ($''$)	Targeted for Spectroscopy	Source a
CDD510	07:21:47.38	+32:28:24.1	18.07 \pm 0.01			2.77	N	3
	07:21:47.20	+32:28:22.4	18.32 \pm 0.06					
J0729+6519	07:29:19.15	+65:19:10.88	20.88 \pm 0.03	0	0	9.1	N	1
	07:29:20.61	+65:19:10.34	20.79 \pm 0.02	0	0			
WD0727+482A/B	07:30:42.80	+48:12:00.0					N	4
	07:30:47.36	+48:10:27.6						
J0748+3025	07:48:52.96	+30:25:43.42	17.73 \pm 0.01			1.5	N	1,3
	07:48:53.08	+30:25:43.57	17.41 \pm 0.01					
LP543-33/32	07:50:15.42	+07:11:26.64	17.20 \pm 0.02	209.72 \pm 2.53	-1787.91 \pm 2.53	16	N	4
	07:50:14.67	+07:11:38.5	17.64 \pm 0.02	208.92 \pm 2.59	-1783.09 \pm 2.59			
J0754+1239	07:54:10.53	+12:39:47.41	18.73 \pm 0.01	0	0	2	Y	1,3
	07:54:10.58	+12:39:45.53	18.83 \pm 0.01	0	0			
J0754+4950	07:54:20.88	+49:50:05.28	20.61 \pm 0.03	-16.59 \pm 5.41	-60.3 \pm 5.41	11	N	1
	07:54:21.11	+49:50:16.43	19.46 \pm 0.01	-23.46 \pm 3.54	-64.35 \pm 3.54			
CDD513	08:02:12.54	+24:20:43.6	19.54 \pm 0.02			25.85	N	3
	08:02:13.44	+24:20:20.9	19.84 \pm 0.02					
CDD514	08:06:44.09	+44:45:03.2	18.14 \pm 0.02			5.09	N	3
	08:06:43.64	+44:45:01.4	18.74 \pm 0.02					
J0827-0216	08:27:30.57	-02:16:20.16	17.83 \pm 0.01			2.7	Y	1
	08:27:30.72	-02:16:18.54	17.99 \pm 0.01					
LP 035-288/287	08:46:01.07	+69:44:38.85				3	N	4
	08:46:01.21	+69:44:37.5						
J0849+4712	08:49:52.46	+47:12:47.73	17.70 \pm 0.01			4.4	Y	1,3
	08:49:52.87	+47:12:49.46	16.71 \pm 0.01	-53.95 \pm 2.64	-67.86 \pm 2.64			
J0859+3306	08:59:15.02	+33:06:44.67	18.00 \pm 0.01			9.3	Y	1,3
	08:59:15.50	+33:06:37.62	18.69 \pm 0.01					
CDD517	08:59:17.36	+42:50:31.6	18.94 \pm 0.05			4.39	N	3
	08:59:17.23	+42:50:27.4	18.38 \pm 0.04					
PG 0901+140	09:04:02.78	+13:49:14.84	16.10 \pm 0.00			3.7	Y	4
	09:04:02.80	+13:49:11.13	16.73 \pm 0.00					

Continued on next page

Table 4.2 – Continued from previous page

Name	α	δ	δ (mag)	μ_α (mas yr ⁻¹)	μ_δ (mas yr ⁻¹)	θ ($''$)	Targeted for Spectroscopy	Source ^a
PG 0922+162	09:25:13.17 09:25:13.48	+16:01:45.4 +16:01:44.14	17.12 ± 0.01 16.12 ± 0.01			4.5	N	1,3
J0926+1321	09:26:46.88 09:26:47.00	+13:21:34.5 +13:21:38.4	18.37 ± 0.15 18.45 ± 0.04	-49.11 ± 3.9 11.41 ± 2.69	-142.69 ± 3.9 -4.36 ± 2.69	4.6	N	4,3
LP 462-56A/B	09:37:00.0 09:37:00.0	-37:21:33 -37:21:33				4	N	4
LP 370-50/51	09:45:07.92 09:45:08.63	+23:27:23.03 +23:27:31.32	17.50 ± 0.01 17.70 ± 0.01	-191.34 ± 2.42 -189.29 ± 2.44	-101.41 ± 2.42 -100.68 ± 2.44	13.2	Y	4
CDDS20	09:54:58.73 09:54:59.97	+39:01:04.6 +39:00:52.4	19.86 ± 0.02 17.69 ± 0.02			18.87	N	3
J1002+3606	10:02:44.87 10:02:45.83	+36:06:29.51 +36:06:53.28	18.89 ± 0.01 19.01 ± 0.01	-32.72 ± 3.29 -29.64 ± 3.44	-27.77 ± 3.29 -27.35 ± 3.44	26.5	Y	2,3
LP 549-33/32	10:15:02.60 10:15:01.73	+08:06:35.7 +08:06:11.5	16.19 ± 0.02 18.35 ± 0.02	-288 ± 2.66 -291.59 ± 3.03	164.96 ± 2.66 155.47 ± 3.03	26	Y	4
PG 1017+125	10:19:55.9 10:19:54.6	+12:16:31.48 +12:17:17.98	15.51 ± 0.03 16.75 ± 0.03	-24.14 ± 2.42 -27.02 ± 2.48	-18.03 ± 2.42 -23.99 ± 2.48	48.8	Y	4
J1048+0148	10:48:18.59 10:48:18.64	+01:48:41.77 +01:48:44.34	19.76 ± 0.02 19.69 ± 0.01			2.7	N	1
CDDS22	10:53:06.13 10:53:06.82	+02:50:52.5 +02:50:27.9	19.14 ± 0.02 18.98 ± 0.02			26.60	N	3
LP 128-254/255	10:54:49.1 10:54:49.88	+53:07:15.51 +53:07:59.43	17.51 ± 0.02 17.90 ± 0.02	-112.5 ± 2.95 -113.57 ± 3.1	-34.56 ± 2.95 -37.02 ± 3.1	44	Y	4
J1110+4517	11:10:16.79 11:10:20.88	+45:17:36.23 +45:18:01.79	17.67 ± 0.01 16.80 ± 0.01	26.63 ± 2.87 26.89 ± 3.61	-45.18 ± 2.87 -46.32 ± 3.61	51.9	Y	1
J1113+3238	11:13:19.43 11:13:22.56	+32:38:17.88 +32:38:58.92	19.03 ± 0.01 19.11 ± 0.01	-162.09 ± 3.15 -158.09 ± 3.17	58.49 ± 3.15 58.36 ± 3.17	56.7	N	2
J1127+2725	11:27:30.96 11:27:31.68	+27:25:42.95 +27:25:40.8	20.81 ± 0.03 17.86 ± 0.01			8.6	N	1
ESO 439-162/163	11:29:52.04 11:29:53.79	-31:22:47.23 -31:22:42.61				23	N	4

Continued on next page

Table 4.2 – Continued from previous page

Name	α	δ	δ (mag)	μ_α (mas yr ⁻¹)	μ_δ (mas yr ⁻¹)	θ ($''$)	Targeted for Spectroscopy	Source ^a
J1130+2103	11:30:32.97	+21:03:59.21	20.56 ± 0.03			2.8	N	1
	11:30:33.14	+21:03:57.99	20.29 ± 0.02					
CDDS23	11:39:28.52	-00:14:20.9	19.42 ± 0.02			2.95	N	3
	11:39:28.47	-00:14:18.0	19.80 ± 0.06					
CDDS24	11:50:30.12	+25:32:10.1	19.95 ± 0.02			6.38	N	3
	11:50:30.48	+25:32:06.0	18.86 ± 0.02					
CDDS25	11:53:05.54	+00:56:46.1	18.89 ± 0.02			1.22	N	3
	11:53:05.47	+00:56:45.8	18.91 ± 0.02					
CDDS26	11:59:37.81	+13:44:13.9	18.07 ± 0.02			5.18	N	3
	11:59:37.82	+13:44:08.7	18.28 ± 0.02					
J1203+4948	12:03:11.03	+49:48:50.76	17.33 ± 0.01	-97.34 ± 2.86	-40.44 ± 2.86	19.3	Y	2
	12:03:11.52	+49:48:32.39	19.01 ± 0.01	-96.7 ± 3.46	-37.92 ± 3.46			
CDDS27	12:27:39.16	+66:12:24.4	17.86 ± 0.02			11.43	N	3
	12:27:41.05	+66:12:24.3	17.99 ± 0.02					
J1230+4734	12:30:21.81	+47:34:10.84	20.13 ± 0.02			4.2	N	1
	12:30:21.84	+47:34:06.63	19.90 ± 0.02					
J1231+5736	12:31:55.72	+57:36:11.37	17.83 ± 0.01			3.2	Y	1
	12:31:56.06	+57:36:09.75	18.53 ± 0.01					
J1254+0218	12:54:58.07	-02:18:37.8	16.46 ± 0.01	-12.57 ± 2.92	-55.89 ± 2.92	30.8	N	1
	12:54:58.55	-02:18:07.74	19.84 ± 0.02	-6.96 ± 4.04	-57.33 ± 4.04			
J1257+1925	12:57:20.87	+19:25:03.71	19.86 ± 0.02	-39.68 ± 5.39	-31.27 ± 5.39	12.2	N	2
	12:57:21.12	+19:24:51.84	17.02 ± 0.01	-33.93 ± 2.74	-33.29 ± 2.74			
GD 322	13:00:35.20	+59:04:15.6	15.24 ± 0.01	39.86 ± 2.62	73.37 ± 2.62	16.1	N	4
	13:00:33.46	+59:04:06.9	18.27 ± 0.01	39.1 ± 3.03	72.26 ± 3.03			
J1304+0917	13:04:07.67	+09:17:22.84	20.43 ± 0.03	-48.29 ± 3.63	8.04 ± 3.63	23.3	N	1
	13:04:08.64	+09:17:41.1	19.99 ± 0.02	-49.11 ± 3.48	6.89 ± 3.48			
LP 322-500A/B	13:04:29.42	+30:59:00.39	18.58 ± 0.03	-0.36 ± 3.11	-16.95 ± 3.11	12	N	4
	13:04:30.31	+30:58:55.08	20.30 ± 0.04	2.69 ± 5.42	-25.1 ± 5.42			
J1306+5925	13:06:04.55	+59:25:09.47	19.75 ± 0.01	-0.94 ± 3.73	-58.89 ± 3.73	63.1	N	1
	13:06:06.71	+59:26:10.31	17.51 ± 0.01	3.34 ± 2.81	-62.99 ± 2.81			

Continued on next page

Table 4.2 – Continued from previous page

Name	α	δ	δ (mag)	μ_α (mas yr ⁻¹)	μ_δ (mas yr ⁻¹)	θ ($''$)	Targeted for Spectroscopy	Source ^a
J1309+5503	13:09:54.23	+55:03:39.23	18.64 ± 0.01	52.11 ± 3.18	-27.57 ± 3.18	13	N	1
	13:09:55.67	+55:03:38.51	17.96 ± 0.01	51.32 ± 2.89	-29.21 ± 2.89			
CDDS28	13:10:12.28	+44:47:28.3	17.84 ± 0.02			15.71		3
	13:10:13.38	+44:47:17.8	17.59 ± 0.02					
LP 096-66/65	13:10:20.68	+61:17:49.4	20.86 ± 0.03			18	N	4
	13:10:22.01	+61:18:04.67	19.62 ± 0.02	-295.89 ± 3.78	37.62 ± 3.78			
J1311+1543	13:11:21.60	+15:43:04.79	19.97 ± 0.02	-39.75 ± 4.99	-12.45 ± 4.99	10	N	1
	13:11:21.84	+15:42:56.52	19.89 ± 0.02	-39.74 ± 3.5	-10.71 ± 3.5			
J1313+2030	13:13:32.13	+20:30:39.63	17.79 ± 0.01			5.9	Y	1,3
	13:13:32.56	+20:30:39.42	17.47 ± 0.01	-32.15 ± 4.64	24.69 ± 4.64			
CDDS30	13:14:21.70	+30:50:51.4	18.20 ± 0.08			2.76	N	3
	13:14:21.50	+30:50:50.5	17.86 ± 0.04					
J1314+1732	13:14:26.40	+17:32:27.96	18.65 ± 0.01	-40.58 ± 2.79	-60.69 ± 2.79	20	Y	1
	13:14:26.88	+17:32:09.24	16.24 ± 0.01	-39.92 ± 2.33	-59.62 ± 2.33			
CDDS31	13:28:14.28	+16:31:51.5	16.27 ± 0.02			1.32	N	3
	13:28:14.36	+16:31:50.9	17.65 ± 0.23					
J1342+5938	13:42:45.86	+59:38:31.37	19.53 ± 0.01			2.2	N	1
	13:42:46.12	+59:38:30.69	19.80 ± 0.02					
J1347+2512	13:47:37.68	+25:12:33.11	19.36 ± 0.01	-61.68 ± 3.24	-20.32 ± 3.24	21.4	N	1
	13:47:39.12	+25:12:28.79	20.22 ± 0.02	-63.02 ± 3.54	-17.65 ± 3.54			
CDDS32	13:57:13.14	-06:59:13.7	19.25 ± 0.02			26.29	N	3
	13:57:14.50	-06:58:56.9	18.16 ± 0.02					
J1412+4216	14:12:07.68	+42:16:27.12	15.82 ± 0.01	-81.41 ± 2.66	-62 ± 2.66	13.6	Y	2
	14:12:08.87	+42:16:24.59	18.45 ± 0.01	-80 ± 3.11	-58.14 ± 3.11			
J1424-0317	14:24:22.32	-03:17:43.33	19.15 ± 0.01	-126.39 ± 3.53	10.98 ± 3.53	86.4	N	1
	14:24:28.07	-03:17:47.54	19.38 ± 0.01	-121.09 ± 3.86	2.74 ± 3.86			
J1432+0136	14:32:59.99	+01:36:36.03	20.75 ± 0.03	-57.68 ± 5.83	-14.02 ± 5.83	88.3	N	1
	14:33:05.75	+01:36:26.82	21.23 ± 0.05	-59.53 ± 5.97	-11.54 ± 5.97			
L 151-81A/B	14:58:06	-63:17.1				2	N	4
	14:58:06	-63:17.1						

Continued on next page

Table 4.2 – Continued from previous page

Name	α	δ	δ (mag)	μ_α (mas yr ⁻¹)	μ_δ (mas yr ⁻¹)	θ ($''$)	Targeted for Spectroscopy	Source ^a
J1507+5210	15:07:46.48	+52:10:02.13	16.92 ± 0.01			5	N	3,4
	15:07:46.79	+52:09:58.06	17.77 ± 0.01					
J1515+1436	15:15:07.92	+14:36:35.45	19.61 ± 0.01			7.9	N	1,3
	15:15:08.30	+14:36:40.89	17.97 ± 0.01	2.94 ± 2.69	-21.59 ± 2.69			
J1544+2344	15:44:03.12	+23:44:58.92	18.42 ± 0.01	109.51 ± 2.98	-25.95 ± 2.98	17.7	N	1
	15:44:03.35	+23:45:16.55	19.64 ± 0.01	104.42 ± 3.51	-32.08 ± 3.51		N	
J1546+6159	15:46:41.49	+61:59:01.57	18.62 ± 0.01			7.7	Y	1,3
	15:46:41.80	+61:58:54.19	16.86 ± 0.01	15.49 ± 2.43	-27.45 ± 2.43			
J1552+4731	15:52:44.40	+47:31:24.06	18.96 ± 0.01			9.7	Y	1,3
	15:52:45.19	+47:31:29.53	18.71 ± 0.01	-8.85 ± 3.47	-11.95 ± 3.47			
CDDS37	16:26:50.11	+48:28:27.9	19.62 ± 0.02			20.22	N	3
	16:26:52.12	+48:28:24.7	18.98 ± 0.01					
CDDS38	16:36:47.81	+09:27:15.7	17.72 ± 0.01			10.12	N	3
	16:36:47.33	+09:27:08.4	19.54 ± 0.02					
CDDS39	16:57:37.90	+62:01:02.1	18.65 ± 0.01			25.47	N	3
	16:57:34.39	+62:00:55.9	18.53 ± 0.01					
J1703+3304	17:03:55.92	+33:04:38.28	18.81 ± 0.01	0.14 ± 3.4	-52.27 ± 3.4	11.2	N	2,3
	17:03:56.87	+33:04:35.75	18.13 ± 0.01	2.46 ± 3.14	-51.45 ± 3.14			
Gr 576/577	17:05:30.45	+48:03:12.02	14.43 ± 0.01			5.7	Y	4
	17:05:30.98	+48:03:09.93	14.40 ± 0.01					
LP 567-39/38	17:28:30.65	+07:21:12.57	19.02 ± 0.12			2	N	4
	17:28:30.78	+07:21:13.42	18.38 ± 0.02	-62.21 ± 2.47	-286.81 ± 2.47			
CDDS41	17:32:49.57	+56:39:00.0	18.95 ± 0.02			2.36	N	3
	17:32:49.32	+56:38:58.8	19.12 ± 0.05					
CDDS42	17:55:59.57	+48:43:59.9	19.21 ± 0.02			16.41	N	3
	17:55:58.35	+48:43:48.8	17.68 ± 0.01					
G 206-17/18	18:13:31.24	+32:48:31.7				55	N	4
	18:13:35.46	+32:48:43.7						
G 021-15	18:27:13.08	+04:03:46.7				58.6	N	4

Continued on next page

Table 4.2 – Continued from previous page

Name	α	δ	δ (mag)	μ_α (mas yr ⁻¹)	μ_δ (mas yr ⁻¹)	θ ($''$)	Targeted for Spectroscopy	Source ^a
J1848+6415	18:48:09.57	+64:15:20.08	19.78 ± 0.01	16.94 ± 4.95	-18.28 ± 4.95	2.2	N	1
	18:48:09.69	+64:15:17.96	19.26 ± 0.01				N	
CDDS43	20:43:18.96	+00:58:41.8	18.24 ± 0.02			19.13	N	3
	20:43:17.93	+00:58:30.5	18.59 ± 0.02					
J2044+4030	20:44:00.72	+40:30:06.01	17.86 ± 0.01	18.78 ± 2.54	46.88 ± 2.54	9.1	Y	1
	20:44:01.03	+40:30:14.39	15.32 ± 0.01					
J2047+0021	20:47:11.28	+00:21:27.35	17.06 ± 0.01	-6.24 ± 2.51	-100.91 ± 2.51	49.8	N	1
	20:47:13.68	+00:22:03.6	18.21 ± 0.01	-8.64 ± 2.8	-95.31 ± 2.8			
J2054+0640	20:54:33.50	+06:40:30.97	20.13 ± 0.02			5	N	1
	20:54:33.62	+06:40:26.23	20.10 ± 0.02					
GD 392	21:00:21.51	+34:26:21.0				45.8	N	4
	21:00:25.17	+34:26:10.81						
J2102+1029	21:02:57.74	+10:29:53.77	19.71 ± 0.01			3.3	N	1
	21:02:57.83	+10:29:50.85	20.12 ± 0.02					
J2106+0211	21:06:43.92	+02:11:54.58	20.39 ± 0.02	13.49 ± 2.99	7.8 ± 2.99	4.1	N	1
	21:06:44.11	+02:11:57.26	19.85 ± 0.01					
J2109+1809	21:09:25.46	+18:09:27.86	19.45 ± 0.01			2.3	N	1
	21:09:25.51	+18:09:30.13	20.59 ± 0.02					
J2115-0741	21:15:07.43	-07:41:51.54	17.44 ± 0.01	-25.33 ± 2.86	-117 ± 2.86	17	N	2
	21:15:07.43	-07:41:34.51	16.78 ± 0.01	-30.12 ± 2.78	-117.74 ± 2.78			
CDDS44	21:16:07.27	+00:45:03.1	18.67 ± 0.01			2.06	N	3
	21:16:07.20	+00:45:01.3	18.96 ± 0.07					
J2124-1620	21:24:32.52	-16:20:21.94	16.12 ± 0.01			8.3	Y	1
	21:24:32.59	-16:20:13.66	17.71 ± 0.01	-28.44 ± 2.45	-13.8 ± 2.45			
G 261-43	21:26:57.69	+73:38:43.6	13.96 ± 0.01	53.42 ± 2.55	-288.79 ± 2.55	1.4	N	4
CDDS45	21:36:48.79	+06:43:20.2	17.94 ± 0.02			3.44	N	3
	21:36:48.98	+06:43:18.2	19.35 ± 0.02					
CDDS46	21:44:56.12	+48:23:52.9	18.74 ± 0.01			14.67	N	3
	21:44:57.39	+48:23:45.5	19.49 ± 0.02					

Continued on next page

Table 4.2 – Continued from previous page

Name	α	δ	δ (mag)	μ_α (mas yr ⁻¹)	μ_δ (mas yr ⁻¹)	θ ($''$)	Targeted for Spectroscopy	Source ^a
CDDS47	21:53:09.89	+46:19:02.7	17.72 ± 0.01			25.68	N	3
	21:53:08.90	+46:18:39.1	19.08 ± 0.01					
J2155+0315	21:55:34.75	+03:15:39	19.32 ± 0.01			3.1	N	1
	21:55:34.94	+03:15:40.32	19.15 ± 0.01					
J2222-0828	22:22:36.31	-08:28:07.96	16.38 ± 0.01			4.3	Y	1,3
	22:22:36.55	-08:28:06	17.07 ± 0.01					
J2223+2201	22:23:01.60	+22:01:31.36	15.59 ± 0.01			6.6	N	1,3
	22:23:01.72	+22:01:24.95	16.00 ± 0.01					
J2224+2315	22:24:26.92	+23:15:36.03	17.83 ± 0.01			2.7	Y	1,3
	22:24:27.09	+23:15:37.47	17.16 ± 0.01					
J2227-0713	22:27:27.81	-07:13:03.3	18.87 ± 0.01			4.5	N	1
	22:27:28.05	-07:13:05.97	19.19 ± 0.01	13.74 ± 2.71	-14.34 ± 2.71			
SSSPM J2231-7514	22:30:96.61	-75:13:49.36				93	N	4
	22:30:33.14	-75:15:18.43						
J2236+2928	22:36:02.87	+29:28:51.34	18.48 ± 0.01			9.9	N	1
	22:36:03.48	+29:28:45.08	20.08 ± 0.02	7.74 ± 3.25	0.99 ± 3.25			
HS 2240+1234	22:42:30.23	+12:50:02.39	16.47 ± 0.01	-33.86 ± 2.76	-72.6 ± 2.76	12.1	N	3,4
	22:42:31.19	+12:50:04.91	16.19 ± 0.01	-32.17 ± 2.73	-75.96 ± 2.73			
J2259+1404	22:59:32.20	+14:04:39.28	16.35 ± 0.01			9.1	Y	1,3
	22:59:32.73	+14:04:44.25	18.58 ± 0.01	26.63 ± 3.25	-13.33 ± 3.25			
J2302+2430	23:02:49.43	+24:30:28.07	18.16 ± 0.01	-48.66 ± 2.81	-127.1 ± 2.81	19.9	N	1
	23:02:50.40	+24:30:13.67	18.49 ± 0.01	-51.55 ± 3	-126.52 ± 3			
J2303-0755	23:03:27.83	-07:55:04.72	18.14 ± 0.01	43.59 ± 2.54	6.37 ± 2.54	7.7	Y	1
	23:03:28.08	-07:54:57.88	18.16 ± 0.01	42.87 ± 2.57	9.42 ± 2.57			
LP 701-69/70	23:04:19.09	-07:01:26.71	17.19 ± 0.02	238.95 ± 2.3	-224.63 ± 2.3	26	N	4
	23:04:19.65	-07:01:52.03	19.98 ± 0.03					
J2317+5550	23:17:57.26	+55:50:34.58	18.72 ± 0.01			8.7	N	1
	23:17:57.59	+55:50:26.26	15.27 ± 0.01	11.48 ± 2.49	10.83 ± 2.49			
J2319+3426	23:19:41.35	+34:26:14.24	17.24 ± 0.01			5.1	Y	1
	23:19:41.44	+34:26:09.31	17.57 ± 0.01	-40.89 ± 5.85	-78.44 ± 5.85			

Continued on next page

Table 4.2 – Continued from previous page

Name	α	δ	δ (mag)	μ_α (mas yr ⁻¹)	μ_δ (mas yr ⁻¹)	θ ($''$)	Targeted for Spectroscopy	Source ^a
GD 559	23:21:17.28	+69:26:22.52	15.14 ± 0.04	-132.02 ± 2.73	-8.32 ± 2.73	28.7	Y	4
	23:21:17.24	+69:25:53.8	18.23 ± 0.04	-133.94 ± 3.07	-5.89 ± 3.07			
J2326-0023	23:26:58.79	-00:23:39.98	19.36 ± 0.01	53.95 ± 3.22	-30.73 ± 3.22	9.5	N	2
	23:26:59.27	-00:23:48.1	17.51 ± 0.01	55.15 ± 2.67	-28.99 ± 2.67			
J2332+4917	23:32:46.24	+49:17:09.13	18.76 ± 0.01			3	N	1,3
	23:32:46.27	+49:17:12.08	18.67 ± 0.01					
J2337+2123	23:37:06.24	+21:23:23.28	18.66 ± 0.01	70.57 ± 2.79	33.98 ± 2.79	14.2	N	1
	23:37:07.19	+21:23:20.75	19.67 ± 0.01	75.8 ± 3.19	31.53 ± 3.19			
J2345+3507	23:45:26.40	+35:07:53.75	20.22 ± 0.03	-36.88 ± 4.09	-36.03 ± 4.09	9.3	N	1
	23:45:26.88	+35:07:46.91	17.57 ± 0.01	-38.49 ± 2.38	-36.27 ± 2.38			
LP 077-57/56	23:54:07.98	+65:22:34.01				3	N	4
	23:54:07.71	+65:22:31.48						
J2355+1708	23:55:15.36	+17:08:06.72	18.23 ± 0.01	51.75 ± 2.69	2.94 ± 2.69	24.4	Y	1
	23:55:15.36	+17:08:30.83	16.22 ± 0.01	53.01 ± 2.33	4.36 ± 2.33			

References. – 1–This work, 2–Paper I, 3–Baxter et al. (2014), 4–Literature, see Paper I for references

Note. – The WDs in each pair are ordered by RA, regardless of the “A” or “B” designation that may exist in the literature.

All the spectra were trimmed, bias-corrected, cleaned of cosmic rays, flat-fielded, extracted, and dispersion-corrected using standard IRAF tasks.⁸ The spectra were flux calibrated using bright WD spectrophotometric standards in the IRAF database. To improve the final signal-to-noise ratio (S/N), spectra were co-added using the IRAF routine `scombine`. Occasionally, the spectra to be combined were taken at different epochs, but the observing setup was identical across all observations.

Wide DWDs identified in Paper I, as well as a few WDs from our photometric search in DR9, have at least one SDSS spectrum ($R \approx 1800$), and we add these ≈ 30 SDSS spectra to our sample. Additionally, high-resolution Very Large Telescope (VLT; $R \approx 15,000$) spectra for ≈ 10 WDs from the Supernova Progenitor Survey (Koester et al. 2009) were provided by D. Koester (priv. communication). In total, we have 114 spectra for 97 WDs in wide DWDs; see Figure 4.8 for sample spectra. The contamination by non-WDs is extremely low: only one of the 97 objects for which we obtained spectra is not a WD (J2124–1620A is an A star).

4.3.2 Atmospheric Model Fits to Our Spectra

To obtain T_{eff} and $\log g$ for these WDs, we used the spectroscopic technique developed by Bergeron et al. (1992) and described in Gianninas et al. (2011, and references therein), which incorporates model atmospheres for WDs with $6.5 \leq \log g \leq 9.5$. The observed and theoretical spectra are normalized to a continuum set to unity, and the observed $H\beta$ to $H8$ lines are fit simultaneously to the synthetic spectra (see Figure 4.9). The uncertainties in

⁸IRAF is distributed by the National Optical Astronomy Observatories, which are operated by the Association of Universities for Research in Astronomy, Inc., under cooperative agreement with the National Science Foundation.

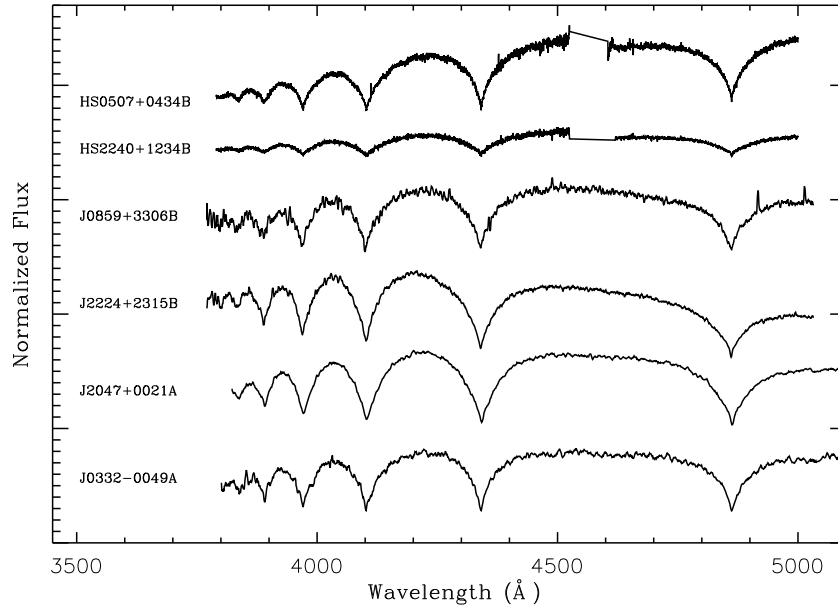


Figure 4.8 Sample VLT, APO, and SDSS WD spectra. These DAs have T_{eff} of 10,000–15,000 K. The top two spectra were taken with the VLT ($R \approx 14,000$) and are not flux calibrated. The middle two were taken at APO ($R \approx 2500$) and the bottom two by SDSS ($R \approx 1800$). These WDs range from $g \approx 16$ (HS 2240+1234B) to ≈ 19 mag (J0859+3306B). The spectra here and in Figure 4.23 have been smoothed using a boxcar average of width 5.

these quantities are a combination of the internal uncertainties, derived from the covariance matrix of the fitting functions, and external uncertainties of 1.2% in T_{eff} and 0.038 dex in $\log g$, derived from multiple observations of the same object (cf. Liebert et al. 2005c).

These solutions are based on one-dimensional (1D) models using a standard mixing-length parameter $ML2/\alpha = 0.8$ (Tremblay et al. 2010). Tremblay et al. (2013) produced a new suite of WDs models and solved the radiation-hydrodynamics equations in three dimensions. These authors find that using this approach rather than mixing-length theory to approximate WDs with convective atmospheres leads to substantial differences in the derived masses for WDs with $7000 < T_{\text{eff}} < 12,000$ K. We applied the fitting formulas

Tremblay et al. (2013) provide to the T_{eff} and $\log g$ solutions for all of the WDs in our sample. In the relevant region of parameter space, these adjustments tend to shift our WD solutions to lower T_{eff} and $\log g$ (or to older and less massive WDs) compared to mixing-length models.

Next, we used the Wood (1995) and Fontaine et al. (2001) models, depending on T_{eff} , to map our T_{eff} and $\log g$ values to τ_{cool} and masses (M_{WD}) for each of our WDs. Our fits also provide distances to the WDs which are determined by comparing photometric magnitudes with absolute magnitudes from the spectroscopic solutions. The resulting quantities for the DA+DA DWDs with spectra are given in Table 4.3.

4.3.3 Our Spectroscopic Sample

Our sample includes 27 DA/DA pairs. Table 4.3 shows that lower S/N spectra result in larger T_{eff} and $\log g$ uncertainties, and hence in the derived τ_{cool} and M_{WD} (for the dependence of these uncertainties on S/N, see figure 12, Gianninas et al. 2005). We therefore divided the sample into high-fidelity and low-fidelity pairs. We labeled systems with mass uncertainties $>0.1 M_{\odot}$ in at least one WD as low-fidelity. These pairs have spectra good enough to identify objects as DAs, but too poor to obtain accurate fits to model atmospheres.

As a further test, we considered the spectroscopic distances to each WD in these candidate DWDs. We designated systems with a distance difference $>25\%$ as low-fidelity. These distances do not necessarily identify these systems as random alignments, but instead reflect the accuracy of the spectral fits. After identifying eight systems as low-

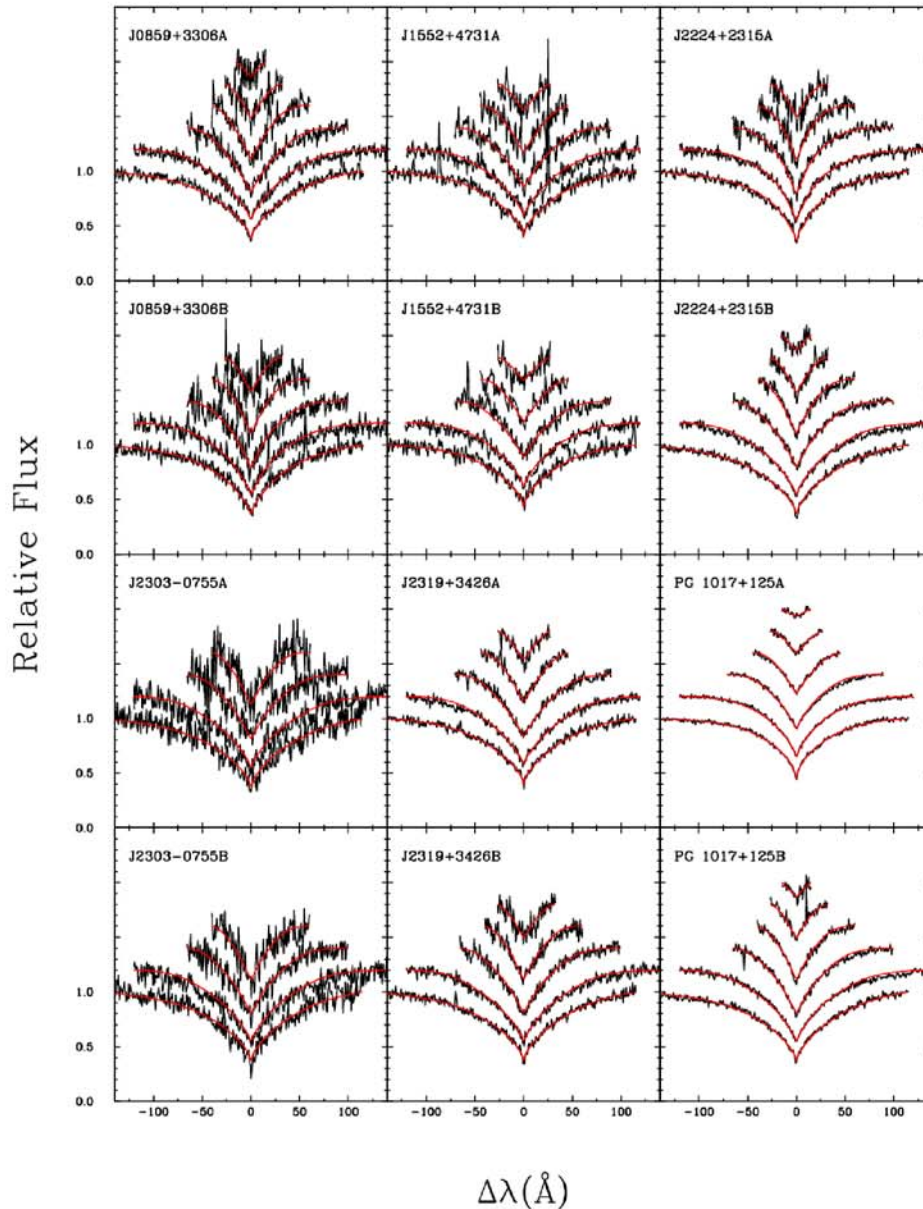


Figure 4.9 Our model fits (red) to the APO spectra of six DA/DA pairs. The number of Balmer lines fit ranges from four to six, starting with $H\beta$ at the bottom. These fits are representative of the fits to all the WDs in our spectroscopic campaign.

fidelity, we are left with 19 high-fidelity pairs as a starting point for our analysis below.

Our spectroscopic campaign also uncovered a number of pairs that, while interest-

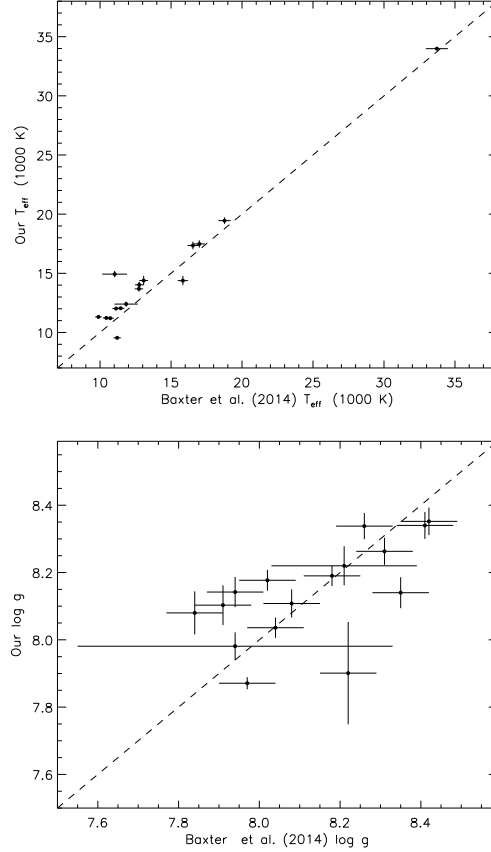


Figure 4.10 A comparison of T_{eff} and $\log g$ values derived by Baxter et al. (2014) with the values from our spectroscopic fits to the eight systems contained in both spectroscopic data sets. The dashed line shows the 1:1 correspondence. While the T_{eff} values are broadly consistent, our values appear to be slightly higher in most cases. By contrast, the $\log g$ values are well-matched for only half of the WDs and differ significantly for the other half, with no obvious trend in the differences.

ing, cannot be used to constrain the IFMR. These include the detection of two systems containing a helium-atmosphere (DB) WD (one of which was already reported by Baxter et al. 2014). We also identify seven pairs that include a candidate magnetic (DAH) WD and six pairs with a (DC) WD too cool to show significant Balmer absorption features. Finally, we obtained spectra of the two known triple degenerate systems, G 21-15 and Gr 576/577, and identified PG 0901+140 as a candidate triple degenerate. These systems are

discussed in greater detail in the Appendix.

Table 4.3: Fit Results for the DA/DA DWD Spectroscopic Sample

Name	Telescope	# of Fitted Balmer Lines	S/N ^a	T_{eff} (K)	$\log g$	Distance (pc)	M_{WD} (M_{\odot})	τ_{cool} (Myr)
High-Fidelity Systems								
HS 0507+0434A	VLT	6	25,22	21450±310	8.00±0.04	51±2	0.629±0.024	50±7
HS 0507+0434B	VLT	6	19,12	12070±190	8.07±0.05	52±2	0.649±0.030	406±33
HS 2240+1234A	VLT	6	1,11	15320±230	8.04±0.04	96±3	0.636±0.026	197±17
HS 2240+1234B	VLT	5	1,10	14150±290	8.10±0.05	99±4	0.668±0.028	272±25
J0332-0049A	SDSS	6	25,23	10940±180	8.10±0.06	168±7	0.661±0.036	544±52
J0332-0049B	VLT	5	2,16	33990±490	7.87±0.05	177±6	0.594±0.022	6±<1
J0754+1239A	APO	5	17	14190±1070	8.24±0.12	258±23	0.755±0.074	335±95
J0754+1239B	APO	5	15	13690±630	8.31±0.11	247±22	0.801±0.072	415±91
J0827-0216A	APO	5	30	27310±450	8.49±0.06	260±13	0.933±0.035	68±11
J0827-0216B	APO	5	24	27860±490	8.58±0.07	265±16	0.989±0.039	79±14
J0859+3306A	APO	6	30	14930±340	7.98±0.06	232±10	0.602±0.034	194±23
J0859+3306B	APO	5	21	12140±280	8.18±0.07	228±12	0.718±0.045	470±59
J1231+5736A	APO	5	38	15360±290	8.01±0.05	217±18	0.618±0.031	185±19
J1231+5736B	APO	5	22	11190±230	7.92±0.08	231±13	0.556±0.046	404±47
J1257+1925A	SDSS	5	10	11750±470	7.91±0.16	456±51	0.552±0.089	350±83
J1257+1925B	SDSS	5	57	47800±990	7.76±0.07	503±32	0.579±0.029	2±<1
J1313+2030A	APO	5	30	14390±450	8.34±0.06	156±8	0.823±0.037	382±49
J1313+2030B	APO	6	40	14030±330	8.19±0.05	147±6	0.726±0.033	322±33
J1552+4731A	APO	5	24	17350±410	8.10±0.07	382±20	0.679±0.044	148±23
J1552+4731B	APO	5	27	19450±390	8.14±0.06	367±17	0.707±0.037	107±16
J2222-0828A	APO	5	41	14380±440	8.18±0.05	92±4	0.719±0.033	295±35
J2222-0828B	APO	5	29	11750±220	8.08±0.06	112±5	0.653±0.038	442±45
HS 2220+2146A	VLT	5	8,11	14270±270	8.15±0.04	79±2	0.702±0.022	289±22
HS 2220+2146B	VLT	5	10,16	18830±220	8.35±0.04	73±2	0.837±0.022	179±14
J2224+2315A	APO	5	39	10930±180	8.16±0.06	137±6	0.702±0.036	604±61
J2224+2315B	APO	6	47	13690±300	8.04±0.05	139±5	0.631±0.031	274±27
J2303-0755A	APO	5	15	14400±960	8.27±0.10	194±16	0.777±0.065	339±84
J2303-0755B	APO	5	18	13900±730	8.04±0.09	223±15	0.635±0.054	264±54
J2319+3426A	APO	5	43	16320±270	8.12±0.05	162±6	0.684±0.030	183±18
J2319+3426B	APO	5	33	14140±450	8.05±0.05	172±7	0.641±0.032	255±31
LP 128-254	APO	6	35	14030±470	8.07±0.06	164±7	0.652±0.034	269±34
LP 128-255	SDSS	5	25	11080±200	7.98±0.07	164±8	0.589±0.040	447±45
LP 370-50	APO	5	30	7560±120	8.19±0.09	59±4	0.710±0.055	1668±324
LP 370-51	APO	5	31	7210±120	8.14±0.10	61±4	0.681±0.061	1723±349
PG 0901+140A ^b	APO	6	67	9100±140	7.78±0.08	59±3	0.474±0.041	585±57
PG 0901+140B	APO	6	39	8120±120	7.89±0.07	58±3	0.531±0.039	886±87
PG 0922+162A	VLT	5	15,15	24480±350	8.28±0.04	158±6	0.797±0.028	59±9
PG 0922+162B	VLT	4	20,8	26500±440	9.04±0.06	110±7	1.220±0.023	227±23
PG 1017+125A	APO	6	90	22130±330	7.99±0.04	106±4	0.622±0.024	41±6
PG 1017+125B	APO	6	50	13580±240	8.12±0.05	108±4	0.681±0.030	317±28
Low-Fidelity Systems								
J1002+3606A	APO	5	20	9720±160	8.42±0.10	152±12	0.863±0.063	1287±296
J1002+3606B	SDSS	4	9	11650±580	8.26±0.21	226±38	0.767±0.135	594±217
J1110+4517A	APO	6	23	13700±370	8.10±0.06	113±5	0.670±0.038	301±36
J1110+4517B	APO	5	46	19000±300	8.12±0.05	152±6	0.692±0.029	111±13
J1203+4948A	APO	6	25	11410±220	8.12±0.07	119±6	0.674±0.041	502±56
J1203+4948B	APO	5	14	7250±150	8.06±0.21	118±18	0.631±0.129	1507±621
J1309+5503A	SDSS	5	13	8120±160	7.94±0.18	136±16	0.560±0.100	951±234

Continued on next page

Table 4.3 – Continued from previous page

Name	Telescope	# of Fitted Balmer Lines	S/N ^a	T_{eff} (K)	$\log g$	Distance (pc)	M_{WD} (M_{\odot})	τ_{cool} (Myr)
J1309+5503B	SDSS	5	22	8090±140	8.17±0.11	85±7	0.698±0.071	1345±277
J1546+6159A	APO	5	20	10880±190	7.84±0.07	244±12	0.514±0.039	398±39
J1546+6159B	APO	6	70	16510±270	8.06±0.05	143±6	0.649±0.029	159±16
J1703+3304A ^c	SDSS	5	12	9400±180	7.63±0.16	239±24	0.424±0.069	874±72
J1703+3304B	SDSS	6	33	11030±190	8.19±0.06	156±7	0.718±0.037	614±64
J0030+1810A	APO	5	11	14070±1050	8.42±0.18	222±33	0.870±0.115	458±167
J0030+1810B	APO	5	5	15620±2930	8.43±0.35	244±77	0.880±0.214	351±306
J1113+3238A	SDSS	4	10	6680±230	7.33±0.54	156±49	0.307±0.185	1474±466
J1113+3238B	SDSS	4	8	7760±260	8.82±0.33	78±27	1.107±0.170	3646±233
J2326–0023A	SDSS	4	9,9	7530±180	8.45±0.23	114±21	0.884±0.151	3028±968
J2326–0023B	SDSS	6	28	10530±170	8.02±0.06	124±5	0.611±0.036	538±50

Note. – When multiple spectra were available, we list the fit to the DA’s best spectrum, which we define as the fit that produces a distance that best matches its companion’s. For previously identified systems, we label the WDs “A” and “B” as in the literature. We order newly identified systems by their RA as opposed to e.g., their relative brightnesses.

^a Entries with more than one listed S/N indicate that multiple spectra were used to fit for the WD parameters.

^b Given its anomalously low mass, PG 0901+140A may be an unresolved triple system.

^c Despite its low mass, J1703+3304A (CDDS40-B) is unlikely to be an unresolved double degenerate (cf. discussion in the Appendix), because the discrepant distances indicate a poor fit.

4.3.4 Comparison to the Baxter et al. (2014) Fit Results

Baxter et al. (2014) identified 53 DWDs, and 12 are included in our spectroscopic sample. Baxter et al. (2014) obtained spectra for eight of these pairs. In Figure 4.10, we compare the $\log g$ and T_{eff} values these authors derived to ours. Half the WDs have T_{eff} and $\log g$ values in agreement; the other half have significantly different spectroscopic solutions, particularly in $\log g$. This is similar to what Baxter et al. (2014) found when comparing their spectroscopic results to the SDSS-derived results of Kleinman et al. (2013): of the five Kleinman et al. (2013) WDs for which Baxter et al. (2014) have spectra, two have significantly differing $\log g$ values.

We show the WD masses derived from these spectral solutions for the 16 WDs in both spectroscopic samples in Figure 4.11. We find that our M_{WD} estimates are systematically

larger by $\approx 0.05 M_{\odot}$. We ascribe these differences to the combination of observations made with instruments with different resolutions and of spectral fitting done with different techniques and atmospheric models.

As the Baxter et al. (2014) spectroscopic sample represents a significant addition to our own, we include the WDs in our analysis below. For systems in both the Baxter et al. (2014) spectroscopic sample and our own, we use the values derived from our spectra.

4.3.5 Our DWD Sample for Constraining the IFMR

Standard stellar evolution theory predicts that the more massive WDs in DWDs are also the older WDs: more massive stars evolve faster, becoming more massive WDs with larger τ_{cool} than their less massive companions. Of the 20 high-fidelity systems in Table 4.3, PG 0901+140 may be a triple system (see discussion in the Appendix) and five appear to host a more massive WD that is younger than its companion: J1231+5736, J1552+4731 (CDDS36), J2222-0828 (CDDS48), HS 2220+2146, and LP 128-254/255. We remove these and use the remaining 14 systems for our analysis.

We then consider the 10 Baxter et al. (2014) systems for which we have poor or no spectroscopic data. We remove five of these systems from our analysis. One of the WDs in CDDS16 has poor S/N; the higher-order Balmer lines are particularly noisy, which impacts the determination of $\log g$. Baxter et al. (2014) identified CDDS30 as a possible triple system. CDDS31 has a projected separation of ≈ 100 AU and could therefore have had previous mass-transfer episodes. The more massive WD in CDDS26 appears to be younger than its companion. Finally, SDSS spectra are available for both WDs in CDDS7,

but the spectra are very poor. We add the remaining five pairs to our sample, so that we now have 19 DWDs with which to constrain the IFMR (see Table 4.4).

4.4 Constraining the IFMR with DWDs

We begin by examining several of the basic assumptions that allow one to use DWDs to constrain the IFMR. These are that the two WDs are co-eval and have not been subjected to significant mass transfer during their lifetimes, that our DWD progenitors did not vary significantly in metallicity, and that the pre-WD lifetimes produced by stellar evolution codes for stars of a given mass are relatively insensitive to the parameters one uses in these calculations. We then revisit the Finley & Koester (1997) result before developing a flexible, Bayesian method that takes into account measurement uncertainties and provides statistically rigorous constraints on the IFMR.

4.4.1 Examining the Underlying Assumptions

4.4.1.1 Co-evolution and Independence of Wide DWDs

Binary star formation theory suggests that the collapse of gas clouds in multistellar systems occurs on a dynamical timescale (Shu et al. 1987); for typical binaries, this is <1 Myr. This expectation has been borne out by observations of binaries in the Taurus-Auriga cluster by Kraus & Hillenbrand (2009), which suggest that the age difference of the stars in binaries is even smaller than that of stars within an open cluster. Since the probability that field DWD progenitor systems formed through gravitational capture is extraordinarily small,

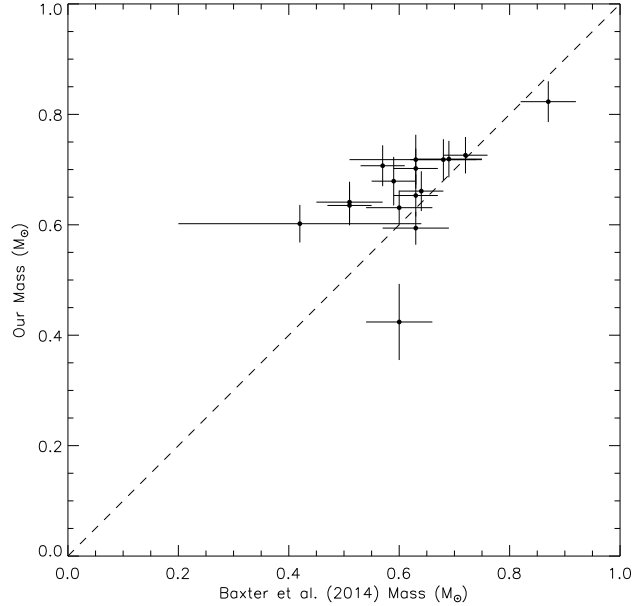


Figure 4.11 Comparison of the M_{WD} of Baxter et al. (2014) and obtained from our spectra for 16 WDs in eight DWDs included in both spectroscopic samples. The dashed line shows the 1:1 correspondence. Our M_{WD} estimates are systematically larger by $\approx 0.05 M_{\odot}$, presumably due to the use of spectra with different resolutions and fitting codes with different model atmospheres.

we can safely assume the stars in a wide binary are born together through fragmentation (Boss 1988).

Wide binaries with small enough separations could have interacted in the past, potentially through wind-fed mass transfer. Indeed, below some critical (but still relatively large) separation, some amount of mass transfer is unavoidable, and may impact the system's evolution. For example, Mira, with a separation of ≈ 70 AU, shows mass accretion at a rate of $\approx 10^{-10} M_{\odot} \text{ yr}^{-1}$ (Sokoloski & Bildsten 2010), high enough to potentially induce periodic nova eruptions on the WD surface every $\approx \text{Myr}$, which would affect its derived

τ_{cool} .

Such mass accretion could be due to so-called wind Roche lobe overflow (Mohamed & Podsiadlowski 2007, 2012). These authors argue that when an asymptotic giant branch (AGB) donor is emitting a slow wind, a companion at tens of AU can channel a substantial fraction of the lost mass. Abate et al. (2013) suggest that wind Roche lobe overflow can occur when the companion is at a separation less than the AGB's dust formation radius, because at larger separations the increased opacity due to dust means that radiation pressure will quickly push the wind to escape the system. Observations suggest that this radius is also \approx tens of AU (Höfner 2009; Karovicova et al. 2013).

More work is needed to determine the spatial separation at which the effects of wind-fed mass transfer can be ignored. However, since the smallest projected binary separation of the wide DWDs in our sample is hundreds of AU (see Table 4.4), we expect mass accretion to be negligible, even in prior evolutionary states when the binaries may have had somewhat smaller separations.

4.4.1.2 Metallicity of the DWD progenitors

In their analysis of WDs in the open cluster M37, Kalirai et al. (2005) found that their data were consistent with stars of a given M_i producing higher mass WDs than in previous studies. These authors suggested that the lower metallicity of M37 might result in less mass loss on the AGB and, therefore, more massive WDs.

Theory supports this interpretation: Renedo et al. (2010) found that metal-poor stars undergo more thermal pulses on the AGB, resulting in more massive WDs. Variations in metallicity should result in WD masses varying by $\approx 0.1 M_\odot$ for a given M_i . However, for

Table 4.4: DA/DA DWDs Used to Constrain the IFMR

Name	$M_{\text{WD},1}$ (M_{\odot})	$M_{\text{WD},2}$ (M_{\odot})	$\tau_{\text{cool},1}$ (Myr)	$\tau_{\text{cool},2}$ (Myr)	Distance ^a (pc)	θ (asec)	s (AU)
HS 0507+0434	0.649±0.030	0.629±0.024	406±33	50±7	51	18	919
HS 2240+1234	0.668±0.028	0.636±0.026	272±25	197±17	97	12	1166
J0332-0049	0.661±0.036	0.594±0.022	544±52	6±< 1	173	19	3290
J0754+1239	0.801±0.072	0.755±0.074	415±91	335±95	252	2	504
J0827-0216	0.989±0.039	0.933±0.035	79±14	68±11	262	3	787
J0859+3306	0.718±0.045	0.602±0.034	470±59	194±23	231	9	2080
J1257+1925	0.579±0.029	0.552±0.089	2±< 1	350±83	490	12	5888
J1313+2030	0.823±0.037	0.726±0.033	382±49	322±33	150	6	901
J2224+2315	0.702±0.036	0.631±0.031	604±61	274±27	138	3	415
J2303-0755	0.777±0.065	0.635±0.054	339±84	264±54	209	8	1670
J2319+3426	0.684±0.030	0.641±0.032	183±18	255±31	167	5	836
LP 370-50/51	0.710±0.055	0.681±0.061	1670±320	1720±350	60	13	781
PG 0922+162	1.220±0.023	0.797±0.028	227±23	59±9	158	5	791
PG 1017+125	0.681±0.030	0.622±0.024	317±28	41±6	107	49	5250
CDDS3	0.592±0.036	0.579±0.034	78±14	491±63	256	7	1792
CDDS6	0.668±0.039	0.655±0.040	31±8	114±19	192	2	385
CDDS9	0.598±0.058	0.535±0.070	142±32	376±69	506	12	6080
CDDS14	0.644±0.041	0.590±0.045	428±54	598±91	211	5	1056
CDDS40	0.694±0.043	0.634±0.040	876±129	530±70	187	11	1419

Note. – In this table WDs 1 and 2 are the more and less massive WDs in the pair, respectively.

^a This is the average of the distance to each WD.

near-solar metallicities, the IFMR does not vary much (Marigo & Girardi 2007; Meng et al. 2008; Romero et al. 2015).

Fortunately, the WDs in our sample should have roughly similar, near-solar metallicities. We cannot directly test for the metallicity of a WD progenitor, but there are indications that most disk stars born in the past several Gyr likely have similar metallicities. For example, in a study of local F and G type stars, Fuhrmann (1998) found that kinematically identified thin-disk stars have [Fe/H] and [Mg/H] metallicity indicators within 0.3 dex of solar.

As shown in Figure 4.2, our subset of candidate WDs with measured proper motions

Table 4.5. MESA Model Parameters

Parameter	Fiducial Model
number of isotopes	26 (up to Mg)
metallicity	$z = 0.02$
mixing length	$\alpha_{\text{MLT}} = 1.73$
overshoot parameter	$f = 0.014$
photospheric model	<code>simple_photosphere</code>
RGB mass loss	Reimers, $\eta = 0.5$
AGB mass loss	Blocker, $\eta = 0.5$
opacity tables	Grevesse & Noels (1993)
convection	Schwartzchild criterion
rotation	off

almost all have transverse velocities consistent with being in the Galactic disk. Furthermore, since we selected relatively hot WDs for the spectroscopic follow-up described in Section 4.3, all of the wide DWDs in our sample are relatively young. We therefore expect the progenitors of the WDs in our sample to have had a metallicity close to $z = 0.02$.

4.4.1.3 Robustness of the Pre-WD Lifetime Function

We obtain a pre-WD lifetime function, F , by running models from MESA. MESA is a suite of modules that includes integrated equations-of-state tables, opacity tables, nuclear reaction networks, and elemental diffusion rates. The stellar evolution module, `MESA_star`, solves the stellar structure equations using a 1D, adaptive Lagrangian algorithm. Built with state-of-the-art prescriptions, `MESA_star` has been extensively tested and compared to observations and other stellar evolution codes (Paxton et al. 2011, 2013, 2015).

The parameters and prescriptions used in our fiducial model are given in Table 4.5.

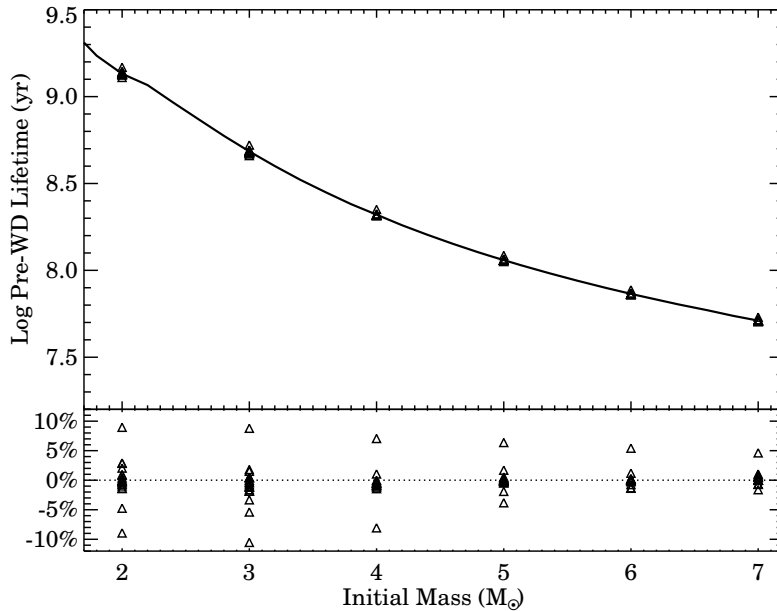


Figure 4.12 Pre-WD lifetime (approximated by the age at the 1TP) as a function of initial mass. The solid line shows ages produced by our fiducial model, while the triangles show the results of MESA models generated varying a number of prescriptions. The lower panel shows that the pre-WD lifetimes produced by these tests are robust, as they typically vary by less than 5% even for very different models.

Stars begin as gas clouds on the pre-Main Sequence. Once fusion begins, the reaction network tracks the concentrations of isotopes. Convection is treated as an exponential diffusive process, with a diffusive constant and adjustable scale length based on the pressure scale height; semi-convection is not included in our fiducial model. Exponential mixing near the convective boundary due to overshooting is included (Freytag et al. 1996; Herwig et al. 1997).

We stop our model at the first thermal pulse (1TP), the start of the thermally pulsing AGB (TP-AGB). We set the star's age here as its pre-WD lifetime, as evolution through the TP-AGB is quick (10^5 to 10^6 yr, or $<1\%$ of its lifetime), with higher mass stars evolving

faster (Vassiliadis & Wood 1993).

We run simulations for our fiducial model for $M_i = 0.6\text{--}8.0 M_\odot$ in $0.2 M_\odot$ steps. To determine the pre-WD lifetime for an arbitrary M_i , we linearly interpolate over the values in this grid. The resulting pre-WD lifetime function is indicated by the solid line in Figure 4.12.

In comparing MESA to other stellar evolution codes, Paxton et al. (2011) found that the derived stellar lifetimes agreed within $\approx 5\%$. However, Paxton et al. (2013) showed that the choice of parameters and prescriptions may have a stronger impact on the stellar lifetime. We therefore tested 19 MESA models in addition to our fiducial model, varying the metallicity, atmospheric models, opacity tables, mixing length, and also included rotation and semi-convection. A detailed discussion of how each parameter affects the stellar lifetime is outside the scope of this work; we used these models to gauge the level of uncertainty in the stellar lifetimes.

The symbols in Figure 4.12 show how the lifetimes we obtain vary from model to model for $2 \leq M_i \leq 7 M_\odot$. The bottom panel shows that the majority of our 19 models produce lifetimes within a few percent of those obtained using our fiducial model. The largest differences in the lifetimes occur when changing the initial composition of the star. Models run with the Asplund et al. (2009) opacity tables lead to lifetimes longer by $\approx 10\%$ than those from models run with the fiducial Grevesse & Noels (1993) tables. Conversely, models with sub-solar metallicities lead to shorter lifetimes (e.g., by $\approx 10\%$ for $z = 0.01$). Since this is a relatively minor uncertainty, we ignore it in our analysis, particularly since, as discussed above, we expect our DWD progenitors to have had similar, approximately

solar metallicities.

4.4.2 Revisiting the Finley & Koester (1997) Result

Finley & Koester (1997) constrained the IFMR using the wide DWD PG 0922+162. These authors compared the more massive WD ($\gtrsim 1.10 M_{\odot}$) to similarly massive WDs in open clusters for which M_i had been published, thereby obtaining $M_i = 6.5 \pm 1.0 M_{\odot}$ for this WD.⁹ Finley & Koester (1997) converted this mass into a pre-WD lifetime of 42–86 Myr, to which they added the τ_{cool} of the massive WD to derive a system age of 320 ± 32 Myr. These authors then used the less massive WD in PG 0922+162 ($M_{\text{WD}} = 0.8 M_{\odot}$) to constrain the IFMR: they derived a pre-WD lifetime for this WD of 231 ± 34 Myr by subtracting its τ_{cool} from the system age, and obtained $M_i = 3.8 \pm 0.2 M_{\odot}$ for its progenitor.

In Figure 4.13 we reproduce one of the key steps in this analysis, the conversion of pre-WD lifetimes into initial masses. Because the relation between lifetime and mass is steeper for longer-lived, lower-mass stars, even relatively large uncertainties in the assumed M_i for the more massive WD in PG 0922+162 results in stringent constraints on the M_i of the less massive WD. Indeed, the Finley & Koester (1997) result is one of the most stringent constraints on the IFMR, and is one of the reasons why Weidemann (2000) anchored his semi-empirical IFMR at $M_i = 4 M_{\odot}$ and $M_{\text{WD}} = 0.8 M_{\odot}$.

⁹This is one of the difficulties in directly applying this method to other DWDs, since comparing the more massive WD in a DWD to WDs in open clusters cannot always be done for a generic DWD.

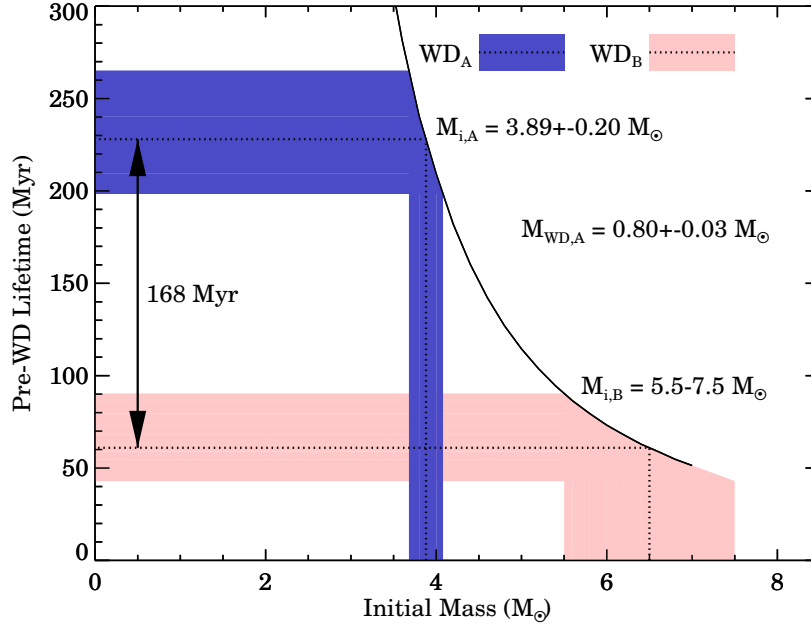


Figure 4.13 Converting M_i into pre-WD lifetimes. Finley & Koester (1997) assigned the more massive WD_B in PG 0922+162 a $M_i = 6.5 \pm 1.0 M_\odot$, which corresponds to a pre-WD lifetime of 43–90 Myr (we use our mesa stellar lifetime function here). Adding the τ_{cool} difference between the two WDs gives a pre-WD lifetime of 198–265 Myr for the less massive WD_A . We derive a corresponding $M_i = 3.89 \pm 0.20 M_\odot$ for WD_A ; Finley & Koester (1997) found $3.8 \pm 0.2 M_\odot$. Despite the relatively large uncertainty in the initial mass of WD_B , the uncertainty in the initial mass of WD_A is small, particularly compared to typical uncertainties derived from other observational methods.

4.4.3 A New Parametric Model for the IFMR

While the Finley & Koester (1997) result indicates that DWDs can be powerful systems for constraining the IFMR, these authors' approach cannot be replicated for a generic set of wide DWDs such as the one we have assembled. We therefore develop a new method for constraining the IFMR with wide DWDs by constructing a parametric model for the IFMR. Our approach is presented in schematic form in Figure 4.14.

We begin by considering the observables: the cooling ages, $\tau_{\text{cool},1}$ and $\tau_{\text{cool},2}$, and WD masses, $M_{\text{WD},1}$ and $M_{\text{WD},2}$. If the WDs are indeed co-eval and evolved independently, the

difference in the cooling ages must be equal to the difference in the pre-WD lifetimes, τ_1 and τ_2 . If WD_1 is the more massive, older WD and therefore had the shorter pre-WD lifetime,

$$\Delta\tau_{\text{cool}} = -\Delta\tau \quad (4.1)$$

$$\tau_{\text{cool},1} - \tau_{\text{cool},2} = -(\tau_1 - \tau_2). \quad (4.2)$$

While $\tau_{\text{cool},1}$ and $\tau_{\text{cool},2}$ are observed, τ_1 and τ_2 are obtained by a functional transformation from M_{WD} :

$$\tau_1 = FM_i \quad (4.3)$$

$$= FG^{-1}M_{\text{WD}} \quad (4.4)$$

where F is the pre-WD lifetime function, and we have applied the inverse IFMR, G^{-1} to obtain M_i from the observed WD masses. Combining these, we obtain:

$$\tau_{\text{cool},1} - \tau_{\text{cool},2} = FG^{-1}M_{\text{WD},2} - FG^{-1}M_{\text{WD},1}. \quad (4.5)$$

Since FM_i can be determined with accuracy from stellar evolution codes (see Section 4.4.1.3), we now need to find the best G^{-1} that satisfies Equation 4.5. Below, we construct a likelihood function that evaluates the ability for any G^{-1} to account for the observations. We then define a parametric model for G , and iterate over these model parameters, Θ , to find the highest likelihood set. As discussed below, because of the

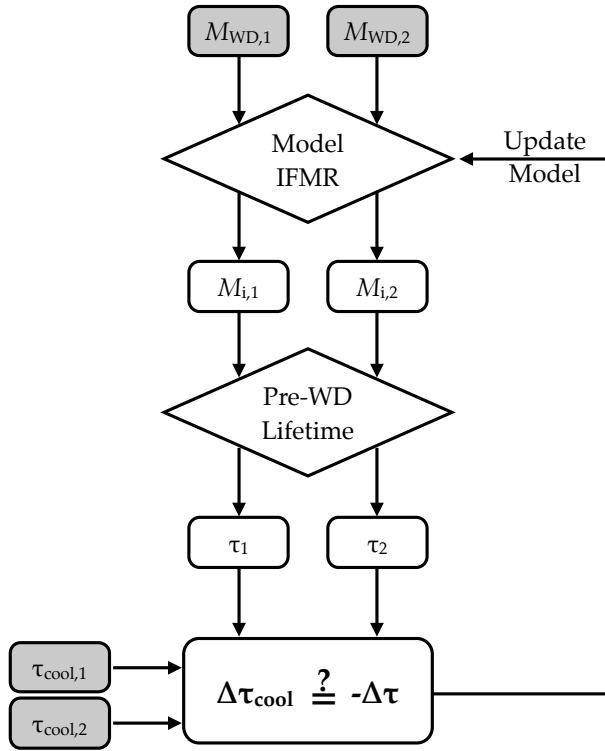


Figure 4.14 A schematic summary of our method. Gray boxes indicate observed quantities. We convert each M_{WD} into a M_i using a candidate IFMR, and then find the corresponding pre-WD lifetime, τ , using the function shown in Figure 4.12. The difference of these lifetimes should be equal to $\Delta\tau_{cool}$, which we obtain from the two observed τ_{cool} . Our problem is then reduced to iterating over our model parameters to find the IFMR that makes this equality true for our set of wide DWDs.

functional form of the IFMR, finding the best G^{-1} is directly equivalent to finding the best G and therefore constraining the IFMR.

4.4.3.1 Bayesian Framework

We calculate a likelihood function for a particular IFMR, using a Bayesian hierarchical model to account for measurement uncertainties. We begin with Bayes's rule:

$$P(\Theta | D, I) = \frac{P(D | \Theta, I)P(\Theta | I)}{P(D | I)}, \quad (4.6)$$

where D is the set of observed wide DWDs,¹⁰ and I represents our prior information and assumptions about the data and model. For instance, observational uncertainties are contained within I . $P(\Theta | D, I)$ is the posterior probability we are looking for, $P(D | I)$ is a constant dependent only on the data, $P(\Theta | I)$ are the priors on our model, and $P(D | \Theta, I)$ is the likelihood. The posterior probability over the set of data is a product over individual measurements:

$$P(D | \Theta, I) = \prod_{D \in \mathcal{D}} P(D | \Theta, I). \quad (4.7)$$

We now substitute in the individual observables:

$$P(D | \Theta, I) = P(M'_1, M'_2, \Delta\tau_{\text{cool}}' | \Theta, I). \quad (4.8)$$

To construct our likelihood function, we first marginalize over τ_1 , τ_2 , and $\Delta\tau$:

$$P(D | \Theta, I) = \int_0^\infty \int_0^\infty \int_{-\infty}^\infty d\tau_1 d\tau_2 d\Delta\tau P(\tau_1, \tau_2, \Delta\tau, M'_1, M'_2, \Delta\tau_{\text{cool}}' | \Theta, I). \quad (4.9)$$

Hereafter, primed quantities refer to observed values and unprimed quantities refer

¹⁰ D refers to the set of wide DWDs, while D refers to an individual system.

to true values. Because observations of each WD and of $\Delta\tau_{\text{cool}}$ are all independent, we can factor this probability:

$$P(D|\Theta, I) = \int_0^\infty \int_0^\infty d\tau_1 d\tau_2 P(M'_1|\tau_1, \Theta, \sigma_{M_1}) P(M'_2|\tau_2, \Theta, \sigma_{M_2}) P(\tau_1|\Theta) P(\tau_2|\Theta) \\ \times \int_{-\infty}^\infty d\Delta\tau P(\Delta\tau_{\text{cool}}'|\Delta\tau, \sigma_{\Delta\tau_{\text{cool}}}) P(\Delta\tau|\tau_1, \tau_2), \quad (4.10)$$

where here we also factored I into individual observational uncertainties. The conditional probability over $\Delta\tau$ is a delta function:

$$P(\Delta\tau|\tau_1, \tau_2) = \delta(\Delta\tau - \tau_1 + \tau_2), \quad (4.11)$$

and the conditional probability over $\Delta\tau_{\text{cool}}'$ is a Gaussian distribution:

$$P(\Delta\tau_{\text{cool}}'|\Delta\tau, \sigma_{\Delta\tau_{\text{cool}}}) = \mathcal{N}(-\Delta\tau|\Delta\tau_{\text{cool}}', \sigma_{\Delta\tau_{\text{cool}}}), \quad (4.12)$$

where the negative sign is from Equation 4.1. After reducing the innermost integral, Equation 4.10 simplifies to:

$$P(D|\Theta, I) = \int_0^\infty \int_0^\infty d\tau_1 d\tau_2 P(M'_1|\tau_1, \Theta, \sigma_{M_1}) P(M'_2|\tau_2, \Theta, \sigma_{M_2}) P(\tau_1|\Theta) P(\tau_2|\Theta) \\ \times \mathcal{N}[(\tau_1 - \tau_2)|\Delta\tau_{\text{cool}}', \sigma_{\Delta\tau_{\text{cool}}}], \quad (4.13)$$

Evaluating Equation 4.13 is unnecessarily computationally expensive, since only a small region of the domain has any contributing probability. We therefore use a Monte

Carlo method to approximate the double integral as a single sum over randomly drawn τ_1 and τ_2 . We make this approximation with a single rather than double sum because the first two terms in the integrand, the observed WD masses, are independent of each other:

$$P(D|\Theta, I) \approx \frac{1}{N} \sum_k P(\tau_{1k}|\Theta)P(\tau_{2k}|\Theta) \mathcal{N}[(\tau_{1k} - \tau_{2k})|\Delta\tau_{\text{cool}}, \sigma_{\Delta\tau_{\text{cool}}}], \quad (4.14)$$

where there are N random draws of τ_{1k} and τ_{2k} from the distributions:

$$\begin{aligned} \tau_{1k} &\sim P(\tau_1|M'_1, \Theta, \sigma_{M_1}) = P(M'_1|\tau_1, \Theta, \sigma_{M_1}) \\ \tau_{2k} &\sim P(\tau_2|M'_2, \Theta, \sigma_{M_2}) = P(M'_2|\tau_2, \Theta, \sigma_{M_2}). \end{aligned} \quad (4.15)$$

Here, we have applied Bayes's theorem to make the equalities on the right side of these equations. To generate these random distributions:

$$\begin{aligned} P(\tau_1|M'_1, \Theta, \sigma_{M_1}) &= P(\mathbf{GF}^{-1}\tau_1|M'_1, \sigma_{M_1}) \left| \frac{d\mathbf{GF}^{-1}\tau_1}{d\tau_1} \right| \\ P(\tau_2|M'_2, \Theta, \sigma_{M_2}) &= P(\mathbf{GF}^{-1}\tau_2|M'_2, \sigma_{M_2}) \left| \frac{d\mathbf{GF}^{-1}\tau_2}{d\tau_2} \right|. \end{aligned} \quad (4.16)$$

We determine the derivatives numerically, and the observational uncertainties in WD mass are Gaussian:

$$\begin{aligned} P(\mathbf{GF}^{-1}\tau_1|M'_1, \sigma_{M_1}) &= \mathcal{N}(\mathbf{GF}^{-1}\tau_1|M'_1, \sigma_{M_1}) \\ P(\mathbf{GF}^{-1}\tau_2|M'_2, \sigma_{M_2}) &= \mathcal{N}(\mathbf{GF}^{-1}\tau_2|M'_2, \sigma_{M_2}). \end{aligned} \quad (4.17)$$

Equations 4.7, 4.14, 4.16, and 4.17 define the model likelihood. For a given model,

finding the model parameters, Θ , implied by our set of wide DWDs involves maximizing the likelihood function in Equation 4.14.

We are interested in determining the precision of the constraints we can place on our model parameters, and therefore chose a Monte Carlo technique rather than a maximum-likelihood calculation. Specifically, we used the Markov Chain Monte Carlo algorithm *emcee* (Foreman-Mackey et al. 2013b), which implements an affine invariant, ensemble sampler algorithm to search the parameter space (Goodman & Weare 2010).

4.4.3.2 Parametric Model

We define our model by first including a parametrization that determines $P(\tau_1 | \Theta)$ and the corresponding quantity for the second WD. To keep the dimensionality of the problem low, our likelihood function (Equation 4.14) marginalizes over all possible pre-WD lifetimes.

Standard stellar evolution precludes the existence of WDs more massive than the Chandrasekhar mass ($\approx 1.35 M_\odot$). At the other end, the Galaxy is not old enough to produce isolated WDs less massive than $\lesssim 0.45 M_\odot$ (Kilic et al. 2007), except in cases of extremely high metallicity. We therefore use a truncated Gaussian to describe the WD mass distribution, $0.45 M_\odot < M_{\text{WD}} < 1.35 M_\odot$, which we can model using the mean mass μ_{WD} and standard deviation $\sigma_{M_{\text{WD}}}$ as parameters.

We set flat priors on μ_{WD} and $\sigma_{M_{\text{WD}}}$, limiting their ranges:

$$\begin{aligned} \frac{\mu_{\text{WD}}}{M_\odot} &\in [0.1, 1.5] \\ \frac{\sigma_{\text{WD}}}{M_\odot} &\in [0.1, 1.0]. \end{aligned} \tag{4.18}$$

More complex models may better represent the WD mass distribution, but for our purposes, this Gaussian model is sufficient. This allows us to add to our model two hyperparameters that weigh τ_1 and τ_2 :

$$P(\tau_1 | \Theta) = \mathcal{N}(GF^{-1}\tau_1 | \mu_{\text{WD}}, \sigma_{M_{\text{WD}}}) \quad (4.19)$$

$$P(\tau_2 | \Theta) = \mathcal{N}(GF^{-1}\tau_2 | \mu_{\text{WD}}, \sigma_{M_{\text{WD}}}). \quad (4.20)$$

Next, we choose a parametric form for the IFMR, G . We expect that the IFMR has three distinct regimes: for $M_i \lesssim 2 M_\odot$, stars undergo a degenerate helium flash (Sweigart & Gross 1978). For $2 \lesssim M_i \lesssim 4 M_\odot$, stars will undergo stable, non-degenerate helium burning. Finally, second dredge-up becomes important for stars with $M_i \gtrsim 4 M_\odot$ (Dominguez et al. 1999).

Theoretical IFMRs from stellar evolution codes indicate roughly linear IFMRs for each of these regimes, with pivots at $M_{p,1} = 2$ and $M_{p,2} = 4 M_\odot$. Assuming a continuous IFMR, we therefore construct a three-component, piecewise linear model with four free parameters: three separate slopes for each regime and a y-intercept that translates the relation vertically.

We then follow Hogg et al. (2010) and parametrize the linear relations in terms of the angle each line makes with the horizontal, not the slope (ϕ , not m), and the perpendicular

distance of the line from the origin, not the intercept (b_{\perp} , not b):

$$\mathbf{G} = \begin{cases} \tan \phi_1 (M_i) + b_1 & : M_i < M_{p,1} \\ \tan \phi_2 (M_i) + b_2 & : M_{p,1} < M_i < M_{p,2} \\ \tan \phi_3 (M_i) + b_3 & : M_{p,2} < M_i. \end{cases} \quad (4.21)$$

To ensure the model is continuous, we have:

$$\begin{aligned} b_2 &= (\tan \phi_1 - \tan \phi_2) M_{p,1} + b_1 \\ b_3 &= (\tan \phi_2 - \tan \phi_3) M_{p,2} + b_2 \end{aligned} \quad (4.22)$$

Combined with our two WD mass distribution parameters, the piecewise function can then be expressed in terms of our four IFMR model parameters:

$$\begin{aligned} \Theta &= (\Theta_{\text{WD}}, \Theta_{\text{IFMR}}) \\ \Theta &= (\mu_{\text{WD}}, \sigma_{\text{WD}}, b_{\perp}, \phi_1, \phi_2, \phi_3), \end{aligned} \quad (4.23)$$

where $b_{\perp} = b_1 \cos \phi_1$. We include priors on our model parameters to ensure that the model IFMR is an increasing function:

$$\begin{aligned} \phi_1 &\in [0, \pi/2] \\ \phi_2 &\in [0, \pi/2] \\ \phi_3 &\in [0, \pi/2]. \end{aligned} \quad (4.24)$$

Finally, we add a prior to our model so that G intercepts the y -axis above the origin, and a second prior that ensures that a $7.0 M_{\odot}$ star produces a WD with a mass between 1.0 and $1.4 M_{\odot}$:

$$\begin{aligned} 0 &< G(0.0 M_{\odot}) < 0.5 M_{\odot} \\ 1.0 &< G(7.0 M_{\odot}) < 1.4 M_{\odot}. \end{aligned} \tag{4.25}$$

4.4.4 Testing the Model with Mock Data

We generate a set of mock observations using a test IFMR, then compare the derived constraints obtained from our model to the input IFMR. We first choose a test set of parameters for our IFMR, and then generate a mock sample of 20 wide DWDs. Table 4.6 summarizes the distributions these mock data are drawn from.

The first WD in the pair is randomly assigned a mass from a truncated Gaussian distribution. The second WD's mass is then obtained based on a mass ratio, q , randomly generated from another Gaussian distribution. We determine M_i using the model IFMR, and then the pre-WD lifetimes for each WD with the function shown in Figure 4.12.

τ_{cool} for the less-massive, slower-evolving WD is selected from a flat distribution in log space between 10 Myr and 1 Gyr. Following Equation 4.2, we then assign the more massive WD the τ_{cool} of its companion plus the difference in pre-WD lifetimes.

The WDs are then “observed.” Masses and cooling ages are randomly selected from Gaussian distributions centered on the true (mock) values, with standard deviations of $0.03 M_{\odot}$ in WD mass and 10% in τ_{cool} (these uncertainties are typical of WD spectral fits).

Table 4.6. Mock Data Parameters

Parameter	Input Distribution	Range
M_1	$\mathcal{N}(\mu = 0.75 M_\odot, \sigma = 0.15 M_\odot)$	(0.6, 1.2)
q	$\mathcal{N}(\mu = 1.0, \sigma = 0.15)$	(0.45, 1.0)
$\log \tau_2$	\mathcal{U}	(7.0, 9.0)
Mock IFMR Parameters		
Θ_{IFMR}	(0.1, 0.1, 0.38, 0.05)	

Note. — \mathcal{N} is a Gaussian distribution with mean μ and standard deviation σ . \mathcal{U} is the uniform distribution. The range dictates where the distributions are truncated. The model parameters, Θ_{IFMR} are defined in Equation 4.23. Observational uncertainties of $0.03 M_\odot$ are assigned to M_{WD} and 10% to τ_{cool} .

Finally, the observed WD masses and τ_{cool} and their associated uncertainties are used as inputs for our Bayesian model.

We use 32 separate chains in `emcee`, running for 10,500 steps, the first 500 steps are a “burn-in,” which we throw away then check to make sure the chains have converged. Figure 4.15 shows our input model (red) and 50 randomly drawn samples (gray) from the posterior distribution of model parameters. Importantly, the posterior samples are evenly distributed around the input IFMR. The spread in the posterior samples indicate the constraints these mock systems place on the IFMR.

Figure 4.16 shows the covariances between the four IFMR parameters in our model. Our model, for this particular combination of input parameters and mock wide DWDs, is able to constrain only certain regions of phase space. Figure 4.15 shows why; since there are no $<0.5 M_\odot$ WDs in the sample, our model is insensitive to the exact form of the first

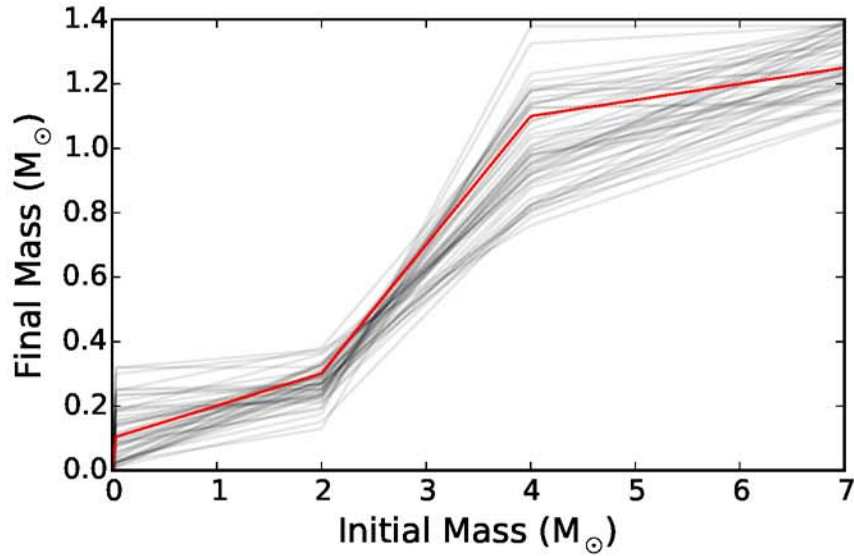


Figure 4.15 The input mock IFMR is shown in red, while samples from the posterior are semi-transparent in gray. The posterior samples are evenly distributed around the input distribution.

component in our piecewise linear model. Similarly, there are few $>1.0 M_{\odot}$ WDs in our sample, and the uncertainties in τ_{cool} estimates for these are of order the differences in the pre-WD lifetimes (however, these data can constrain ϕ_2 , the second piecewise linear component of our model). For the set of mock wide DWDs shown here, the constraints are most stringent between roughly 2 and 3 M_{\odot} .

The top panel of Figure 4.17 shows the covariance between the two model parameters describing the WD mass distribution. Although our model is too simple to exactly reproduce the input WD masses, the bottom panel shows that the posteriors from our model (lines) approximate the input WD mass distribution (histogram).

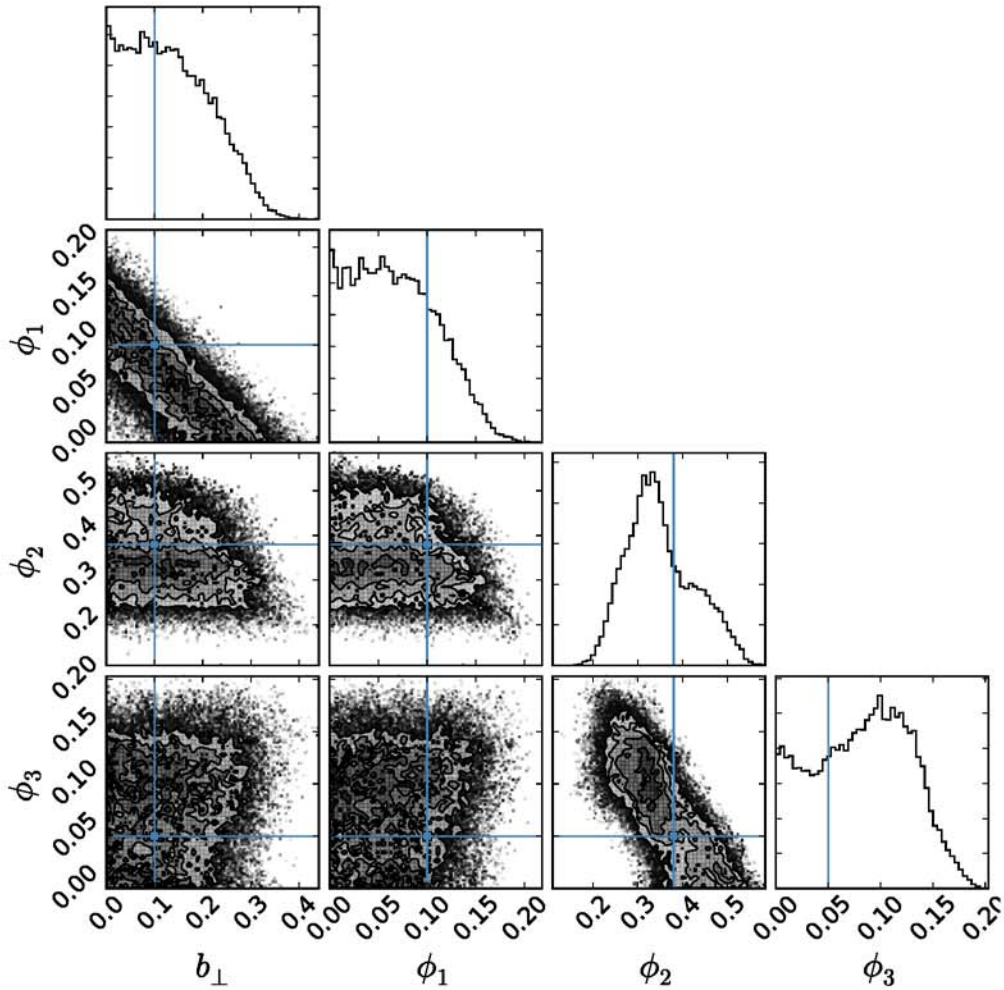


Figure 4.16 Covariances between the four parameters in Θ_{IFMR} in our model for our mock data set. Lines indicate the input values for our parameters. Our posterior distributions are centered around the input parameters, indicating that our model converged to the correct solutions.

4.4.5 Applying the Model to Wide DWDs

We applied our parametric model to our sample of wide DWDs using *emcee*. We check the 32 separate Markov chains to make sure they have converged. Here again, we throw away the first 500 steps and run the model for another 5000 steps. Figure 4.18 shows selected samples from the posterior distribution of model parameters. The posterior

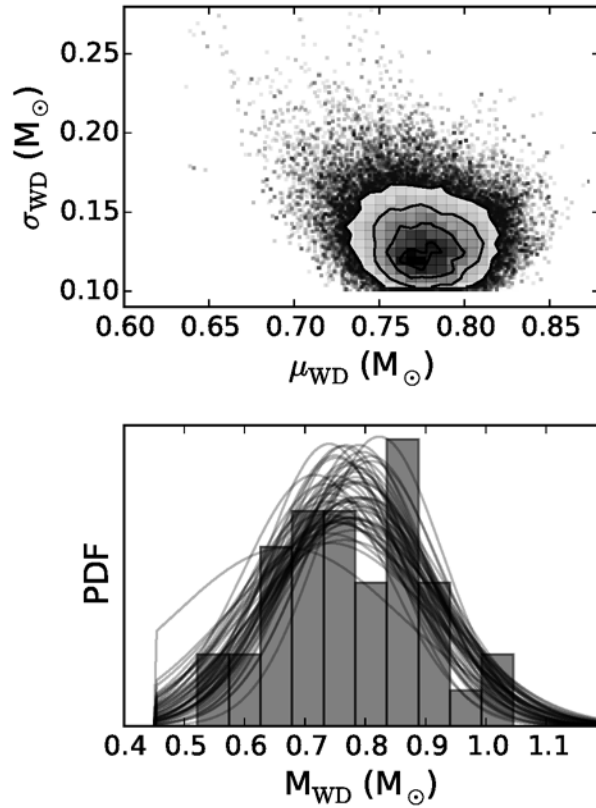


Figure 4.17 The top panel shows the covariance between the WD mass distribution model parameters μ_{WD} and σ_{WD} for our mock data set. The bottom panel shows a normalized histogram of the WD masses in our test sample. Lines show samples from the posterior distribution of model parameters.

samples converge between 2 and 4 M_{\odot} .

Reassuringly, this mass range corresponds to $\approx 0.5\text{--}0.8 M_{\odot}$ WDs, roughly the masses of the WDs in our sample (see Table 4.4). Smaller M_i produce WDs too low-mass to be found in our sample, and our method is not as sensitive to the small differences in the pre-WD lifetimes of more massive stars.

The covariances between the different model parameters are shown in Figure 4.20. These confirm that the parameters have converged. In particular, the slope of the second

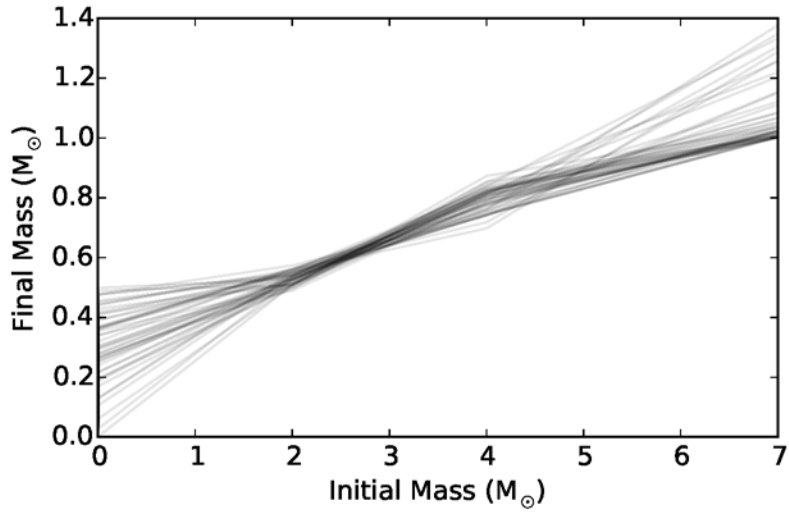


Figure 4.18 Samples from the posterior distribution for our fiducial model are semi-transparent in gray. The model converges for the second linear component ($M_i = 2\text{--}4 M_\odot$), but diverges outside of this mass range.

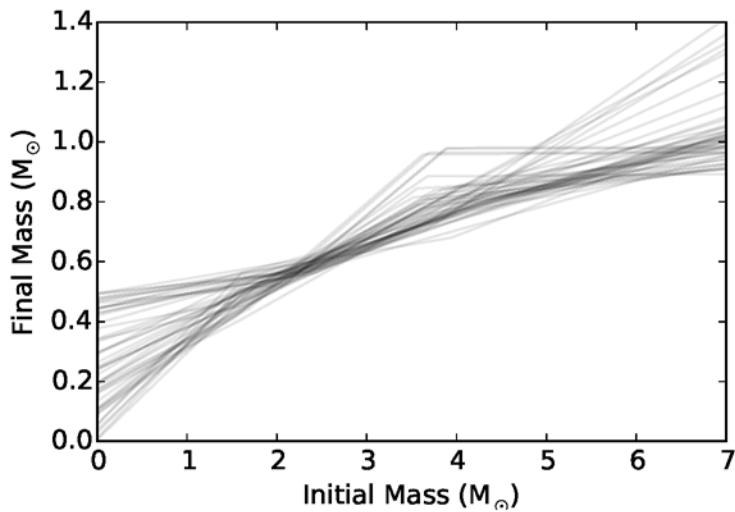


Figure 4.19 Samples from the posterior distribution for our eight parameter model in which the pivot points for our three component piecewise model are allowed to vary. The results are consistent with the four parameter model: our DWDs constrain the IFMR between $\approx 2\text{--}4 M_\odot$.

piecewise linear component of our model, ϕ_2 , is well constrained, and the covariance between b_\perp and ϕ_1 indicates that the model is well constrained near the pivot point at $M_i = 2 M_\odot$.

4.4.6 A Test of the Number of Model Parameters

To test the dependence of our results on our model, we extend our model by allowing the pivot points to vary. We then have a model with eight parameters: μ_{WD} , σ_{WD} , ϕ_1 , ϕ_2 , ϕ_3 , b_\perp , $M_{p,1}$, and $M_{p,2}$. We keep the same priors on the first six parameters in Equations 4.18, 4.24, and 4.25, and add flat priors on the pivot masses:

$$\begin{aligned} M_{p,1} &\in [1.5, 2.5] \\ M_{p,2} &\in [3.5, 4.5]. \end{aligned} \tag{4.26}$$

Figure 4.19 shows the results when we apply this eight-parameter model. Even with this more flexible model, the posterior distribution converges to a narrow distribution in M_{WD} for $M_i = 2\text{--}4 M_\odot$, suggesting that this convergence is not a result of our original choice to fix the pivot points.

In model parameter space, however, the masses at which the IFMR pivots do not converge. This can be seen in Figure 4.19: the pivot points vary across the whole allowed range. Perhaps with a future, larger data set, this model will be able to constrain $M_{p,1}$ and $M_{p,2}$, but the current sample of wide DWDs cannot.

Because our original four-parameter model reasonably represents the constraints

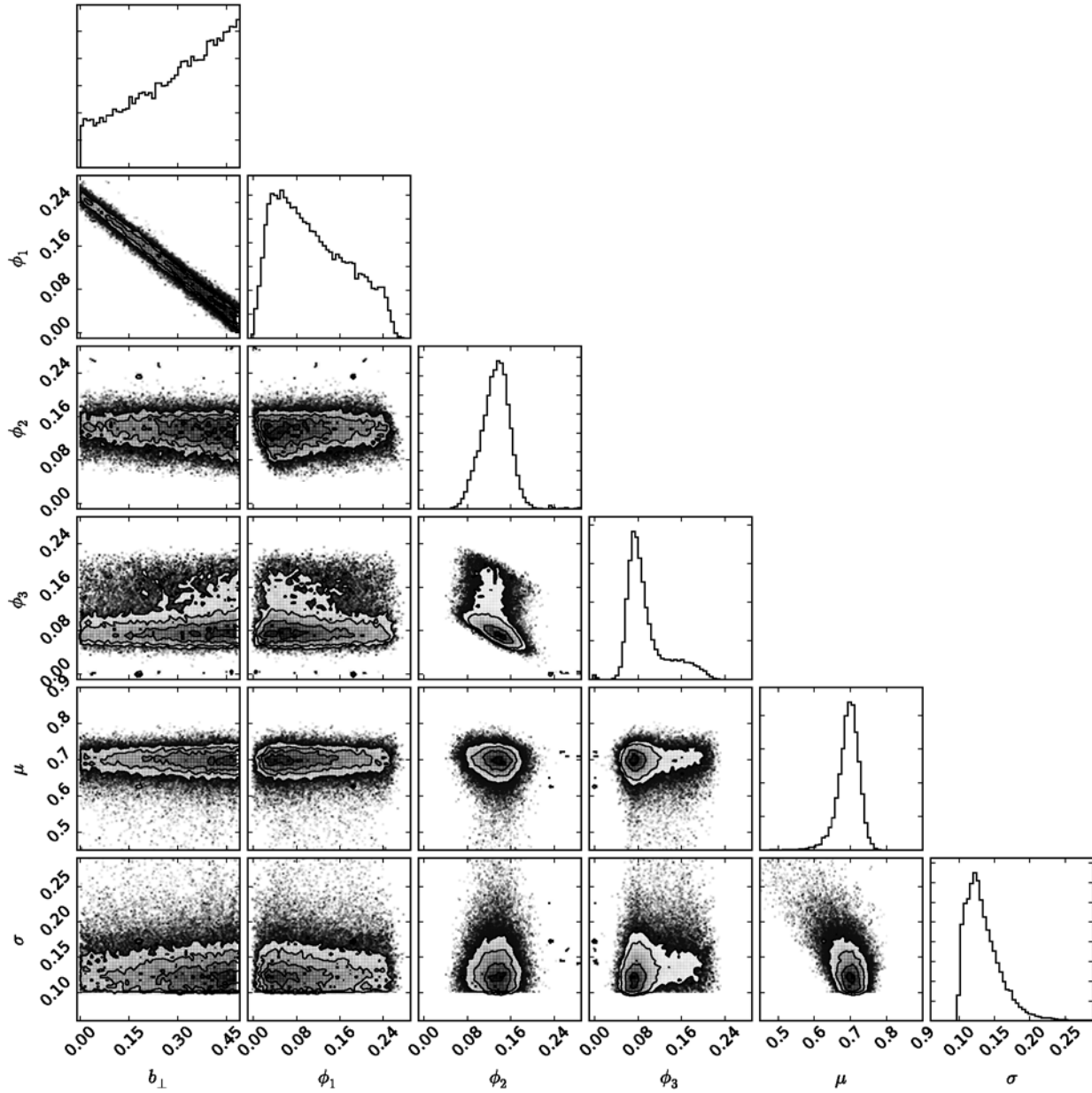


Figure 4.20 Covariances of the model parameters for our model applied to our sample of wide DWDs.

from our DWD sample and provides convex solutions, we choose that model as our fiducial model for the remainder of our analysis.

4.5 Discussion

4.5.1 Comparison to Theoretical Predictions

While stellar evolution codes still disagree significantly on the functional form of the IFMR, major divergences typically occur after the first thermal pulse, and codes generally produce similar core masses at the 1TP (Kalirai et al. 2014). Furthermore, one of the primary expectations from theory is that the core mass will not diminish on the TP-AGB (e.g., Karakas et al. 2002). This provides a significant sanity check for any observationally derived IFMR: for a given M_i , the resulting WD should be at least as massive as the 1TP core mass.

We compared samples from the posterior distribution from our fiducial model to the 1TP core masses obtained from the theoretical relations of Dominguez et al. (1999), Weiss & Ferguson (2009), and Kalirai et al. (2014). Reassuringly, between 2 and 4 M_{\odot} , our fiducial model constrains the IFMR to be above these relations.

Evolving from the 1TP to produce a WD is computationally challenging. The pulses that give the TP-AGB phase its name are due to thermal instabilities in the helium-burning shell of the AGB star (Schwarzschild & Härm 1965). These pulses are suspected to form a temporary convective zone within the He inter-shell region. This leads to the so-called third dredge-up, in which the convective envelope extends into the inter-shell region,

mixing heavier elements into the outer envelope (Iben 1975). This sequence of successive dredge-up events and overshooting naturally explain the observed C abundances in AGB stars (cf. discussion in Herwig 2000).

Although convective overshooting has been seen in three-dimensional numerical simulations, such calculations are currently only possible for small regions of a stellar atmosphere over small timescales (e.g., Freytag et al. 2012). For now, stellar evolution predictions are typically limited by the ability of 1D models, which rely on some form of mixing-length theory (Böhm-Vitense 1958) combined with a prescription for convective overshooting (cf. Herwig 2000, and references therein), to calculate accurately the energy transport during these pulses. This can cause problems. For example, 1D approximations can lead to large radiation pressures developing at the base of the convective envelope, which can in turn lead to unphysically large (supersonic) radial velocities. One way to deal with this involves decreasing the opacity profiles by hand in these regions (e.g., Renedo et al. 2010; Pignatari et al. 2013).

With these caveats in mind, we present in Figure 4.21 three IFMRs produced by different stellar evolution codes; the major differences between them stem from the treatments of dredge-up and wind mass loss. Renedo et al. (2010) argue, based on the theoretical results of Canuto (1998) and observations of *s*-process abundances by Lugaro et al. (2003), that the third dredge-up should be suppressed. In this scenario, the He core grows continuously, its mass only limited by the reduction of the envelope due to stellar winds, as described using the prescription of Vassiliadis & Wood (1993).

The Kalirai et al. (2014) IFMR uses the AGB models of Marigo et al. (2013), which

improve the treatment of the onset of the third dredge-up and the calculation of opacities. However, the resulting IFMR is still dependent upon a prescriptions for the dredge-up efficiency (Kalirai et al. (2014) use the prescription of Karakas et al. 2002) and the wind mass loss. Kalirai et al. (2014) calibrate their prescriptions by defining ignorance parameters and then finding the best fit ignorance parameters to match the observed open cluster constraints.

Finally, Weiss & Ferguson (2009) use the exponential overshooting prescription of Herwig et al. (1997). On the AGB, these authors use the wind mass loss prescription of Wachter et al. (2002) for C-rich AGB stars and the prescription of van Loon et al. (2005) for O-rich AGB stars. The Weiss & Ferguson (2009) simulations show little core growth on the TP-AGB, resulting in less massive WDs for a given M_i compared with the models produced by Renedo et al. (2010) and Kalirai et al. (2014).

Figure 4.21 includes our posterior samples with these three theoretical IFMRs. For $M_i = 2-4 M_\odot$, our model converges to a region of parameter space that suggests that the IFMR may lie between the higher final-mass models of Renedo et al. (2010) and Kalirai et al. (2014) and the lower final-mass model of Weiss & Ferguson (2009). We may not yet be able to place stringent constraints on wind-mass-loss models and dredge-up efficiencies with the available data, but Figure 4.21 suggests that DWDs may eventually provide important new observational tests for stellar evolution codes.

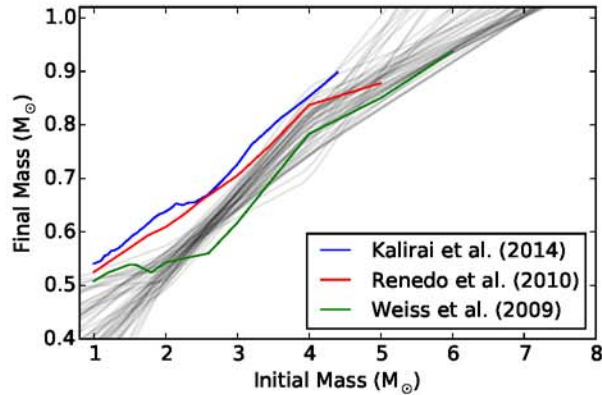


Figure 4.21 A comparison between samples from the posterior distribution from our fiducial model (gray lines) and theoretical IFMRs obtained from three separate stellar evolution codes. The differences between the codes are due primarily to treatment of the dredge-up and wind mass loss.

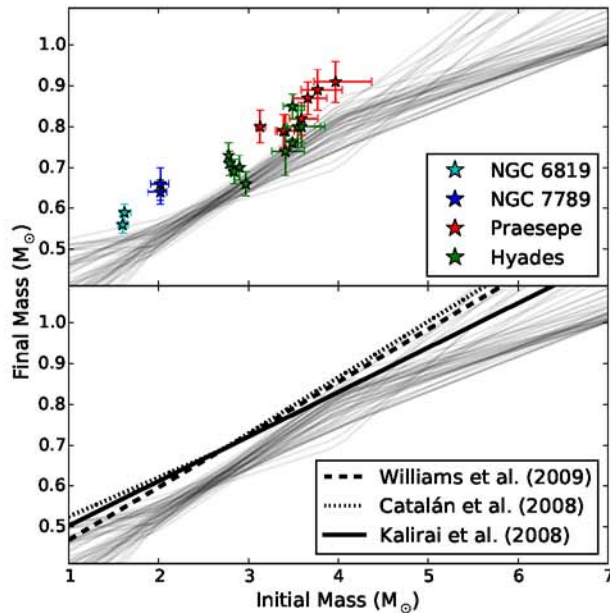


Figure 4.22 The top panel shows samples from the posterior distribution for our model (gray lines) and the observational constraints generated by WDs in four older open clusters (from Kalirai et al. 2014). The bottom panel compares the same posterior samples to the semi-empirical linear fits of Catalán et al. (2008a), Kalirai et al. (2008), and Williams et al. (2009).

4.5.2 Comparison to Other Observational Constraints

The most commonly used method for constraining the IFMR is that pioneered by Sweeney (1976). Here, the WDs are members of open clusters for which reliable ages can be obtained from e.g., isochrone fitting. There are at least two important limitations to consider when discussing this method. The first is that even for the nearby, well-studied open clusters that are generally used in these studies, significant disagreements about the stars' ages are not unusual. Furthermore, the techniques employed to obtain these ages differ, so that the constraints on the IFMR depend on different sets of systematic effects.

The second is that most easily accessible open clusters are young, with ages $\ll 1$ Gyr, so that only the most massive stars have evolved off the Main Sequence. There are four notable exceptions: NGC 6819, NGC 7789, the Hyades, and Praesepe are all old enough for their $\approx 2\text{--}4 M_{\odot}$ members to have evolved into WDs. Kalirai et al. (2014) recently re-analyzed 18 WDs in these four clusters using improved WD atmospheric models. These data are shown in the top panel of Figure 4.22. Our results are consistent with those derived from WDs in the Hyades, but the initial masses for WDs in NGC 7789 and Praesepe are systematically lower than our posterior samples.¹¹

Various authors have pointed out that metallicity could lead to a natural spread in the IFMR (e.g., Kalirai et al. 2005). However, the four clusters hosting the WDs in Figure 4.22 all have near-solar metallicities,¹² while we also expect the DWDs in our sample to have roughly solar metallicity (see Section 4.4.1.2). While Meng et al. (2008) and Romero et al.

¹¹We ignore the WDs in NGC 6819, since these evolved from $< 2 M_{\odot}$ stars, outside the mass range to which we are sensitive.

¹²NGC 6819: $[\text{Fe}/\text{H}] = -0.02 \pm 0.02$ (Lee-Brown et al. 2015); NGC 7789: $+0.03 \pm 0.07$ (Overbeek et al. 2015); Praesepe: $+0.16 \pm 0.05$ (Carrera & Pancino 2011); Hyades: $+0.11 \pm 0.01$ (Carrera & Pancino 2011).

(2015) showed that metallicity-dependent mass-loss rates can result in WDs with masses varying by as much as $0.2 M_{\odot}$, the range is principally due to cases of extremely low or high metallicities. For metallicities near solar, variations in $M_{\text{WD}} \lesssim 0.05 M_{\odot}$ (see figure 1 in Meng et al. 2008 and figure 4 in Romero et al. 2015). Metallicity differences are therefore unlikely to explain the discrepancy between our constraints and the WDs in these open clusters.

Instead, the difference could stem from uncertainties in the cluster ages. Kalirai et al. (2014) followed Claver et al. (2001) in adopting the *Hipparchos*-derived Hyades age of 625 Myr (Perryman et al. 1998) for Praesepe.¹³ By contrast, when fitting metallicity-specific isochrones to Praesepe, Salaris et al. (2009) found an age ranging from ≈ 450 –650 Myr. The inclusion of convective overshooting, which extends stellar lifetimes, accounts for the difference. If, instead of 625 Myr, the Hyades and Praesepe are 550 Myr, the corresponding data points in Figure 4.22 would all shift right, toward higher M_i , by ≈ 0.2 – $0.3 M_{\odot}$. These constraints would then be consistent with samples from our posterior distribution.¹⁴

The discrepancy with the two WDs in NGC 7789 could also be due to an inaccurate cluster age. Kalirai et al. (2014) adopt the age of 1.4 Gyr obtained by Kalirai et al. (2008) from isochrone fits. However, isochrone-derived ages for this cluster vary noticeably in the literature, ranging from 1.1 Gyr (Mazzei & Pigatto 1988) to 1.6 Gyr (Gim et al. 1998). A modestly younger age of 1.2 Gyr for NGC 7789 increases the derived M_i by $\approx 0.2 M_{\odot}$, enough that these data also become consistent with samples from our posterior

¹³For a recent discussion of the evidence that the two clusters are indeed the same age, see Douglas et al. (2014).

¹⁴Brandt & Huang (2015) recently argued that if stellar models accounting for rotation are used in the isochrone fitting, both clusters are ≈ 800 Myr, illustrating just how much uncertainty remains about the age of two of the nearest, best-studied open clusters.

distribution.

There are a number of other possibilities for the difference we see in Figure 4.22. Our piecewise-linear model might be inappropriate because there is significant structure in the IFMR for $M_i = 2\text{--}4 M_\odot$. Some of the WDs in either the open cluster or wide DWD data may have unresolved binary companions that affected their evolution, and therefore should not be used to constrain the IFMR. To identify the source(s) of this discrepancy, progress needs to be made with both methods: we need more complex models than that presented here for the IFMR, combined with larger sets of wide DWDs, as well as new WDs in older open clusters.

The bottom panel of Figure 4.22 shows that our posterior samples lie significantly below the semi-empirical IFMRs of Catalán et al. (2008a), Kalirai et al. (2008), and Williams et al. (2009). These authors use somewhat different WD samples and spectroscopic solutions in generating their linear fits, but for $M_i = 2\text{--}4 M_\odot$, the constraints are obtained predominantly with the WDs shown in the top panel of Figure 4.22.

Considering the uncertainties in the ages of the clusters hosting these WDs, we suggest that these semi-empirical relations be used with caution for $M_i = 2\text{--}4 M_\odot$. We make samples from the posterior distribution from our model available for use within this M_i mass range.

4.6 Conclusions

In an effort to provide new, independent constraints on the IFMR, we began by conducting a comprehensive search for wide DWDs in the SDSS DR9 photometric catalog. Using two

separate methods, we identified 65 new candidate systems. By combining these pairs with those already in the literature, we assembled a sample of 142 candidate and confirmed wide DWDs.

To confirm the WD nature of the stars in these pairs, and to obtain accurate mass and τ_{cool} measurements for them, we engaged in a spectroscopic campaign using the 3.5-m APO telescope (and also collected spectra from the literature). Our targets included new systems identified in Andrews et al. (2012), those photometrically selected from DR9, and literature pairs that lacked spectroscopy. The contamination by non-WDs was extremely low: only one of the 97 objects for which we obtained spectra was not a WD. Fitting WD model atmospheres to our spectra gave us $\log g$ and T_{eff} values; these were then converted to M_{WD} and τ_{cool} for each star.

In addition to 27 DA/DA pairs, our campaign identified a number of interesting systems that cannot be used to constrain the IFMR. We confirmed the nature of the second known DA/DB system, SDSS J0849+4712 (CDDS15), and identified SDSS J2355+1708 as the third DA/DB DWD. DBs may evolve from H-deficient post-AGB stars (Althaus et al. 2005), and it is unclear whether the same IFMR applies to these stars as to DA WDs and their progenitors. We found four new DC WDs with DA companions (we also confirm the nature of another previously identified DA/DC system); the lack of absorption features makes it impossible to determine the mass of the DCs from spectra alone. We identify four new candidate DA/DAH pairs, and confirm the nature of three previously known systems; the DAH spectra cannot be fit with DA atmospheric models, and in general require higher-resolution and/or better S/N spectra to confirm their nature.

Finally, we identify two candidate triple systems: PG 0901+140 (based on the anomalously low mass of one of its components, this system could be triple degenerate) and J2047+0021B (which was previously identified by Silvestri et al. (2006) as an unresolved DQ+K7 binary). Because of the potential for mass transfer in the unresolved pair, candidate triple systems such as these had to be excluded from our efforts to constrain the IFMR.

We divided our double DAs into high- and low-fidelity pairs, labeling the DWDs with mass uncertainties $>0.1 M_{\odot}$ in at least one WD as low-fidelity. These pairs have spectra good enough to identify objects as DAs, but too poor to obtain accurate fits to model atmospheres. We also considered the spectroscopic distances to each WD in these candidate DWDs, and designated pairs with a distance difference $>25\%$ as low-fidelity. Finally, we removed from our high-fidelity sample DWDs for which the more massive WD appeared to have a shorter τ_{cool} than its less-massive companion, as this goes against standard expectations from stellar evolution. Combining our high-fidelity pairs with DWDs from Baxter et al. (2014) for which we lacked spectroscopic data, we obtained a sample of 19 DWDs with which to constrain the IFMR.

Because the members of wide binaries are co-eval and evolve independently (i.e., without mass transfer affecting their evolutionary pathways), the age of each WD in a DWD is the same and is the sum of each WD's τ_{cool} and pre-WD lifetime. Using this as a starting point, we developed a hierarchical Bayesian framework that tests the likelihood that any particular IFMR accounts for the observed masses and cooling ages, and corresponding uncertainties, of a wide DWD. We then constructed a parametrized

form of the IFMR, choosing a continuous, piecewise-linear function with pivot points at 2 and $4 M_{\odot}$. We also included a model for the underlying WD mass distribution, which we varied simultaneously with the IFMR parameters.

We first tested our model on a set of mock wide DWDs and successfully recovered our input IFMR. We then applied our model to our 19 high-fidelity DWDs, using a Markov Chain Monte Carlo approach to find the region of parameter space implied by the data. The resulting constraints are comparable to previous constraints on the IFMR obtained using WDs in open clusters. However, our results produce larger M_i than previous observations (or alternatively, we found that stars of a given M_i produce less massive WDs). Importantly, our constraints are most sensitive to $M_i = 2\text{--}4 M_{\odot}$, a regime that the open cluster data have difficulty testing. We found no improvement when we tested an expanded model in which the pivot points vary; our original model with fixed pivot points is sufficient to describe our current set of DWDs.

Our model can be expanded to include other constraints, including those from open cluster WDs, globular cluster WD cooling tracks, and Sirius-like binaries. Because each of these methods has their own associated systematic uncertainties, including these in a statistically responsible way is not straightforward, however.

Our three-component, piecewise linear model is only an approximation for the true, physical IFMR. Ultimately, we would like to be able to constrain physically meaningful stellar evolution parameters. Kalirai et al. (2014) recently performed such an analysis using the WDs presented in Figure 4.22. Our method here could similarly be expanded to constrain stellar evolution directly. For example, the form of the IFMR within the $M_i = 2\text{--}4$

M_{\odot} range is sensitive to physics on the TP-AGB. DWD data may be precise enough to place important constraints on uncertain dredge-up and overshooting physics. We leave this to future work.

In our search for new DWDs, we relied on SDSS photometry combined with proper motion measurements to identify WD candidates, while masses and τ_{cool} were derived from fits to WD template spectra. With precision astrometry from the *Gaia* space telescope, identifying WDs and matching them with common proper motion companions will be significantly easier. Furthermore, as pointed out by Carrasco et al. (2014), data from the BP and RP spectrophotometers, combined with distance measurements and a mass-radius relation, will provide T_{eff} and M_{WD} for every WD identified. These authors estimate *Gaia* will find some 250,000 to 500,000 WDs. We do not know the space density of wide DWDs in the Galaxy, but it is hard to escape the conclusion that *Gaia* will identify hundreds to thousands of new wide DWDs. With a measured T_{eff} and M_{WD} for the WDs in each of these pairs, these wide DWDs will potentially revolutionize our understanding of the IFMR.

4.7 Appendix

Our spectroscopic campaign uncovered a number of interesting DWDs that could not be used to constrain the IFMR. These include two systems in which a DA is paired with a DB WD, which is a WD lacking an optically thick H layer and with $T_{\text{eff}} \gtrsim 12,000$ K. SDSS J0849+4712 (CDDS15) was previously identified by Baxter et al. (2014) as the second known DA/DB system after L 151-81 A/B (Oswalt et al. 1988). Here we report J2355+1708

as the third identified wide DA/DB DWD.

The DBs in these systems, SDSS J0849+4712B (CDDS15-A) and J2355+1708B, are shown in Figure 4.23. The fit results for these stars in Table 4.3 were provided by P. Bergeron (priv. communication). DBs probably form through a different channel than DAs. They may evolve from H-deficient post-AGB stars (Althaus et al. 2005), and it is unclear whether the same IFMR applies to these stars.

As DBs cool to $T_{\text{eff}} \lesssim 12,000$ K, they can no longer ionize He. They are then known as DC WDs and characterized by their featureless blackbody spectra. The lack of absorption features makes it impossible to determine the mass of these DC WDs from spectra alone. We identify four DC WDs in our sample: LP 549-32, J0029+0015A (CDDS2), J0344+1510A, and J1544+2344B. GD 559 was previously identified as a DA/DC wide pair by Farihi et al. (2005). Due to their cool temperatures, the spectra of these objects generally have a low S/N.

Magnetic DAs (DAHs) are identified by Zeeman splitting in the Balmer lines. We have identified four new candidate DAHs: J0002+0733B, J1314+1732A, J1412+4216B, and J2044+4030A. We also confirm the DAH nature of three previously identified DAH WDs in wide pairs: PG 1258+593B (Girven et al. 2010), J0748+3025 (CDDS11 Dobbie et al. 2013; Baxter et al. 2014) J2259+1404B (CDDS52 Baxter et al. 2014). Spectra for several of these are shown in Figure 4.23. Since DA atmospheric models cannot be used here, we only include spectroscopic fits to the DAHs' companions in Table 4.7.

We label the DA/DC and DA/DAH systems as candidates in Table 4.7 because higher-resolution and/or better S/N spectra are required to confirm the nature of the non-DAs in

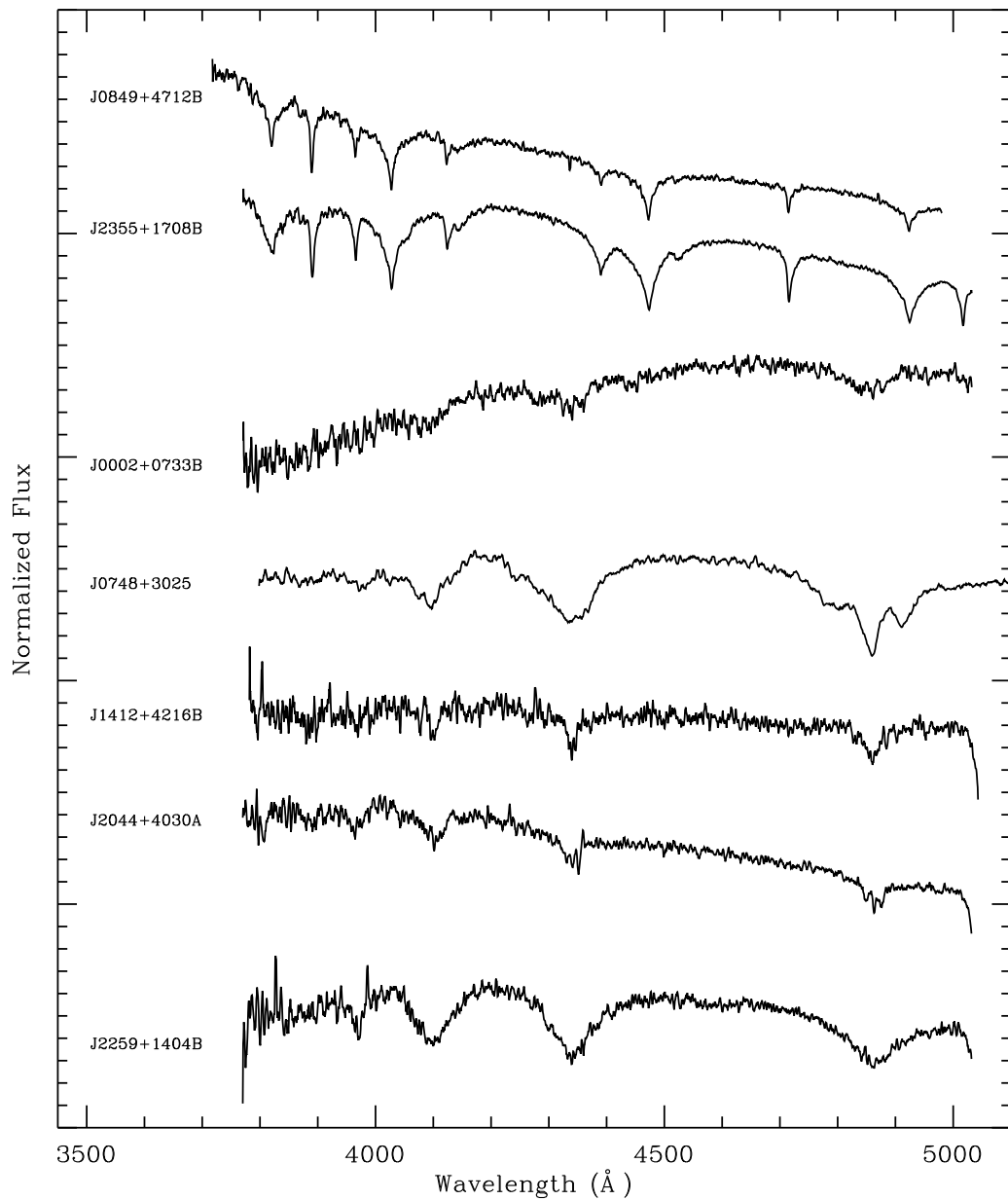


Figure 4.23 The two top spectra are for the DBs in our sample: J0849+4712B (CDDS15-A) and J2355+1708B. The other spectra are for five DAHs: J0002+0733B, J0748+3025, J1412+4216B, J2044+4030A, and J2259+1404B. We do not include the SDSS spectra for PG 1258+593B and J1314+1732A, which show Zeeman splitting in the $H\alpha$ line, but not in the higher order Balmer lines.

these pairs.

The “B” component of the wide DWD J2047+0021B was identified by Silvestri et al. (2006) as a carbon atmosphere WD (DQ) with a K7 companion. This would make it the second such triple system composed of two WDs and a K star, after CDDS30 (Baxter et al. 2014). We list J2047+0021 as a candidate triple system in Table 4.7.

Finally, while it is possible to form single WDs with masses as low as $0.45 M_{\odot}$ (Kilic et al. 2007), observations of WDs with $M_{\text{WD}} < 0.45 M_{\odot}$ indicate a binary fraction $\gtrsim 80\%$ (Brown et al. 2011a), suggesting that the low-mass WDs in several of our systems are in fact unresolved binaries. These systems are listed as candidate triple systems in Table 4.7. This list includes the two known systems, G 21-15 (Farihi et al. 2005) and Gr 576/577 (Maxted et al. 2000), which are hierarchical triples composed of a close pair of WDs with a degenerate tertiary body in a larger orbit. In both systems, our spectroscopic fits return $\approx 0.45 M_{\odot}$ for the unresolved close pair. Additionally, PG 0901+140A (with $M_{\text{WD}} = 0.47 \pm 0.04 M_{\odot}$) may be an unresolved degenerate pair. Because of the potential for mass transfer in the unresolved pairs, these systems cannot be used to constrain the IFMR and were excluded from our analysis. We note here that our spectroscopic solutions for PG 0901+140 differ substantially from those of Farihi et al. (2005), who find that both WDs in the system are approximately $0.8 M_{\odot}$.

For completeness, we also include in Table 4.7 those systems for which we had only one spectrum and our one spectroscopic contaminant, the DA/A-star pair SDSS J2124–1620.

Table 4.7: Fit Results for the non-DA/DA Spectroscopic Sample

Name	Telescope	# of Fitted Balmer Lines	WD Type	S/N ^a	T _{eff} (K)	log g	Distance (pc)	M _{WD} (M _⊙)	τ _{cool} (Myr)
DA/DB Systems ^b									
J0849+4712A	APO	6	DA	28	11720±210	8.05±0.06	152±7	0.635±0.036	425±41
J0849+4712B	APO	...	DB	...	17480±310	8.08±0.06
J2355+1708A	APO	5	DA	23	10160±160	8.31±0.07	131±7	0.797±0.045	927±109
J2355+1708B	APO	...	DB	...	21470±440	8.12±0.03
Candidate DA/DAH Systems ^c									
PG 1258+593A ^d	DA	...	15160±240	8.00±0.05	65	0.61±0.03	...
PG 1258+593B	SDSS	...	DAH
J0002+0733A	APO	...	DA
J0002+0733B	APO	...	DAH
J0748+3025 ^e	SDSS	...	DAH
J1314+1732A	SDSS	...	DAH
J1314+1732B	APO	6	DA	50	12530±210	8.04±0.05	84±3	0.631±0.029	352±29
J1412+4216A	APO	6	DA	104	15420±240	8.12±0.05	79±3	0.686±0.027	220±19
J1412+4216B	APO, SDSS	...	DAH
J2044+4030A	APO	...	DAH
J2044+4030B	APO	6	DA	107	13590±240	8.00±0.05	61±2	0.607±0.026	264±22
J2259+1404A	APO	5	DA	48	25200±390	8.68±0.05	103±5	1.042±0.028	137±15
J2259+1404B ^e	APO	...	DAH
Candidate DA/DC Systems ^c									
LP 549-32	APO	...	DC
LP 549-33	SDSS	5	DA	54	6660±110	7.84±0.10	31±2	0.499±0.052	1370±179
LP 549-33	APO	5	DA	50	7090±110	8.41±0.09	24±2	0.855±0.057	3342±424
GD 559A	APO	7	DA	51	18720±290	8.14±0.05	69±3	0.701±0.028	121±13
GD 559B	APO	...	DC
J0029+0015A	SDSS	...	DC
J0029+0015B	SDSS	6	DA	33,17	9960±150	8.08±0.06	167±8	0.648±0.036	682±65
J0344+1510A	APO	...	DC
J0344+1510B	APO	6	DA	36	8300±130	7.92±0.09	64±4	0.547±0.048	871±104
J1544+2344A	SDSS	5	DA	15	9470±180	7.97±0.13	162±14	0.581±0.075	668±121
J1544+2344B	SDSS	...	DC
Candidate Triple Systems									
G 21-15 ^f	VLT	7	DA+DC	10,24,10,22	14460±210	7.66±0.04	41±2	0.448±0.018	244±10
Gr 577	APO	7	DA+DA	85	9390±130	7.74±0.05	29±1	0.461±0.023	986±33
Gr 576	APO	7	DA	73	14240±270	8.09±0.05	39±1	0.665±0.027	265±23
PG 0901+140A	APO	6	DA+DA?	67	9100±140	7.78±0.08	59±3	0.474±0.041	585±57
PG 0901+140B	APO	6	DA	39	8120±120	7.89±0.07	58±3	0.531±0.039	886±87
J2047+0021A	SDSS	5	DA	51	14330±300	8.03±0.05	140±5	0.627±0.028	236±23

Continued on next page

Table 4.7 – Continued from previous page

Name	Telescope	# of Fitted Balmer Lines	WD Type	S/N ^a	T_{eff} (K)	$\log g$	Distance (pc)	M_{WD} (M_{\odot})	τ_{cool} (Myr)	
J2047+0021B [§]	SDSS	...	DQ+K7	
Systems With Only One Spectrum										
J0000–1051A	SDSS	5	DA	13	8590±180	8.03±0.19	161±21	0.614±0.111	933±256	
J0117+2440B	SDSS	6	DA	12	17730±670	8.26±0.11	472±41	0.777±0.070	183±42	
J0139+1447A	SDSS	4	DA	7	8740±250	8.29±0.31	186±49	0.779±0.200	1316±880	
J0754+4950A	SDSS	4	DA	6	6710±340	7.39±0.82	133±55	0.328±0.326	1603±1090	
J1254–0218A	SDSS	7	DA	92	17260±260	8.11±0.05	120±5	0.681±0.027	151±14	
J1254–0218A	VLT	5	DA	8, 8	15510±250	7.97±0.05	119±4	0.598±0.027	170±16	
J2115–0741A	SDSS	5	DA	27	8090±130	8.13±0.09	68±5	0.675±0.057	1264±198	
J2332+4917A	SDSS	6	DA	20	18490±450	7.99±0.07	400±21	0.614±0.041	93±17	
Contaminants ^h										
J2124–1620A	APO	...	non-WD	
J2124–1620B	APO	5	DA	19	10290±180	8.06±0.09	127±8	0.640±0.055	611±85	

^a Objects with more than one listed S/N indicate multiple spectra were used to fit for the WD parameters.

^b The DB WDs in our spectroscopic sample were fit by P. Bergeron (pers. communication).

^c Confirming the nature of the non-DA WDs in these pairs requires higher S/N spectra.

^d Spectroscopic data for PG 1258+593A were taken from Gianninas et al. (2011). For a detailed discussion on this system see Girven et al. (2010).

^e J0748+3025 and J2259+1404 have already been identified as DA+DAH pairs (see Baxter et al. 2014, and references therein). J0748+3025 is composed of a pair of WDs separated by ≈ 15 . However, the SDSS spectrum shows three cores in H β ; see Figure 4.23.

^f Farihi et al. (2005) identified the companion to G 21-15 as a DC WD.

[§] Silvestri et al. (2006) identified J2047+0021B as an unresolved binary composed of a carbon atmosphere WD (DQ) with a K7 companion.

^h J2124–1620 is composed of a DA WD and an A star.

4.8 Acknowledgments

We thank the observing specialists for their help with the APO observations. We thank P. Bergeron for fitting the DB WDs in our sample and D. Koester for providing us with VLT spectra of several of the WDs discussed here. We thank Lars Bildsten, Silvia Catalán, Falk Herwig, David Hogg, Marcelo Miller Bertolami, Rodolfo Montez, Jr., and Adrian Price-Whelan for stimulating and helpful discussions. M.A.A., M.K., and A.G. gratefully acknowledge the support of the NSF and NASA under grants AST-1255419, AST-1312678, and NNX14AF65G, respectively.

This work made use of the *yeti* cluster at the Columbia University Shared Research Computing Facility, which is supported by NIH Research Facility Improvement Grant 1G20RR030893-01 and matching funds from New York State/the Empire State Development's Division of Science, Technology and Innovation (NYSTAR) under Contract C090171.

Funding for SDSS-III has been provided by the Alfred P. Sloan Foundation, the Participating Institutions, the National Science Foundation, and the U.S. Department of Energy Office of Science. The SDSS-III web site is <http://www.sdss3.org/>.

SDSS-III is managed by the Astrophysical Research Consortium for the Participating Institutions of the SDSS-III Collaboration including the University of Arizona, the Brazilian Participation Group, Brookhaven National Laboratory, University of Cambridge, Carnegie Mellon University, University of Florida, the French Participation Group, the German Participation Group, Harvard University, the Instituto de Astrofísica de Canarias, the Michigan State/Notre Dame/JINA Participation Group, Johns Hopkins Univer-

sity, Lawrence Berkeley National Laboratory, Max Planck Institute for Astrophysics, Max Planck Institute for Extraterrestrial Physics, New Mexico State University, New York University, Ohio State University, Pennsylvania State University, University of Portsmouth, Princeton University, the Spanish Participation Group, University of Tokyo, University of Utah, Vanderbilt University, University of Virginia, University of Washington, and Yale University.

Chapter 5

The Curious Case of HS 2220+2146

5.1 Introduction

Roughly half of all Galactic field stars are found in multiple systems, but only a fraction have small enough separations to interact. Using catalogs of nearby stars, Duquennoy & Mayor (1991) showed that the distribution of wide stellar binaries is well approximated by a Gaussian centered on an orbital period (P_{orb}) of 180 years. More recently, Dhital et al. (2010) used the Sloan Digital Sky Survey (SDSS; York et al. 2000) to identify binaries with separations as large as 10^5 AU. For $M \lesssim 8 M_{\odot}$, stars in such widely separated binaries never interact, independently evolving through the main sequence (MS) and giant branches and becoming white dwarfs (WDs).

Wide double WDs (DWDs), the evolutionary endpoints of these wide binaries, were first identified as common proper motion pairs in nearby proper motion catalogs (Sanduleak & Pesch 1982; Greenstein 1986b; Sion et al. 1991). Recently, systematic searches for

wide DWDs have used precision proper motion data from SDSS and statistically associated astrometrically close pairs of blue objects as wide DWDs (Andrews et al. 2012; Baxter et al. 2014). Our recent search applied both methods to data from SDSS Data Release 9 (Ahn et al. 2012), and brought the total number of candidate and confirmed wide DWDs to 142 (Andrews et al., in prep).

This sample includes two spectroscopically confirmed triple degenerate systems, Sanduleak A/B (Maxted et al. 2000) and G 021-15 (Farihi et al. 2005), and one candidate triple system, PG 0901+140 (Andrews et al., in prep). These triple systems are composed of an unresolved pair of WDs with a widely separated, visual WD companion. Reipurth & Mikkola (2012) argued that such hierarchical triple systems may be the natural evolutionary endpoint of newborn triple systems: the inner binary tightens while the outer companion's orbit expands. Triple degenerate systems form when all three stars evolve into WDs, with the inner binary surviving any phase of mass transfer or dynamical interaction it undergoes.

In some systems, however, the inner binary may merge first, reducing the triple to a wide binary. The eccentric Kozai-Lidov (EKL) mechanism allows the inner and outer binary of a hierarchical triple to secularly trade angular momentum, resulting in large oscillations in the inner binary's eccentricity and mutual inclination of the two orbital planes. Perets & Fabrycky (2009) first suggested that the EKL mechanism, combined with tidal dissipation, could cause the inner binary to merge, forming a blue straggler with a widely separated companion.

Naoz & Fabrycky (2014) expanded the EKL equations to include the octopolar term

and ran a suite of simulations evolving hierarchical triple systems to compare the systems that ended as stable triple systems with those in which the inner binary merged forming a blue straggler binary. They found the resulting blue straggler binaries had typical orbital periods of 10^2 - 10^4 yr. Crucially, such systems should then evolve into wide DWDs.

In our most recent search for wide DWDs (Andrews et al., in prep) we identified HS 2220+2146 as a curious DWD system. High-resolution Very Large Telescope (VLT; $R \approx 14,000$) spectra indicate that the more massive WD in this system has a higher temperature than its less massive companion. Since more massive MS stars evolve faster into more massive WDs, this cannot be explained through standard stellar evolution.

Recently, the more massive WD in the DWD SDSS J1257+5428 (Badenes et al. 2009; Marsh et al. 2011) was also shown to have a smaller cooling age than its companion (Bours et al. 2015). However, HS 2220+2146 is fundamentally different because it is very unlikely that mass transfer played a roll in its evolution. Here we show that HS 2220+2146 is consistent with having formed from a hierarchical triple in which the inner binary merged into a blue straggler.

Observations of blue stragglers in the open cluster NGC 188 show that a large fraction are found in binaries (Mathieu & Geller 2009). Geller & Mathieu (2011) found that the companions may in fact be WDs, and Gosnell et al. (2014) identified three blue stragglers with young WD companions. The widest orbital period binary, WOCS 4540, has a $P_{\text{orb}} = 3030 \pm 70$ days. These authors argue that although the binary is difficult to create via a standard Roche lobe overflow, it can be formed through accretion from the stellar wind of a binary.

HS 2220+2146, however, has a $P_{\text{orb}} \approx 10^3$ years, and is too wide to have formed a blue straggler through mass accretion. If our proposed formation scenario is correct, the progenitor to the more massive WD in HS 2220+2146 was the product of the merger of a close binary. HS 2220+2146 would then be the first DWD known to have formed through this evolutionary channel.

In Section 5.2 we demonstrate through both high-resolution spectra and gravitational redshift measurements that the hotter WD in HS 2220+2146 is indeed the more massive WD in the pair. We describe a possible formation history for this DWD in Section 5.3. We discuss the possibility of the EKL mechanism being responsible for merging the inner binary, and rule out the possibility of significant stellar wind accretion, in Section 5.4. We conclude in Section 5.5.

5.2 Observations

The two WDs in HS 2220+2146 were first identified as an associated system by Baxter et al. (2014). Using the astrometry from SDSS DR7 (Abazajian et al. 2009), these authors showed that the two WDs form a wide binary due to their close separation, their matching proper motion, and their similar derived distance moduli. In Andrews et al. (in prep) we recover this system as part of our search for wide DWDs in SDSS DR9.

Two separate spectra of each WD in the system were taken as part of the Supernova Progenitor survey (SPY; Koester et al. 2009) on 2002 September 25 and 26. Details of the data reduction can be found in that work, but we note here that the spectra were taken with the UVES spectrograph at the ESO VLT telescope and have a high resolution

of $R \approx 14,000$. We show the individual spectra in Figure 5.1 along with fits to model templates using the technique originally developed in Bergeron et al. (1992) and described in detail in Gianninas et al. (2011, and references therein). These solutions are based on one-dimensional models using a mixing length parameter $ML2/\alpha = 0.8$ (Tremblay et al. 2010, 2011a). The best fit T_{eff} and $\log g$ values from our spectral fits are given in Table 5.1 along with the corresponding WD masses (M_{WD}) and cooling ages (τ_{cool}).

We also fit archival spectra of both WDs taken with the GMOS instrument on Gemini-North using the B600 grating. We reduce these data using standard reduction techniques with pyraf’s gemini package. We applying the same WD models to the reduced spectra, and provide the derived T_{eff} and $\log g$ values in Table 5.1. These spectra provide an important consistency check since they were taken with different instruments and different spectral resolutions and are in close agreement with the spectral values derived using the VLT spectra.

According to standard stellar evolution theory, the initially more massive star in a pair should evolve into a more massive WD first. Since M_{WD} and τ_{cool} map roughly to $\log g$ and T_{eff} , one would expect that, for a coeval DWDs whose progenitors never interacted, the WD with the larger $\log g$ will be the cooler one. The spectral values in Table 5.1 indicate that, for HS 2220+2146, the opposite is true. Detailed fits to WD atmospheric models are necessary since more massive WDs have a smaller radius and therefore cool more slowly, but Table 5.1 confirms our basic intuition about this system: the *less* massive WD was born first.

This evolution could be explained by one of the WDs being in a close binary with

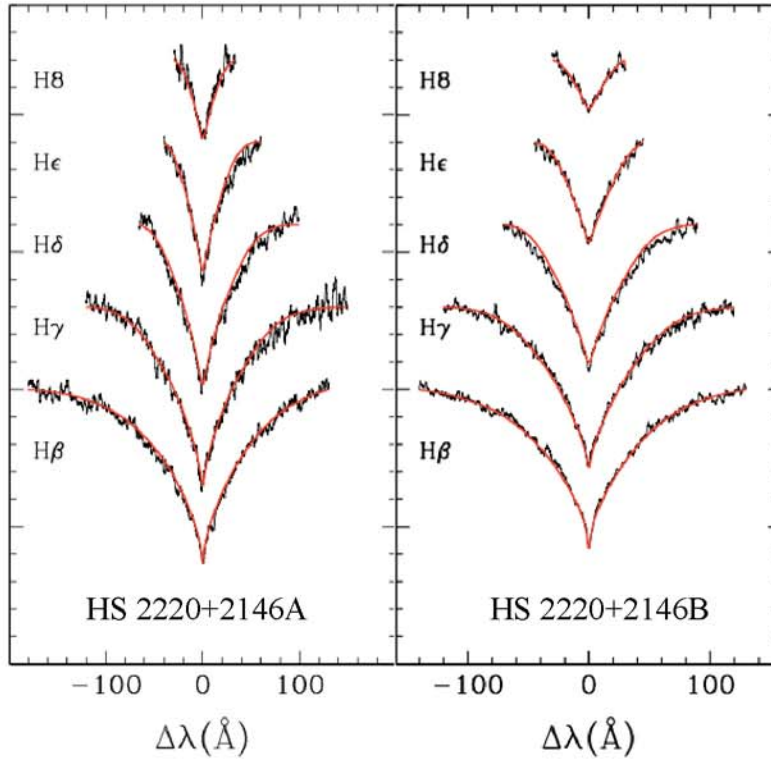


Figure 5.1 Balmer absorption lines from $H\beta$ to $H8$ and the corresponding best fit spectral templates (from Tremblay et al. 2011a) for HS 2220+2146A and HS 2220+2146B. Spectra were taken by the SPY survey using the VLT with $R \approx 14,000$ and boxcar averaged with a width of 20 elements. T_{eff} and $\log g$ values and the corresponding M_{WD} and τ_{cool} are given in Table 5.1.

another, unresolved star since mass transfer could have affected both the mass and cooling age of a WD. Only a late-type dwarf or brown dwarf could escape detection in the VLT spectra. In Figure 5.2, we compare the calculated spectral energy distribution (SED) derived from the best fit spectral value to SDSS, 2MASS, and WISE photometry. WISE cannot resolve the DWD pair, and the W1 and W2 photometric measurements shown in Figure 5.2 are actually the combined emission from both WDs. The lack of any excess in either the 2MASS H and K bands (upper limits) and the WISE W1 and W2 bands eliminates

Table 5.1. Spectroscopic Fits

	VLT/UVES ^a			Gemini-N/GMOS ^b	
	Koester et al. (2009)	Koester Updated ^c	Our Fits	Baxter et al. (2014)	Our Fits
HS 2220+2146A					
log g	8.080±0.012	8.213±0.006	8.151±0.036	8.07±0.07	8.163±0.052
T_{eff}	14601±32	14434±58	14270±274	13950±321	14274±434
HS 2220+2146B					
log g	8.241±0.008	8.283±0.005	8.353±0.035	8.37±0.07	8.386±0.044
T_{eff}	18743±44	18305±29	18833±218	19020±438	19469±284

Note. — A comparison of the the various spectral fits to the WDs in HS 2220+2146 obtained with VLT/UVES and Gemini-N/GMOS spectra. All spectra show that HS 2220+2146B has a larger log g and T_{eff} . We use our fits to the VLT/UVES spectra throughout the remainder of this work.

^aReported values are weighted averages of fits to the two spectra of each WD obtained as part of the SPY survey (Koester et al. 2009).

^bReported values are weighted averages of fits to the three spectra of each WD obtained by Baxter et al. (2014).

^cWe refit the VLT/UVES spectra using an updated version of the same models used to originally fit the WDs from Koester et al. (2009).

the possibility of any late-type stellar companion or dust disk around either WD.

The putative hidden companion could be another WD, making the system a heirarchical triple WD like the two other such known systems,¹ G 021-15 (Farihi et al. 2005) and Sanduleak A/B (Maxted et al. 2000). To test this possibility, we obtained several follow-up spectra with the FLWO 1.5-meter telescope on the nights of 2015 July 11 and July 20 to search for radial velocity variations. These data were reduced using standard procedures. The spectra for each WD are cross-correlated with each observation to determine if there is any radial velocity shift. While there is an absolute uncertainty of $\sim 10 \text{ km s}^{-1}$ in these observations, the relative uncertainty across observations and between the two WDs is

¹We have recently identified a third WD candidate, PG 0901+140

Table 5.2. System Characteristics

	HS 2220+2146A	HS 2220+2146B
M_{WD} (M_{\odot})	0.702 ± 0.022	0.837 ± 0.022
τ_{cool} (Myr)	289 ± 22	179 ± 14
$v_{\text{radial}}^{\text{a}}$ (km s^{-1})	30 ± 7	53 ± 19
$v_{\text{grav}}^{\text{b}}$ (km s^{-1})	38 ± 2	53 ± 3
$M_{\text{ZAMS}}^{\text{c}}$ (M_{\odot})	2.8	3.9
$\tau_{\text{stellar}}^{\text{d}}$ (Myr)	590	230

Note. — M_{WD} and τ_{cool} for each WD are obtained from our fits to VLT spectra, see Table 5.1.

^aRadial velocities are obtained from averages of our FLWO spectra (see Figure 5.3). Listed uncertainties represent random errors. There is an additional systemic uncertainty of $\sim 10 \text{ km s}^{-1}$.

^bGravitational redshifts are obtained from interpolations of the WD models from Wood (1995).

^cInitial stellar masses are obtained by using the IFMR from Williams et al. (2009), using the listed M_{WD} .

^dStellar lifetimes are obtained from mesa evolution models, using the listed M_{ZAMS} .

negligible. Although the current data do not constrain all orbital periods and companion masses, Figure 5.3 shows that neither of these WDs shows any indication of significant radial velocity variations.

The dashed lines in Figure 5.3 show the average apparent radial velocity of each WD, which we provide along with the derived uncertainty in Table 5.1. HS 2220+2146B, with a larger mass, has an apparent radial velocity larger by 23 km s^{-1} . This difference is accounted for by the different gravitational redshifts of the two WDs, which can easily be

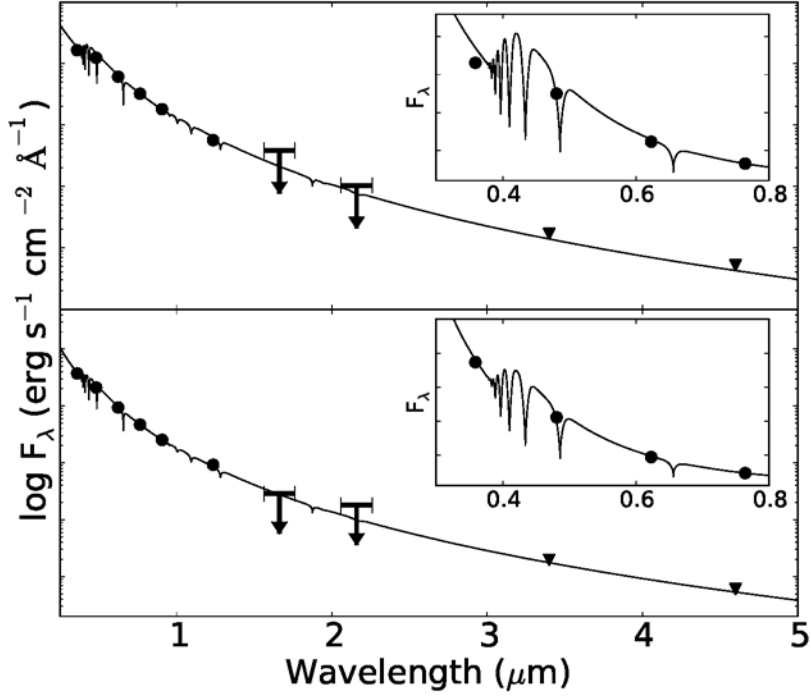


Figure 5.2 Using the best fit T_{eff} values from our spectral fits, we compare the SED of HS 2220+2146A and HS 2220+2146B with SDSS, 2MASS, and WISE photometry, normalized to the SDSS i band. 2MASS H and K photometry only provides upper limits. WISE cannot resolve the two WDs, and the W1 and W2 photometry (triangles) is for the combined DWD system. The WISE measurements, in particular, match the signal from just the WDs' blackbody radiation, precluding the existence of a hidden late-type stellar companion. In the inset figures, we focus on the visible component (SDSS $ugri$) of the SED. Note that here, we plot F_{λ} , not $\log F_{\lambda}$.

calculated straightforward from the WD's mass and radius (Falcon et al. 2010):

$$v_{\text{grav}} = \frac{G M_{\text{WD}}}{R_{\text{WD}} c}. \quad (5.1)$$

From our spectroscopically determined T_{eff} and M_{WD} measurements for each WD, we interpolate between the WD mass-radius tables from Wood (1995) to obtain the WD radii.

The contribution to the apparent radial velocity from gravitational redshift in Table 5.1.

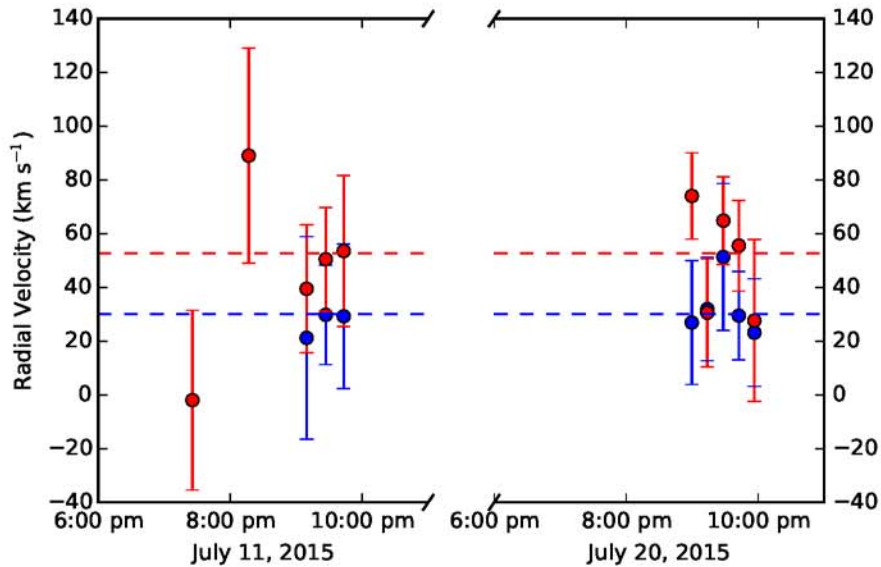


Figure 5.3 The radial velocities for HS 2220+2146A (blue) and HS 2220+2146B (red) calculated from the follow-up spectra taken with the 1.5-meter FLWO. There is no apparent radial velocity variation due to a hidden binary companion. HS 2220+2146B has a larger average radial velocity (red dashed line) than its companion (blue dashed line) because its larger mass causes a larger gravitational redshift. The apparent radial velocity difference provides a consistency check for our spectroscopic solutions.

If the system is indeed an associated binary, which is overwhelmingly indicated by both the work by Baxter et al. (2014) and Andrews et al. (in prep), the two WDs must have the same actual radial velocity. The difference in the apparent radial velocities of the two WDs must be due to differences in the gravitational redshift of the two WDs. Since HS 2220+2146B has a larger apparent radial velocity, it must also be more massive than its companion. Since the difference in the calculated gravitational redshift is in such close agreement with the observed radial velocity difference, these radial velocities provide an additional, independent consistency check on the spectroscopic results listed in Table 5.1.

Based on the original fits from the SPY survey (Koester et al. 2009), Baxter et al. (2014)

argue that when observational uncertainties are taken into account, using three separate test IFMRs, the two WDs are consistent with having been born at the same time and evolving independently.² As an independent check, Baxter et al. (2014) take their own low-resolution Gemini-N/GMOS spectra which are consistent with our spectral values. No matter which spectroscopic fit used, HS 2220+2146B always has a significantly larger $\log g$ and T_{eff} .

Why do these spectra produce such different results? One answer may lie in the spectral templates. Improvements have been made since the SPY survey spectral fits from Koester et al. (2009). In particular, Tremblay & Bergeron (2009) improved Stark broadening calculations and included some nonideal effects on the spectra. The numerical fitting techniques also differ (see Gianninas et al. 2011, for a discussion of these differences). Using up-to-date spectra, we fit the VLT spectra with both techniques, and provide both spectral values in Table 5.1. The disagreement in spectral values is typical. Regardless of the technique or models used, these spectral templates robustly show that HS 2220+2146B has a larger $\log g$ and higher T_{eff} than its companion: the more massive WD formed after the less massive WD. Hereafter we use the derived M_{WD} and τ_{cool} measurements from the Bergeron models applied to the VLT spectra.

²Baxter et al. (2014) increase the uncertainties on the original SPY survey fits for $\log g$ from 0.01 to 0.07, presumably to account for systematic uncertainties in the spectra, which may account for their conclusion that the system evolved normally.

5.3 Proposed Formation Scenario

To form a system in which the more massive WD formed second, we propose the scenario outlined in Figure 5.4. In this scenario, the system began as a hierarchical triple system. While all three stars were still on the MS, the inner binary merged forming a blue straggler. The system then appeared as a wide binary composed of the merger product (with a much shorter lifetime, but the merger “restarted” its clock) and a MS star that had already been undergoing nuclear burning. The outer, now less massive, star evolved first, into the $0.702 M_{\odot}$ WD, HS 2220+2146A. Somewhat later, the blue straggler evolved into the $0.837 M_{\odot}$ WD, HS 2220+2146B.

The high resolution WD spectra allow us to work backwards to reconstruct the evolution of this binary. The less massive WD in the pair has a cooling age of 289 Myr. Using the IFMR from Williams et al. (2009), this star evolved from a $2.8 M_{\odot}$ MS star. We run a suite of stellar evolution models using MESA to find that this star had a lifetime of 590 Myr. This sets the overall lifetime to 875 Myr (rounded to the nearest 25 Myr). The cooling age of the $0.837 M_{\odot}$ WD is 179 Myr indicating how long ago it evolved into a WD. Again, using the Williams et al. (2009) IFMR, we determine this WD came from a $3.9 M_{\odot}$ MS star. Our MESA models indicate this star had a lifetime of 230 Myr. The difference between the cooling age and stellar lifetimes of each WD derived by our models gives the merger time of the inner binary in the initial hierarchical triple. Although the general scenario outlined in Figure 5.4 is robust to different choices of stellar lifetime function or IFMR, the timeline provided in Figure 5.4 is suggestive, and we therefore round to the nearest 25 Myr.

	Time			Masses
System Birth	0 Myr			$M_{1,a} = 1.9$ $M_{1,b} = 1.9$ $M_2 = 2.81$
Inner Binary Mergers	475 Myr			$M_1 = 3.86$ $M_2 = 2.81$
Outer star evolves into an AGB star	575 Myr			$M_1 = 3.86$ $M_2 = 2.81$
Outer star evolves into a WD	575 Myr			$M_1 = 3.86$ $M_2 = 0.702$
Inner star evolves into an AGB star	700 Myr			$M_1 = 3.86$ $M_2 = 0.702$
Inner star evolves into a WD	700 Myr			$M_1 = 0.837$ $M_2 = 0.702$
Today	875 Myr			$M_1 = 0.837$ $M_2 = 0.702$

Figure 5.4 Our proposed formation history for HS 2220+2146 described in Section 5.3. The inner binary in a hierarchical triple system merged forming a blue straggler. The two stars then evolved independently, forming the WDs observed today. The provided timeline is inferred by working backwards from the observed WD cooling ages and stellar lifetimes assumed to form each WD. These are only rough times, rounded to the nearest 25 Myr.

The two WDs in HS 2220+2146 have an angular separation of $6.2''$. At the spectroscopic distance of 76 pc, this corresponds to a projected physical separation of 470 AU. For widely enough separated stars, mass is lost with the specific angular momentum of the mass losing star causing the orbit to expand upon mass loss (Jeans mode mass loss).

Orbital eccentricity does not secularly change, and $A(M_1 + M_2)$ is a conserved quantity (Hadjidemetriou 1963). If we take the current projected separation as a lower limit on A , we can estimate the orbital separation of the outer binary at birth to be $\gtrsim 110$ AU, expanding to 160 AU after the first component becomes a WD. The true orbital separation is likely to be somewhat larger due to the unknown inclination and phase of the orbit (Fischer & Marcy 1992).

5.4 Discussion

5.4.1 The Eccentric Kozai-Lidov Mechanism

The eccentric Kozai-Lidov (EKL) mechanism has been shown to cause the secular exchange of angular momentum between the inner and outer binary in triple systems (Kozai 1962; Lidov 1962). If our scenario provided in Figure 5.4 is correct, the 475 Myr merger time of the inner binary should match with simulations of the EKL mechanism. Naoz et al. (2013) provides the relevant quadrupolar timescale for the EKL mechanism:

$$t_{\text{quad}} \sim \frac{2\pi A_2^3 (1 - e_2^2)^{3/2} \sqrt{m_{1,a} + m_{1,b}}}{A_1^{3/2} m_2 \sqrt{G}}, \quad (5.2)$$

where A_1 and A_2 are the orbital separations of the inner and outer binary, and e_2 is the eccentricity of the outer binary. Setting $e_2 = 0.1$, we show t_{quad} as a function of A_2 for three separate values of A_1 in Figure 5.5.

In their parameter space study, Naoz & Fabrycky (2014) find that the inner binary

merges, t_{merge} between 5 and $100 t_{\text{quad}}$. Adopting 475 Myr for t_{merge} , the region between the dashed lines in Figure 5.5 ($1/5$ and $1/100 t_{\text{merge}}$) indicate the range of t_{quad} inferred. The EKL mechanism could have driven the inner binary to merge for $A_1 = 1$ AU and $A_2 = 200 - 500$ AU. Although there is a great deal of uncertainty in this estimate, particularly since we cannot know exactly how many quadrupolar timescales the system went through before merger, Figure 5.5 shows that the values for A_1 and A_2 implied by our t_{merge} are reasonable for a putative hierarchical triple progenitor of HS 2220+2146. Furthermore, Naoz & Fabrycky (2014) perform a Monte Carlo simulation, forward modeling a large population of triple systems. They find that the distribution of systems that merge forming blue straggler binaries peaks at roughly $P_{\text{orb}} \sim 10^5$ days or $A \sim 100$ AU (see their Figure 8) which matches our putative triple formation scenario outlined in 5.4.

We want to stress that although we cannot ascribe the merger of the inner binary of HS 2220+2146 to any particular physical process with certainty, the EKL mechanism is a natural choice, completely consistent with our suggested formation scenario.

5.4.2 Wind Mass Accretion

Our evolutionary formation for this system relies on the assumption that the two stars have never interacted, however when each star sheds its envelope, evolving from an asymptotic giant branch (AGB) star into a WD, some portion of the mass lost may be accreted by its companion. The binary separation is large enough that neither star will overfill its Roche lobe as an AGB star; instead the companion could accrete from the AGB star's wind. We are interested in determining first if, when the first star evolves into a

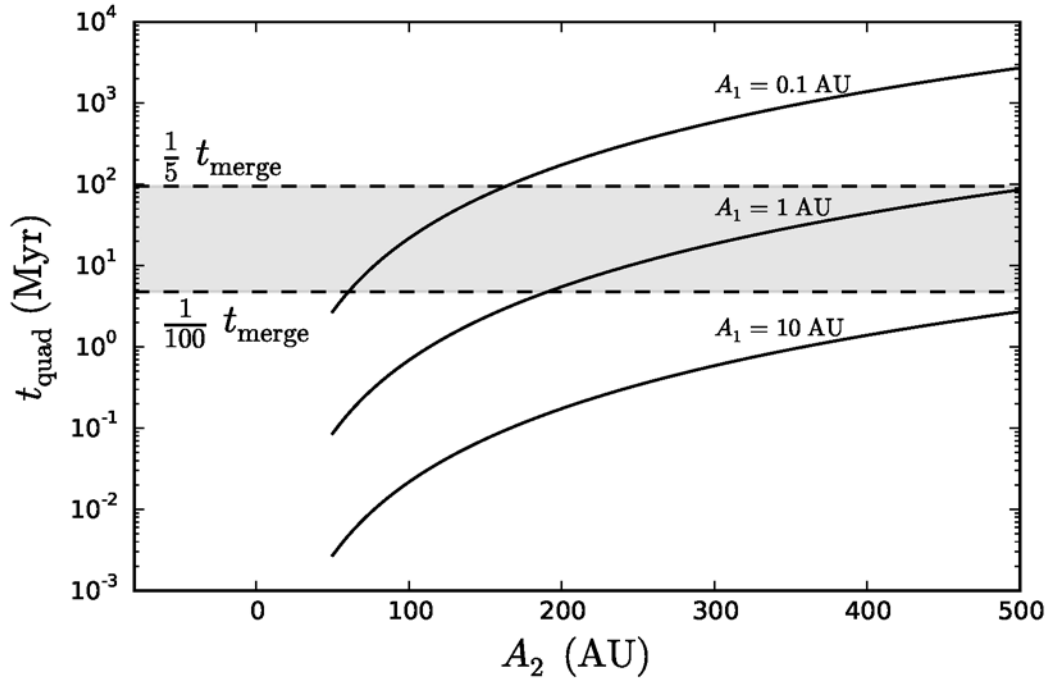


Figure 5.5 The quadrupolar timescale given in Equation 5.2 as a function of the outer orbital separation, A_2 , for three different inner binary orbital separations, A_1 , of 0.1 AU, 1 AU, and 10 AU (we have assumed $e_2 = 0.1$). The horizontal dashed lines indicate $1/5$ th and $1/100$ th of 475 Myr, the calculated t_{merge} . Naoz et al. (2013) find that the inner binary typically merges between 5 and 100 t_{quad} , indicated by the gray, filled region between the two dashed lines. HS 2220+2146 is consistent with having been formed through the EKL mechanism if the system began as a hierarchical triple with $A_1 \approx 1$ AU and $A_2 \approx 200 - 500$ AU.

WD, enough mass can be accreted by the MS companion to affect its mass or evolutionary timescale. Second, we would also like to know if, when the second star evolves into a WD, enough of its mass accretes onto its WD companion to affect its observed M_{WD} and τ_{cool} .

It is thought that mass is lost from AGB stars via a two step process (see Vassiliadis & Wood 1993, and references therein). First, pulsations on the AGB give rise to a low velocity wind which is slowed by gravity as it expands and cools. When the temperature

decreases sufficiently, dust grains condense (≈ 1000 K for silicates and ≈ 1500 K for amorphous carbon grains) (Höfner 2009). With their increased opacity, dust grains drive the second stage of the wind, caused by radiation pressure impacting the dust grains which are coupled to the surrounding gas, and the wind is quickly accelerated away from the star.

Mohamed & Podsiadlowski (2007) showed that a detached companion with a separation of \sim tens of AU could gravitationally focus the wind of an AGB star before being accelerated by radiation pressure (see also Mohamed & Podsiadlowski 2012). Termed Wind Roche Lobe Overflow (WRLOF), Abate et al. (2013) suggest the condition for WRLOF should be that the dust formation radius, R_c is a significant fraction of the Roche lobe radius, R_L of the donor star. Specifically, they find that when the $R_c > 0.4 R_L$, the accretion rate is enhanced with respect to the canonical Bondi-Hoyle-Littleton accretion rate (BHL), while $R_c < 0.4 R_L$, \dot{M} is well approximated by BHL. Abate et al. (2013) suggest that $R_c \approx 3 R_\star$ for most of the AGB phase. In a more detailed discussion, Höfner (2009) argues that silicates and amorphous carbon grains both typically have $R_c \approx 2 - 3R_\star$ (R_c may be somewhat larger for silicates when there is significant iron present). Recent observations of M-type AGB stars using mid-infrared interferometry seem to agree, showing $R_c/R_\star \approx 2$ for Al_2O_3 and $R_c/R_\star \approx 4$ for silicates (Karovicova et al. 2013). Additionally, Olofsson et al. (2002) and González Delgado et al. (2003) find that they can reasonably approximate the transition line profiles of CO and SiO in several dozen AGB stars using a constant wind velocity model for distances greater than a few stellar radii. From our MESA simulations, we find that a $4 M_\odot$ star reaches a maximum radius of ≈ 2.7 AU, while the potential donor

star has $R_L \approx 40$ AU (assuming an orbital separation of 110 AU). Therefore, WRLOF likely did not operate in HS 2220+2146, and the BHL accretion rate should well approximate \dot{M} .

BHL accretion assumes a companion accreting mass from a plane parallel wind with a constant velocity. This is appropriate here since the orbital separation is much larger than the radius of an AGB star. We first determine the Bondi radius where we combine the AGB wind velocity, v_{wind} , and the orbital velocity, v_{orb} , to determine the relative velocity between the wind and the accretor:

$$r_{\text{acc}} = \frac{2GM_{\text{acc}}}{v_{\text{wind}}^2 + v_{\text{orb}}^2} \quad (5.3)$$

where M_{acc} is the mass of the accretor. A wind speed of 10 km s^{-1} is typical (González Delgado et al. 2003), and M_{acc} and v_{orb} depend on the specifics of the binary in question.

We are first interested in when the $2.8 M_{\odot}$ outer star evolves into a $0.7 M_{\odot}$ WD, with a $3.8 M_{\odot}$ blue straggler companion as the accretor at a separation of ~ 110 AU. Using these numbers, we calculate the Bondi radius:

$$r_{\text{acc}} \approx 44 \text{ AU}. \quad (5.4)$$

In the plane parallel limit, we can estimate the amount of mass accreted onto the companion star by determining the fraction of the sky subtended by the companion's accretion radius, r_{acc} given the binary separation, A . In the limiting case, all the mass that falls

within the Bondi radius is accreted:

$$M_{\text{acc}} \approx \frac{\pi r_{\text{acc}}^2}{4\pi A^2} \Delta M_{\text{donor}} \quad (5.5)$$

$$\approx 0.1 \left(\frac{r_{\text{acc}}}{44 \text{ AU}} \right)^2 \left(\frac{A}{110 \text{ AU}} \right)^{-2} \left(\frac{\Delta M_{\text{donor}}}{2.1 M_{\odot}} \right) M_{\odot}. \quad (5.6)$$

Here, the Bondi radius is a significant portion of the orbital separation, and the plane parallel assumption may not be appropriate since the effect of the Roche potential may need to be taken into account. However, using 3D smoothed particle hydrodynamics, Mastrodemos & Morris (1999) simulate the effect of a wide, detached binary on the outflow of the wind from a dust-driven AGB wind. They find the accretion rates onto a binary companion are even lower than the Bondi-Hoyle derived rates. Even if we adopt the pessimistic assumption that all the mass falling within r_{acc} is accreted, only $\approx 0.1 M_{\odot}$ is accreted. This is an insignificant amount; a difference of $0.1 M_{\odot}$ alters the stellar lifetime by only ≈ 20 Myr.

This calculation can similarly be used to rule out the alternative blue straggler formation scenario in which instead of a hierarchical triple, the system begins as a roughly equal mass binary, each star of roughly $2.7 M_{\odot}$. If when the slightly more massive star evolves into a WD, its companion accretes $\approx 1 M_{\odot}$, it can rejuvenate the star, essentially forming a new, more massive MS star. Equations 5.3 and 5.5 show the difficulty of this formation scenario: r_{acc} will be smaller for a smaller mass accretor, and therefore M_{acc} will be even smaller than $0.1 M_{\odot}$ calculated above. For this scenario to be viable, the binary would have to accrete roughly half the mass lost by the AGB star (possibly through WRLOF), which is extremely unlikely for the orbital separations inferred from the projected separation

observed today.

We are next interested in when the $3.8 M_{\odot}$ star evolves into a $0.8 M_{\odot}$ WD, with a $0.7 M_{\odot}$ WD accretor at a separation of 160 AU. Using equation 5.3, we determine the Bondi radius for the WD:

$$r_{\text{acc}} \approx 10 \text{ AU}. \quad (5.7)$$

With a larger orbital separation of 160 AU, we can determine the amount of mass accreted using Equation 5.5:

$$M_{\text{acc}} \approx 0.003 \left(\frac{r_{\text{acc}}}{10 \text{ AU}} \right)^2 \left(\frac{A}{160 \text{ AU}} \right)^{-2} \left(\frac{\Delta M_{\text{donor}}}{3 M_{\odot}} \right) M_{\odot}.$$

Even a small hydrogen mass, less than $10^{-5} M_{\odot}$, accreted onto a WD is substantial enough to induce hydrogen burning (e.g., Nomoto et al. 2007; Wolf et al. 2013). Such nuclear burning would temporarily increase the WD's temperature, but leave its mass will largely unaffected. The system would be older than the age derived previously, making the discrepancy between cooling ages even larger. Given the several pessimistic assumptions used to derive this mass, it is possible that the system never underwent hydrogen burning. But even if hydrogen fusion did occur, our conclusion that the more massive WD is younger one in the pair remains unaffected.

We can rule out the alternative scenario in which the $0.8 M_{\odot}$ WD was formed first (the standard formation scenario), then reheated by a phase of surface hydrogen burning from mass accretion. Even if the WD retained enough of the nuclear burning energy to reheat it back to 10^5 K, the WD's cooling tracks remain essentially unchanged, and the two

WDs would have roughly the same τ_{cool} . To recreate the observed cooling age difference, the $0.8 M_{\odot}$ WD would have to be steadily burning material for 10^8 years. Since, planetary nebulae dissipate in 10^4 to 10^5 yrs (Badenes et al. 2015), HS 2220+2146 is unlikely to have formed in this manner.

5.5 Conclusions

HS 2220+2146 was recently identified by Baxter et al. (2014) as a wide DWD. We fit archival VLT/UVES and Gemini-N/GMOS spectra for both WDs in the pair which consistently show that this system has a peculiar quality: HS 2220+2146B, the more massive WD in the pair, is also the younger. Since WDs have an inverse mass-radius relation, the more massive WD should have a larger apparent radial velocity due to its increased gravitational redshift. Follow-up spectral observations agree with the expected radial velocities from our spectroscopic M_{WD} , providing an important consistency check. This system could not have been formed through the standard binary evolution channel.

One possibility is that one of the WDs in this system is actually an unresolved binary, however our follow-up spectra show no indications of radial velocity variations due to a hidden component. We also compare the WDs' SED with SDSS, 2MASS, and WISE photometry which exclude the presence of a late-type stellar companion.

To explain the peculiar qualities of this system, we suggest this system went through an alternative evolutionary channel in which HS2220+2146 formed as a triple system. The inner binary then merged to create a blue straggler in a wide binary. Both stars then evolved independently into the resolved pair of WDs we see today. Since the blue

straggler has a longer stellar lifetime than its mass would suggest, the discrepancy in this system's M_{WD} and τ_{cool} are naturally explained.

Using each WD's spectral fits for M_{WD} and τ_{cool} , we reconstruct the formation of this system, finding that the inner binary merged ~ 475 Myr after this system was formed. When we make reasonable assumptions about the system's initial configuration, the eccentric Kozai-Lidov mechanism is consistent with causing the inner binary to merge in the observed timescale.

We show that at the observed binary separation, the two WDs essentially evolved independently. The system is too widely separated for wind Roche lobe overflow to have occurred, and Bondi accretion of either star's wind is insignificant.

Although there may be other, exotic evolutionary channels that can form HS 2220+2146, our proposed scenario naturally explains the observations. Furthermore, there are two known hierarchical triple WDs in the literature which would be the analogs of HS 2220+2146 in which the inner binary did not merge. Triple systems are common in the Universe, and as the endpoints of intermediate mass triple stellar evolution, triple WDs and other systems similar to HS 2220+2146 may exist. Finding more of these systems may allow a better understanding of the dynamics involved in triple stellar evolution, including the eccentric Kozai-Lidov mechanism.

5.6 Acknowledgments

We acknowledge useful conversations with Phil Macias, Smadar Naoz, and Enrico Ramirez-Ruiz. M.A.A., M.K., and A.G. gratefully acknowledge the support of the NSF and NASA

under grants AST-1255419, AST-1312678, and NNX14AF65G, respectively.

Based on observations obtained at the Gemini Observatory acquired through the Gemini Science Archive and processed using the gemini pyraf package, which is operated by the Association of Universities for Research in Astronomy, Inc., under a cooperative agreement with the NSF on behalf of the Gemini partnership: the National Science Foundation (United States), the National Research Council (Canada), CONICYT (Chile), the Australian Research Council (Australia), Ministério da Ciência, Tecnologia e Inovação (Brazil) and Ministerio de Ciencia, Tecnología e Innovación Productiva (Argentina).

This publication makes use of data products from the Wide-field Infrared Survey Explorer, which is a joint project of the University of California, Los Angeles, and the Jet Propulsion Laboratory/California Institute of Technology, funded by the National Aeronautics and Space Administration.

(This page left intentionally blank.)

Chapter 6

Conclusions

Adapted from academic papers accepted, submitted, or soon to be submitted, the chapters comprising this thesis run the gamut of astronomical techniques including observations, theory, data mining, and simulations. In many ways, they form a disparate compilation, yet underlying this dissertation are common threads:

- This dissertation focuses on both close and wide DWDs, the endpoints of intermediate mass binary formation. These systems provide stringent tests of our understanding of binary evolution; having evolved through all the types of interactions occurring in stellar binaries, the population of DWDs represents the cumulative effects of a variety of both single and binary stellar evolutionary processes. Larger populations of DWDs allow a better understanding of these processes.
- The individual chapters in this dissertation chip away at long-standing astronomical problems; by no means are they meant to be the last word on any of these topics. They merely represent attempts to build and develop techniques to attack difficult

questions. In the case of LMWDs, we are ultimately interested in constraining the CE phase. In Chapters 3 and 4, we identify a sample of wide DWDs to constrain the IFMR. And finally, in Chapter 5, the wide DWD HS 2220+2146 (and other systems like it) may improve our understanding of the EKL mechanism and the importance of triple systems in our Galaxy.

- The work here relies heavily on data analysis. In Chapter 2 we developed new statistical techniques to work with single-line spectroscopic binaries. Before our first search in SDSS (Andrews et al. 2012), there had been no systematic effort to identify new systems in two decades. It was a primary goal of Chapters 3 and 4 to determine how we could efficiently identify wide DWDs in large data sets. Finally, the formation scenario we reached in Chapter 5 for HS 2220+2146 resulted from a careful interpretation of the data we obtained.

The data available for the studies throughout this dissertation are constantly increasing. The ELM WD sample is only getting larger, with an additional 24 systems expected to be published soon. New astrometric data sets ideal for identifying wide DWDs such as *Gaia* should be public soon as well. The work represented here will only have more relevance as new data come online.

Below, we briefly revisit our results and provide some avenues for future research.

6.1 Summary of Results and Future Work

The work we present in Chapter 2 is a first step toward using LMWDs to constrain binary evolution. We developed a new statistical technique to constrain the companion masses to LMWDs, showing that LMWDs had, on average, massive WDs, with $M_{\text{WD}} > 0.7 M_{\odot}$. This is unexpected from population synthesis studies which predict that LMWDs should often come in pairs. A clear avenue for future research would be to run population synthesis simulations to identify which parameters can explain the observed mass ratios in these systems.

The biggest uncertainty in binary evolution involves the CE, and ultimately LMWDs have the potential to place strong constraints for three reasons. First, the data set is comprised of 61 objects, 55 of which are clearly in a binary, and another two dozen LMWDs are to be published soon. This sample is statistically large enough to start to study these objects as a population. Second, because essentially every system is in a binary, there are no strong observational biases in P_{orb} , crucially important for constraining CE physics. Third, since both components are WDs, LMWDs may have gone through two CEs, making them sensitive tests of CE physics (although Woods et al. 2012, argue that for some DWDs, one of the mass transfer phases may have been stable). Any constraints on CE physics using LMWDs is outside the scope of the work presented here, but our study presented in Chapter 2 lays the groundwork for just such an analysis.

In our search for new wide DWDs in Chapter 3, we began by building up the previously identified sample from the heterogeneous data set scattered throughout the literature. We were able to compile these data into a table that included any available

spectroscopic data. We continued to collect data on wide DWDs, including the systems from Baxter et al. (2014) and our own search through SDSS DR9, described in Chapter 4. There are now 142 known systems, and this number will only increase as more large scale surveys come online. To allow other researchers to use wide DWDs to constrain physics, we have made our current catalog publicly available for download.

Photometric surveys such as Pan-STARRS (with its 3π steradian survey coverage) and LSST may produce many new wide DWDs. Ultimately, *Gaia*, with its ability to measure 6-dimensional phase space data for WDs out to several hundred parsecs, will revolutionize the discovery of wide DWDs. Importantly, its precision astrometry will allow the high-fidelity discovery of new wide DWDs, without significant contamination from foreground or background objects. Furthermore, *Gaia*'s very low resolution photometer will estimate a WD's temperature, and comparing the WD's distance with its brightness and T_{eff} will give a radius, and hence a mass, measurement, *without any observational follow-up*. One would have difficulty imagining a more perfect instrument for not just searching for new wide DWDs, but also for identifying the most interesting systems, those in which the WDs have differing masses.

Wide DWDs can be used for constraining the expansion of orbits due to mass loss and probing the Galactic tide (Sion et al. 1991). In addition to these (and possibly other) astronomical phenomenon, because of the method developed in Chapter 4, wide DWDs have the clearest potential to constrain the IFMR. Although the sample of 19 wide DWDs we use to actually place our constraints is relatively small, this sample will only grow. Optimistically, *Gaia* may allow us to increase the known sample by a factor of a few, and

with spectroscopic follow-up, we may eventually have some 50 to 100 spectroscopically characterized wide DWDs to constrain the IFMR. Adding these to our model is trivial. With such a sample, we can revolutionize our understanding of the IFMR.

A complete understanding of the IFMR will require constraints from more than one method. Open cluster WDs are best at constraining the higher mass regime, since only massive stars have evolved off the MS in most open clusters. Since they are older, globular cluster constraints are better at constraining the lower mass regime, since these take many Gyr to evolve. Finally, wide binaries composed of a WD with a non-WD companion constrain the lower to intermediate mass regime. Ultimately, these methods complement each other and will all need to be used to completely define the IFMR. Our method presented in Chapter 4, although it employs somewhat modern statistical algorithms for probing parameter space, is still quite simplistic in its approach. It can potentially be expanded to combine constraints from all observational methods, but such a complex model is still many years away.

Finally, this work touches on the endpoints of intermediate mass triple star evolution through both hierarchical triple WDs (G 21-15 and Sanduleak A/B) and the system HS 2220+2146, which likely formed initially as a triple system, but is today seen as a DWD. The prevalence of unevolved triple systems in the Galaxy almost certainly guarantee that there are many more triple WD systems. While the formation and evolution of triple WDs has been largely ignored in the literature (probably due to their obscurity) it seems likely that recent astronomical focus on dynamics will draw increased attention to these systems. Researchers interested in the triple system dynamics are only recently beginning

to include important stellar evolution effects (the most obvious is a realistic treatment of stellar tides) in their studies. If more peculiar systems like HS 2220+2146 are found, in depth studies of the formation of these systems may provide a better understanding of the stellar interactions involved. It seems clear that there is much we can learn from these triple systems, and given their prevalence, we may not be able to ignore their effects of triple dynamics on the population of WDs in the Galaxy.

Chapter 7

Bibliography

Aaronson, M., & Mould, J. 1985, *ApJ*, 288, 551

Abate, C., Pols, O. R., Izzard, R. G., Mohamed, S. S., & de Mink, S. E. 2013, *A&A*, 552, A26

Abazajian, K. N. et al. 2009, *ApJS*, 182, 543

Agüeros, M. A. et al. 2009a, *ApJS*, 181, 444

Agüeros, M. A., Camilo, F., Silvestri, N. M., Kleinman, S. J., Anderson, S. F., & Liebert, J. W. 2009b, *ApJ*, 697, 283

Ahn, C. P. et al. 2012, *ApJS*, 203, 21

Althaus, L. G., Serenelli, A. M., Panei, J. A., Córscico, A. H., García-Berro, E., & Scóccola, C. G. 2005, *A&A*, 435, 631

Ambartsumian, V. A. 1937, *Astron. Zhurn.*, 14, 207

Andrews, J. J., Agüeros, M. A., Belczynski, K., Dhital, S., Kleinman, S. J., & West, A. A. 2012, *ApJ*, 757, 170

Andrews, J. J., Price-Whelan, A. M., & Agüeros, M. A. 2014, *ApJL*, 797, L32

Antoniadis, J., van Kerkwijk, M. H., Koester, D., Freire, P. C. C., Wex, N., Tauris, T. M., Kramer, M., & Bassa, C. G. 2012, *MNRAS*, 423, 3316

Asplund, M., Grevesse, N., Sauval, A. J., & Scott, P. 2009, *ARA&A*, 47, 481

- Astropy Collaboration et al. 2013, *A&A*, 558, A33
- Auer, L. H., & Woolf, N. J. 1965, *ApJ*, 142, 182
- Badenes, C., Maoz, D., & Ciardullo, R. 2015, *ApJL*, 804, L25
- Badenes, C., Mullally, F., Thompson, S. E., & Lupton, R. H. 2009, *ApJ*, 707, 971
- Barstow, M. A., Bond, H. E., Holberg, J. B., Burleigh, M. R., Hubeny, I., & Koester, D. 2005, *MNRAS*, 362, 1134
- Barstow, M. A., Jordan, S., O'Donoghue, D., Burleigh, M. R., Napiwotzki, R., & Harrop-Allin, M. K. 1995, *MNRAS*, 277, 971
- Bassa, C. G., et al. 2006, *A&A*, 456, 295
- Baxter, R. B. et al. 2014, *MNRAS*, 440, 3184
- Bedijn, P. J. 1988, *A&A*, 205, 105
- Belczynski, K., Kalogera, V., & Bulik, T. 2002, *ApJ*, 572, 407
- Belczynski, K., Kalogera, V., Rasio, F. A., Taam, R. E., Zezas, A., Bulik, T., Maccarone, T. J., & Ivanova, N. 2008, *ApJS*, 174, 223
- Bergeron, P., Leggett, S. K., & Ruiz, M. T. 2001, *ApJS*, 133, 413
- Bergeron, P., Ruiz, M. T., & Leggett, S. K. 1997, *ApJS*, 108, 339
- Bergeron, P., Saffer, R. A., & Liebert, J. 1992, *ApJ*, 394, 228
- Bergeron, P. et al. 2011, *ApJ*, 737, 28
- Böhm-Vitense, E. 1958, *ZAp*, 46, 108
- Boss, A. P. 1988, *Comments on Astrophysics*, 12, 169
- Bours, M. C. P. et al. 2015, *MNRAS*, 450, 3966
- Brandt, T. D., & Huang, C. X. 2015, *ApJ*, 807, 24
- Brown, J. M., Kilic, M., Brown, W. R., & Kenyon, S. J. 2011a, *ApJ*, 730, 67
- Brown, W. R., Geller, M. J., Kenyon, S. J., Kurtz, M. J., & Bromley, B. C. 2007, *ApJ*, 660, 311

Brown, W. R., Kilic, M., Allende Prieto, C., Gianninas, A., & Kenyon, S. J. 2013, *ApJ*, 769, 66

Brown, W. R., Kilic, M., Allende Prieto, C., & Kenyon, S. J. 2010, *ApJ*, 723, 1072

—. 2012, *ApJ*, 744, 142

Brown, W. R., Kilic, M., Hermes, J. J., Allende Prieto, C., Kenyon, S. J., & Winget, D. E. 2011b, *ApJL*, 737, L23

Brown, W. R., et al. 2006, *ApJ*, 647, 303

Callanan, P. J., et al. 1998, *MNRAS*, 298, 207

Canuto, V. M. 1998, *ApJL*, 508, L103

Carrasco, J. M., Catalán, S., Jordi, C., Tremblay, P.-E., Napiwotzki, R., Luri, X., Robin, A. C., & Kowalski, P. M. 2014, *A&A*, 565, A11

Carrera, R., & Pancino, E. 2011, *A&A*, 535, A30

Casali, M. et al. 2007, *A&A*, 467, 777

Casewell, S. L., Dobbie, P. D., Geier, S., Lodieu, N., & Hambly, N. C. 2015, *MNRAS*, 451, 4259

Catalán, S. 2015, in *Astronomical Society of the Pacific Conference Series*, Vol. 493, 19th European Workshop on White Dwarfs, ed. P. Dufour, P. Bergeron, & G. Fontaine, 325

Catalán, S., Isern, J., García-Berro, E., & Ribas, I. 2008a, *MNRAS*, 387, 1693

Catalán, S., Isern, J., García-Berro, E., Ribas, I., Allende Prieto, C., & Bonanos, A. Z. 2008b, *A&A*, 477, 213

Chanamé, J., & Gould, A. 2004, *ApJ*, 601, 289

Claver, C. F., Liebert, J., Bergeron, P., & Koester, D. 2001, *ApJ*, 563, 987

Clemens, D. P., Yun, J. L., & Heyer, M. H. 1991, *ApJS*, 75, 877

Cojocaru, R., Torres, S., Isern, J., & García-Berro, E. 2014, *A&A*, 566, A81

Covey, K. R. et al. 2007, *AJ*, 134, 2398

Cummings, J. D., Kalirai, J. S., Tremblay, P.-E., & Ramirez-Ruiz, E. 2015, ArXiv e-prints

Dawson, S. A., & Schröder, K.-P. 2012, *MNRAS*, 420, 2339

De Marco, O., Passy, J.-C., Moe, M., Herwig, F., Mac Low, M.-M., & Paxton, B. 2011, *MNRAS*, 411, 2277

Dhital, S., West, A. A., Stassun, K. G., & Bochanski, J. J. 2010, *AJ*, 139, 2566

Dhital, S., West, A. A., Stassun, K. G., Schluns, K. J., & Massey, A. P. 2015, *AJ*, 150, 57

Dobbie, P. D., Baxter, R., Külebi, B., Parker, Q. A., Koester, D., Jordan, S., Lodieu, N., & Euchner, F. 2012a, *MNRAS*, 421, 202

Dobbie, P. D., Day-Jones, A., Williams, K. A., Casewell, S. L., Burleigh, M. R., Lodieu, N., Parker, Q. A., & Baxter, R. 2012b, *MNRAS*, 423, 2815

Dobbie, P. D. et al. 2013, *MNRAS*, 428, L16

—. 2006, *MNRAS*, 369, 383

Dobbie, P. D., Napiwotzki, R., Burleigh, M. R., Williams, K. A., Sharp, R., Barstow, M. A., Casewell, S. L., & Hubeny, I. 2009, *MNRAS*, 395, 2248

Dobbie, P. D., Pinfield, D. J., Napiwotzki, R., Hambly, N. C., Burleigh, M. R., Barstow, M. A., Jameson, R. F., & Hubeny, I. 2004, *MNRAS*, 355, L39

Dominguez, I., Chieffi, A., Limongi, M., & Straniero, O. 1999, *ApJ*, 524, 226

Douglas, S. T. et al. 2014, *ApJ*, 795, 161

Dupuy, T. J., & Liu, M. C. 2011, *ApJ*, 733, 122

Duquennoy, A., & Mayor, M. 1991, *A&A*, 248, 485

Eggen, O. J., & Greenstein, J. L. 1965, *ApJ*, 141, 83

Eisenstein, D. J. et al. 2006a, *ApJS*, 167, 40

—. 2006b, *ApJS*, 167, 40

Falcon, R. E., Winget, D. E., Montgomery, M. H., & Williams, K. A. 2010, *ApJ*, 712, 585

Farihi, J. 2004a, PhD thesis, University of California, s Angeles, California, USA

—. 2004b, *ApJ*, 610, 1013

Farihi, J., Becklin, E. E., & Zuckerman, B. 2005, *ApJS*, 161, 394

Farihi, J., Hoard, D. W., & Wachter, S. 2006, *ApJ*, 646, 480

Finley, D. S., & Koester, D. 1997, *ApJL*, 489, L79

Fischer, D. A., & Marcy, G. W. 1992, *ApJ*, 396, 178

Fontaine, G., Brassard, P., & Bergeron, P. 2001, *PASP*, 113, 409

Foreman-Mackey, D., Hogg, D. W., Lang, D., & Goodman, J. 2013a, *PASP*, 125, 306

—. 2013b, *PASP*, 125, 306

Frantsman, I. L. 1986, *Astrofizika*, 25, 517

—. 1988, *Ap&SS*, 145, 251

Freytag, B., Ludwig, H.-G., & Steffen, M. 1996, *A&A*, 313, 497

Freytag, B., Steffen, M., Ludwig, H.-G., Wedemeyer-Böhm, S., Schaffenberger, W., & Steiner, O. 2012, *Journal of Computational Physics*, 231, 919

Fuhrmann, K. 1998, *A&A*, 338, 161

García-Berro, E. et al. 2012, *ApJ*, 749, 25

García-Berro, E., Torres, S., Althaus, L. G., & Miller Bertolami, M. M. 2014, *A&A*, 571, A56

Geller, A. M., & Mathieu, R. D. 2011, *Nature*, 478, 356

Gianninas, A., Bergeron, P., & Fontaine, G. 2005, *ApJ*, 631, 1100

Gianninas, A., Bergeron, P., & Ruiz, M. T. 2011, *ApJ*, 743, 138

Gianninas, A., Dufour, P., Kilic, M., Brown, W. R., Bergeron, P., & Hermes, J. J. 2014, *ApJ*, 794, 35

Gim, M., Vandenberg, D. A., Stetson, P. B., Hesser, J. E., & Zurek, D. R. 1998, *PASP*, 110, 1318

Girardi, L. et al. 2010, *ApJ*, 724, 1030

- Girven, J., Gänsicke, B. T., Külebi, B., Steeghs, D., Jordan, S., Marsh, T. R., & Koester, D. 2010, *MNRAS*, 404, 159
- Girven, J., Gänsicke, B. T., Steeghs, D., & Koester, D. 2011, *MNRAS*, 417, 1210
- González Delgado, D., Olofsson, H., Kerschbaum, F., Schöier, F. L., Lindqvist, M., & Groenewegen, M. A. T. 2003, *A&A*, 411, 123
- Goodman, J., & Weare, J. 2010, *Comm. App. Math. Comp. Sci.*, 5, 65
- Gosnell, N. M., Mathieu, R. D., Geller, A. M., Sills, A., Leigh, N., & Knigge, C. 2014, *ApJL*, 783, L8
- Greaves, J. 2005, *Journal of Double Star Observations*, 1, 41
- Green, R. F., Schmidt, M., & Liebert, J. 1986, *ApJS*, 61, 305
- Greenstein, J. L. 1984, *ApJ*, 276, 602
- . 1986a, *AJ*, 92, 859
- . 1986b, *AJ*, 92, 859
- . 1986c, *AJ*, 92, 867
- Greenstein, J. L., Dolez, N., & Vauclair, G. 1983, *A&A*, 127, 25
- Grevesse, N., & Noels, A. 1993, in *Origin and Evolution of the Elements*, ed. N. Prantzos, E. Vangioni-Flam, & M. Casse, 15–25
- Hadjidemetriou, J. D. 1963, *Icarus*, 2, 440
- Hambly, N. C. et al. 2008, *MNRAS*, 384, 637
- Han, Z. 1998, *MNRAS*, 296, 1019
- Hansen, B. M. S., et al. 2007, *ApJ*, 671, 380
- Haro, G., & Luyten, W. J. 1962, *Boletín de los Observatorios Tonantzintla y Tacubaya*, 3, 37
- Hermes, J. J. et al. 2014, *ApJ*, 792, 39
- Herwig, F. 2000, *A&A*, 360, 952

- Herwig, F., Bloeker, T., Schoenberner, D., & El Eid, M. 1997, *A&A*, 324, L81
- Herwig, F., Schoenberner, D., & Bloeker, T. 1998, *A&A*, 340, L43
- Hewett, P. C., Warren, S. J., Leggett, S. K., & Hodgkin, S. T. 2006, *MNRAS*, 367, 454
- Hintzen, P., Oswalt, T. D., Liebert, J., & Sion, E. M. 1989, *ApJ*, 346, 454
- Hodgkin, S. T., Irwin, M. J., Hewett, P. C., & Warren, S. J. 2009, *MNRAS*, 394, 675
- Höfner, S. 2009, in *Astronomical Society of the Pacific Conference Series*, Vol. 414, *Cosmic Dust - Near and Far*, ed. T. Henning, E. Grün, & J. Steinacker, 3
- Hogg, D. W., Bovy, J., & Lang, D. 2010, *ArXiv e-prints*
- Holberg, J. B. 2005, in *Bulletin of the American Astronomical Society*, Vol. 37, *American Astronomical Society Meeting Abstracts*, 205.01
- Holberg, J. B., & Bergeron, P. 2006, *AJ*, 132, 1221
- Holberg, J. B., Sion, E. M., Oswalt, T., McCook, G. P., Foran, S., & Subasavage, J. P. 2008, *AJ*, 135, 1225
- Iben, Jr., I. 1975, *ApJ*, 196, 525
- Iben, J. I., & Livio, M. 1993, *PASP*, 105, 1373
- Ivanova, N. et al. 2013, *A&A Rev.*, 21, 59
- Jiang, Y.-F., & Tremaine, S. 2010, *MNRAS*, 401, 977
- Jordan, S. et al. 1998, *A&A*, 330, 277
- Justham, S., Wolf, C., Podsiadlowski, P., & Han, Z. 2009, *A&A*, 493, 1081
- Kalirai, J. S., Hansen, B. M. S., Kelson, D. D., Reitzel, D. B., Rich, R. M., & Richer, H. B. 2008, *ApJ*, 676, 594
- Kalirai, J. S., Marigo, P., & Tremblay, P.-E. 2014, *ApJ*, 782, 17
- Kalirai, J. S., Richer, H. B., Reitzel, D., Hansen, B. M. S., Rich, R. M., Fahlman, G. G., Gibson, B. K., & von Hippel, T. 2005, *ApJL*, 618, L123

- Kalirai, J. S., Saul Davis, D., Richer, H. B., Bergeron, P., Catelan, M., Hansen, B. M. S., & Rich, R. M. 2009, *ApJ*, 705, 408
- Kaplan, D. L. et al. 2014, *ApJ*, 780, 167
- Karakas, A. I., Lattanzio, J. C., & Pols, O. R. 2002, *PASA*, 19, 515
- Karovicova, I., Wittkowski, M., Ohnaka, K., Boboltz, D. A., Fossat, E., & Scholz, M. 2013, *A&A*, 560, A75
- Kawka, A., & Vennes, S. 2005, in *Astronomical Society of the Pacific Conference Series*, Vol. 334, 14th European Workshop on White Dwarfs, ed. D. Koester & S. Moehler, 101
- Kepler, S. O., Kleinman, S. J., Nitta, A., Koester, D., Castanheira, B. G., Giovannini, O., Costa, A. F. M., & Althaus, L. 2007, *MNRAS*, 375, 1315
- Kepler, S. O. et al. 2015, *MNRAS*, 446, 4078
- Kilic, M., Brown, W. R., Allende Prieto, C., Agüeros, M. A., Heinke, C., & Kenyon, S. J. 2011, *ApJ*, 727, 3
- Kilic, M., Brown, W. R., Allende Prieto, C., Kenyon, S. J., Heinke, C. O., Agüeros, M. A., & Kleinman, S. J. 2012, *ApJ*, 751, 141
- Kilic, M. et al. 2013, *MNRAS*, 434, 3582
- . 2014, *MNRAS*, 438, L26
- Kilic, M., Kowalski, P. M., Reach, W. T., & von Hippel, T. 2009, *ApJ*, 696, 2094
- Kilic, M. et al. 2006, *AJ*, 131, 582
- Kilic, M., Stanek, K. Z., & Pinsonneault, M. H. 2007, *ApJ*, 671, 761
- Kiziltan, B., Kottas, A., De Yoreo, M., & Thorsett, S. E. 2013, *ApJ*, 778, 66
- Kleinman, S. J. et al. 2004, *ApJ*, 607, 426
- . 2013, *ApJS*, 204, 5
- Kobulnicky, H. A., & Fryer, C. L. 2007, *ApJ*, 670, 747
- Koester, D., & Reimers, D. 1981, *A&A*, 99, L8

—. 1996, *A&A*, 313, 810

Koester, D., Voss, B., Napiwotzki, R., Christlieb, N., Homeier, D., Lisker, T., Reimers, D., & Heber, U. 2009, *A&A*, 505, 441

Koester, D., & Weidemann, V. 1980, *A&A*, 81, 145

Kowalski, P. M., & Saumon, D. 2006, *ApJL*, 651, L137

Kozai, Y. 1962, *AJ*, 67, 591

Kraus, A. L., & Hillenbrand, L. A. 2009, *ApJ*, 704, 531

Kroupa, P., Tout, C. A., & Gilmore, G. 1993, *MNRAS*, 262, 545

Külebi, B., Jordan, S., Nelan, E., Bastian, U., & Altmann, M. 2010, *A&A*, 524, A36

Lawrence, A. et al. 2007, *MNRAS*, 379, 1599

Lee-Brown, D. B., Anthony-Twarog, B. J., Deliyannis, C. P., Rich, E., & Twarog, B. A. 2015, *AJ*, 149, 121

Lépine, S., & Bongiorno, B. 2007, *AJ*, 133, 889

Lépine, S., & Shara, M. M. 2005, *AJ*, 129, 1483

Lidov, M. L. 1962, *planss*, 9, 719

Liebert, J., Bergeron, P., & Holberg, J. B. 2005a, *ApJS*, 156, 47

Liebert, J., Fontaine, G., Young, P. A., Williams, K. A., & Arnett, D. 2013, *ApJ*, 769, 7

Liebert, J., Young, P. A., Arnett, D., Holberg, J. B., & Williams, K. A. 2005b, *ApJL*, 630, L69

Liebert, J., et al. 2004, *ApJL*, 606, L147

—. 2005c, *ApJS*, 156, 47

Lugaro, M., Herwig, F., Lattanzio, J. C., Gallino, R., & Straniero, O. 2003, *ApJ*, 586, 1305

Luyten, W. J. 1963, in Bruce proper motion survey. The general catalogue (vol 1,2). (1963),
0

- Luyten, W. J. 1979, New Luyten catalogue of stars with proper motions larger than two tenths of an arcsecond; and first supplement; NLTT. (Minneapolis (1979)); Label 12 = short description; Label 13 = documentation by Warren; Label 14 = catalogue
- . 1987, My first 72 years of astronomical research. Reminiscences of an astronomical curmudgeon, revealing the presence of human nature in science. (Willem J)
- . 1988, *Ap&SS*, 142, 17
- Marigo, P., Bressan, A., Nanni, A., Girardi, L., & Pumo, M. L. 2013, *MNRAS*, 434, 488
- Marigo, P., & Girardi, L. 2007, *A&A*, 469, 239
- Marsh, T. R., Gänsicke, B. T., Steeghs, D., Southworth, J., Koester, D., Harris, V., & Merry, L. 2011, *ApJ*, 736, 95
- Marsh, T. R., et al. 1995, *MNRAS*, 275, 828
- Mastrodemos, N., & Morris, M. 1999, *ApJ*, 523, 357
- Mathieu, R. D., & Geller, A. M. 2009, *Nature*, 462, 1032
- Maxted, P. F. L., Marsh, T. R., Moran, C. K. J., & Han, Z. 2000, *MNRAS*, 314, 334
- Mazzei, P., & Pigatto, L. 1988, *A&A*, 193, 148
- McCook, G. P., & Sion, E. M. 1977, A Catalogue of spectroscopically identified white dwarfs
- . 1987, *ApJS*, 65, 603
- . 1999, *ApJS*, 121, 1
- Meng, X., Chen, X., & Han, Z. 2008, *A&A*, 487, 625
- Meng, X. C., Chen, W. C., Yang, W. M., & Li, Z. M. 2011, *A&A*, 525, A129+
- Mohamed, S., & Podsiadlowski, P. 2007, in *Astronomical Society of the Pacific Conference Series*, Vol. 372, 15th European Workshop on White Dwarfs, ed. R. Napiwotzki & M. R. Burleigh, 397
- Mohamed, S., & Podsiadlowski, P. 2012, *Baltic Astronomy*, 21, 88
- Munn, J. A. et al. 2004, *AJ*, 127, 3034

- . 2008, *AJ*, 136, 895
- Naoz, S., & Fabrycky, D. C. 2014, *ApJ*, 793, 137
- Naoz, S., Kocsis, B., Loeb, A., & Yunes, N. 2013, *ApJ*, 773, 187
- Nebot Gómez-Morán, A. et al. 2011, *A&A*, 536, A43
- Nelemans, G. et al. 2005, *A&A*, 440, 1087
- Nelemans, G., & Tout, C. A. 2005, *MNRAS*, 356, 753
- Nelemans, G., Verbunt, F., Yungelson, L. R., & Portegies Zwart, S. F. 2000, *A&A*, 360, 1011
- Nelemans, G., Yungelson, L. R., Portegies Zwart, S. F., & Verbunt, F. 2001a, *A&A*, 365, 491
- . 2001b, *A&A*, 365, 491
- Nomoto, K., Saio, H., Kato, M., & Hachisu, I. 2007, *ApJ*, 663, 1269
- Olofsson, H., González Delgado, D., Kerschbaum, F., & Schöier, F. L. 2002, *A&A*, 391, 1053
- Öpik, E. J. 1924, *Tartu Obs. Publ.*, 25
- Oswalt, T. D., Hintzen, P. M., Liebert, J. W., & Sion, E. M. 1988, *ApJL*, 333, L87
- Oswalt, T. D., & Strunk, D. 1994, in *Bulletin of the American Astronomical Society*, Vol. 26, American Astronomical Society Meeting Abstracts #184, 901
- Overbeek, J. C., Friel, E. D., Jacobson, H. R., Johnson, C. I., Pilachowski, C. A., & Mészáros, S. 2015, *AJ*, 149, 15
- Özel, F., Psaltis, D., Narayan, R., & Santos Villarreal, A. 2012, *ApJ*, 757, 55
- Parker, Q. 2011, A New Lead on the White Dwarf Initial-to-Final Mass Relation, HST Proposal
- Paxton, B., Bildsten, L., Dotter, A., Herwig, F., Lesaffre, P., & Timmes, F. 2011, *ApJS*, 192, 3
- Paxton, B. et al. 2013, *ApJS*, 208, 4
- . 2015, ArXiv e-prints
- Perets, H. B., & Fabrycky, D. C. 2009, *ApJ*, 697, 1048

- Perryman, M. A. C. et al. 1998, *A&A*, 331, 81
- Peters, P. C. 1964, *Phys. Rev.*, 136, B1224
- Pickering, E. C. 1899, *ApJ*, 9, 175
- Pignatari, M. et al. 2013, ArXiv e-prints
- Poveda, A., Allen, C., & Hernández-Alcántara, A. 2007, in *IAU Symposium*, Vol. 240, IAU Symposium, ed. W. I. Hartkopf, E. F. Guinan, & P. Harmanec, 417–425
- Raghavan, D. et al. 2010, *ApJS*, 190, 1
- Rebassa-Mansergas, A., Nebot Gómez-Morán, A., Schreiber, M. R., Girven, J., & Gänsicke, B. T. 2011, *MNRAS*, 413, 1121
- Reid, N., & Mould, J. 1984, *ApJ*, 284, 98
- . 1985, *ApJ*, 299, 236
- Reipurth, B., & Mikkola, S. 2012, *Nature*, 492, 221
- Renedo, I., Althaus, L. G., Miller Bertolami, M. M., Romero, A. D., Córscico, A. H., Rohrmann, R. D., & García-Berro, E. 2010, *ApJ*, 717, 183
- Richards, G. T., et al. 2002, *AJ*, 123, 2945
- Romanishin, W., & Angel, J. R. P. 1980, *ApJ*, 235, 992
- Romero, A. D., Campos, F., & Kepler, S. O. 2015, *MNRAS*, 450, 3708
- Rowell, N., & Hambly, N. C. 2011, *MNRAS*, 417, 93
- Rubin, K. H. R., Williams, K. A., Bolte, M., & Koester, D. 2008, *AJ*, 135, 2163
- Ruiter, A. J., Belczynski, K., Benacquista, M., Larson, S. L., & Williams, G. 2010, *ApJ*, 717, 1006
- Ruiter, A. J., Belczynski, K., Sim, S. A., Hillebrandt, W., Fryer, C. L., Fink, M., & Kromer, M. 2011, *MNRAS*, 1282
- Ruiz, M. T., & Takamiya, M. Y. 1995, *AJ*, 109, 2817
- Salaris, M., Serenelli, A., Weiss, A., & Miller Bertolami, M. 2009, *ApJ*, 692, 1013

Salim, S., & Gould, A. 2002, *ApJL*, 575, L83

Sanduleak, N., & Pesch, P. 1982, *IAU Circ.*, 3703, 1

Schneider, D. P. et al. 2010, *AJ*, 139, 2360

Schröder, K.-P., Pauli, E.-M., & Napiwotzki, R. 2004, *MNRAS*, 354, 727

Schwarzschild, M., & Härm, R. 1965, *ApJ*, 142, 855

Shu, F. H., Adams, F. C., & Lizano, S. 1987, *ARA&A*, 25, 23

Silvestri, N. M., Oswalt, T. D., Wood, M. A., Smith, J. A., Reid, I. N., & Sion, E. M. 2001, *AJ*, 121, 503

Silvestri, N. M., et al. 2006, *AJ*, 131, 1674

Sion, E. M., Oswalt, T. D., Liebert, J., & Hintzen, P. 1991, *AJ*, 101, 1476

Smedley, S. L., Tout, C. A., Ferrario, L., & Wickramasinghe, D. T. 2014, *MNRAS*, 437, 2217

Smith, M. C. et al. 2009, *MNRAS*, 399, 1223

Sokoloski, J. L., & Bildsten, L. 2010, *ApJ*, 723, 1188

Stoughton, C., et al. 2002, *AJ*, 123, 485

Stromberg, G. 1939, *ApJ*, 89, 10

Sweeney, M. A. 1976, *A&A*, 49, 375

Sweigart, A. V., & Gross, P. G. 1978, *ApJS*, 36, 405

Toonen, S., Nelemans, G., & Portegies Zwart, S. 2012, *A&A*, 546, A70

Torres, S., García-Berro, E., Krzesinski, J., & Kleinman, S. J. 2014, *A&A*, 563, A47

Tremblay, P.-E., & Bergeron, P. 2009, *ApJ*, 696, 1755

Tremblay, P.-E., Bergeron, P., & Gianninas, A. 2011a, *ApJ*, 730, 128

—. 2011b, *ApJ*, 730, 128

Tremblay, P.-E., Bergeron, P., Kalirai, J. S., & Gianninas, A. 2010, *ApJ*, 712, 1345

- Tremblay, P.-E., Ludwig, H.-G., Steffen, M., & Freytag, B. 2013, *A&A*, 559, A104
- Ungren, A. R. 1996, *QJRAS*, 37, 453
- van der Sluys, M. V., Verbunt, F., & Pols, O. R. 2006, *A&A*, 460, 209
- van Kerkwijk, M. H., Bergeron, P., & Kulkarni, S. R. 1996, *ApJL*, 467, L89
- van Leeuwen, J., Ferdman, R. D., Meyer, S., & Stairs, I. 2007, *MNRAS*, 374, 1437
- van Loon, J. T., Cioni, M.-R. L., Zijlstra, A. A., & Loup, C. 2005, *A&A*, 438, 273
- Vassiliadis, E., & Wood, P. R. 1993, *ApJ*, 413, 641
- Wachter, A., Schröder, K.-P., Winters, J. M., Arndt, T. U., & Sedlmayr, E. 2002, *A&A*, 384, 452
- Wegner, G. 1973, *MNRAS*, 165, 271
- Wegner, G., McMahan, R. K., & Boley, F. I. 1987, *AJ*, 94, 1271
- Weidemann, V. 1977, *A&A*, 59, 411
- . 1987, *A&A*, 188, 74
- . 2000, *A&A*, 363, 647
- Weidemann, V., & Koester, D. 1983, *A&A*, 121, 77
- Weinberg, M. D., Shapiro, S. L., & Wasserman, I. 1987, *ApJ*, 312, 367
- Weiss, A., & Ferguson, J. W. 2009, *A&A*, 508, 1343
- Williams, K. A., Bolte, M., & Koester, D. 2004, *ApJL*, 615, L49
- . 2009, *ApJ*, 693, 355
- Winget, D. E., Hansen, C. J., Liebert, J., van Horn, H. M., Fontaine, G., Nather, R. E., Kepler, S. O., & Lamb, D. Q. 1987, *ApJL*, 315, L77
- Wolf, W. M., Bildsten, L., Brooks, J., & Paxton, B. 2013, *ApJ*, 777, 136
- Wood, M. A. 1995, in *Lecture Notes in Physics*, Berlin Springer Verlag, Vol. 443, White Dwarfs, ed. D. Koester & K. Werner, 41

- Wood, M. A., & Oswalt, T. D. 1992, *ApJL*, 394, L53
- Woods, T. E., Ivanova, N., van der Sluys, M. V., & Chaichenets, S. 2012, *ApJ*, 744, 12
- York, D. G. et al. 2000, *AJ*, 120, 1579
- Yu, S., & Jeffery, C. S. 2010, *A&A*, 521, A85+
- Yuan, J. W. 1992, *A&A*, 261, 105
- Zacharias, N., Urban, S. E., Zacharias, M. I., Wycoff, G. L., Hall, D. M., Monet, D. G., & Rafferty, T. J. 2004, *AJ*, 127, 3043
- Zhao, J. K., Oswalt, T. D., Willson, L. A., Wang, Q., & Zhao, G. 2012, *ApJ*, 746, 144
- Zuckerman, B., Becklin, E. E., Macintosh, B. A., & Bida, T. 1997, *AJ*, 113, 764